Master Thesis

Effect of Micro-Porosity on CO_2-Brine Displacement Stability

Written by:
Éva Beatrix Radányi, BSc
1435632

Advisor:
Univ.-Prof. Dipl.-Phys. Dr.rer.nat. Holger OTT

Leoben, March 21, 2017

EIDESSTATTLICHE ERKLÄRUNG

Ich erkläre an Eides statt, dass ich die vorliegende Diplomarbeit selbständig und ohne fremde Hilfe verfasst, andere als die angegebenen Quellen und Hilfsmittel nicht benutzt und die den benutzten Quellen wörtlich und inhaltlich entnommenen Stellen als solche erkenntlich gemacht habe.

AFFIDAVIT

I hereby declare that the content of this work is my own composition and has not been submitted previously for any higher degree. All extracts have been distinguished using quoted references and all information sources have been acknowledged.

Kurzfassung

Wegen der hohen Treibhausgasemissionen der letzten Jahrzehnte gibt es ein wachsendes Interesse an der Entsorgung von Kohlendioxid (CO_2) in unterirdischen geologischen Formationen. Beispiele solcher Formationen sind tiefe salzhaltige Grundwasserleiter, die weltweit weit verbreitet sind. Da CO_2 über sehr lange Zeiträume gespeichert werden muss – im Wesentlichen über geologische Zeiträume – ist eine Vorhersage der CO_2-Migration im Reservoir unerlässlich. Ein besseres Verständnis der Verdrängungseffizienz von Formationswasser durch CO_2 im frühen und mittleren Injektionsstadium ist das Ziel dieser Studie. Nach Erreichen des chemischen Gleichgewichts kann der Verdrängungsprozess als nichtmischbare Zweiphasenströmung beschrieben werden. CO_2 ist unter typischen Reservoirbedingungen im überkritischen Zustand. Es besitzt eine geringere Dichte und eine geringere Viskosität als das Formationswasser. Dies führt unter Umständen zu Separation durch Auftrieb und zu viskosen Instabilitäten.

Petrophysikalische Gesteinseigenschaften spielen dabei eine entscheidende Rolle. Sie beeinflussen den CO_2-Fluss im Grundwasserleiter und somit auch die Stabilität der CO_2-Verdrängungsfront. Diese Eigenschaften werden durch die relative Permeabilität von CO_2, des Formationswassers und den entsprechenden Kapillardruckkurven beschrieben. In der vorliegenden Arbeit wird die stabilisierende Wirkung des Kapillardrucks auf unterschiedlichen Längenskalen und die Auswirkung relativer Permeabilität auf die Stabilität der CO_2-Front mittels numerischer Simulationen umfassend untersucht. Der Schwerpunkt dieser Arbeit liegt dabei auf der Einbeziehung von Mikroporosität in Karbonaten im Zusammenhang mit Gravitation und Instabilität. Dabei wird der Einfluss von Mikroporosität auf die Verdrängungseffizienz über Änderungen der relativen Permeabilität und über Kapillardruckkurven eingeführt und variiert.

Abstract

Because of the high green-house gas emission, in the last decade there was an increased interest on underground disposal of carbon-dioxide (CO_2) in underground geological formations. One example of those is deep saline aquifer, what has a wide availability around the world. As underground CO_2 storage is a long-term commitment, the determination of the injected CO_2 plume migration is essential. The displacement process of brine by CO_2 at the early injection stages (when saturation equilibrium is already achieved), what is the objective of this study, can be described as two-phase immiscible flow dominated by primary drainage. As brine and CO_2, even in supercritical state, has substantial density and viscosity contrast; instabilities, as viscous fingering and gravity override, are expected to occur. There are several petro-physical properties affecting the displacement front stability of CO_2 plume, including relative permeability relationships and capillary saturation function. The stabilizing effect of capillary pressure as a function of different length scales and the effect of the parameter alteration of the extended Corey relative permeability model on the CO_2 flood front stability had been studied extensively by means of numerical simulation. The scope of this research is to broaden the available results on the displacement stability of CO_2-brine systems by performing a sequence of numerical simulations with a focus on the possible mitigation effect of micro-porosity (typical for carbonates) on gravity segregation, by the occupation of micro-pores. To obtain an extensive picture on the effect of micro-pores on displacement stability, series of numerical experiments were performed in 2D, under representative conditions for CO_2 sequestration, with the systematic modification of length scales, capillary saturation functions representing typical rock types and the parameters of the extended Corey-model. With the simulation results it was exemplified that with sufficient length-scale the micro-porosity can be invaded by CO_2, and it has substantial effect on the stabilization of gravity fingering. Even though, with increasing the length-scale buoyancy gains more importance, so higher CO_2 saturation can be achieved in the top part of the reservoir, but the retention effects of micro-porosity on gravity fingering becomes less visible.

List of Tables

List of Figures

Abbreviations

A	area
BHP	bottom hole pressure
B_α	formation volume factor of phase α
B_o	Bond number
c_α	compressibility of phase α
cos(zz')	direction cosine between vertical Cartesian coordinate z' and the z coordinate normal to the initially plane macroscopic interface
c_p	pore compressibility
cp	centipoise
g	gravitational acceleration
S_α	saturation of the phase α
ϕ	porosity
ϕ_{eff}	effective porosity
L	characteristic length
IFT	interfacial tension
k	absolute permeability
kPa	kilopascal
kg/m^3	kilogram per cubic meter
$k_{r,\alpha}$	relative permeability of the phase α
$k_{r,nw}$	end point relative permeability of the non-wetting phase
l_{grain}	characteristic length of micro-porous grains
m	mass
M	mobility ratio
M_e	end-point mobility ratio
M_s	shock-front mobility ratio
m_α	mass of phase α
mD	miliDarcy
mN/m	miliNewton/m
m/s	meter/second
N_{cap}^{M}	macroscopic capillary number
n	Corey-exponent
p	pressure
ppm	parts per million
p_c	capillary pressure
p_{nw}	pressure of the non-wetting phase
PV	injected pore volume
p_w	pressure of the wetting phase
p_r	reservoir pressure
p_{sc}	standard condition pressure
r	radius

r_1	principle curvature radius 1
r_2	principle curvature radius 2
R_s	solution gas ratio
S_α	saturation of phase α
S_{con}	connate water saturation
S_{crit}	critical water saturation
S_{wirr}	irreducible water saturation
ρ	density
t	time
T	temperature
T_r	reservoir temperature
T_{sc}	standard condition temperature
U	flow velocity
v_l	linear flow velocity
v_α	actual velocity of phase α
v_{Darcy}	Darcy velocity
V_α	volume of phase α
V_b	bulk volume
V_p	pore volume
V_s	solid volume
θ	contact angle
σ_{12}	interfacial tension between fluid 1 and fluid 2
σ_{s1}	surface tension between solid and fluid 1
σ_{s2}	surface tension between solid and fluid 2
μ	dynamic viscosity
μ_α	dynamic viscosity of phase α
λ	wavelength

Subscripts:

brine	brine
CO_2	carbon-dioxide phase
crit	critcal
g	gas
int	interstitial
nw	non-wetting phase
o	oil
r	residual saturation of a phase
r	reservoir condition (with p, T, V, ρ)
ref	reference
sc	standard condition
w	wetting phase

Table of content

Page

1 Introduction

There are continuously newer and stronger evidences available (see e.g. the Report of the Intergovernmental Panel on Climate Change (IPCC)) that the global warming observed in the last decades are due to human activities. Global warming is responsible for the more common weather anomalies, the melting of the polar icecaps, and as consequence, for the increasing ocean levels. The almost universally accepted cause of global warming is the increasing greenhouse gas concentration of the atmosphere, particularly carbon-dioxide (CO_2). The development of greenhouse gas concentrations and global anthropogenic CO_2 emissions since the end of the industrial revolution are illustrated in Fig. 1.1.

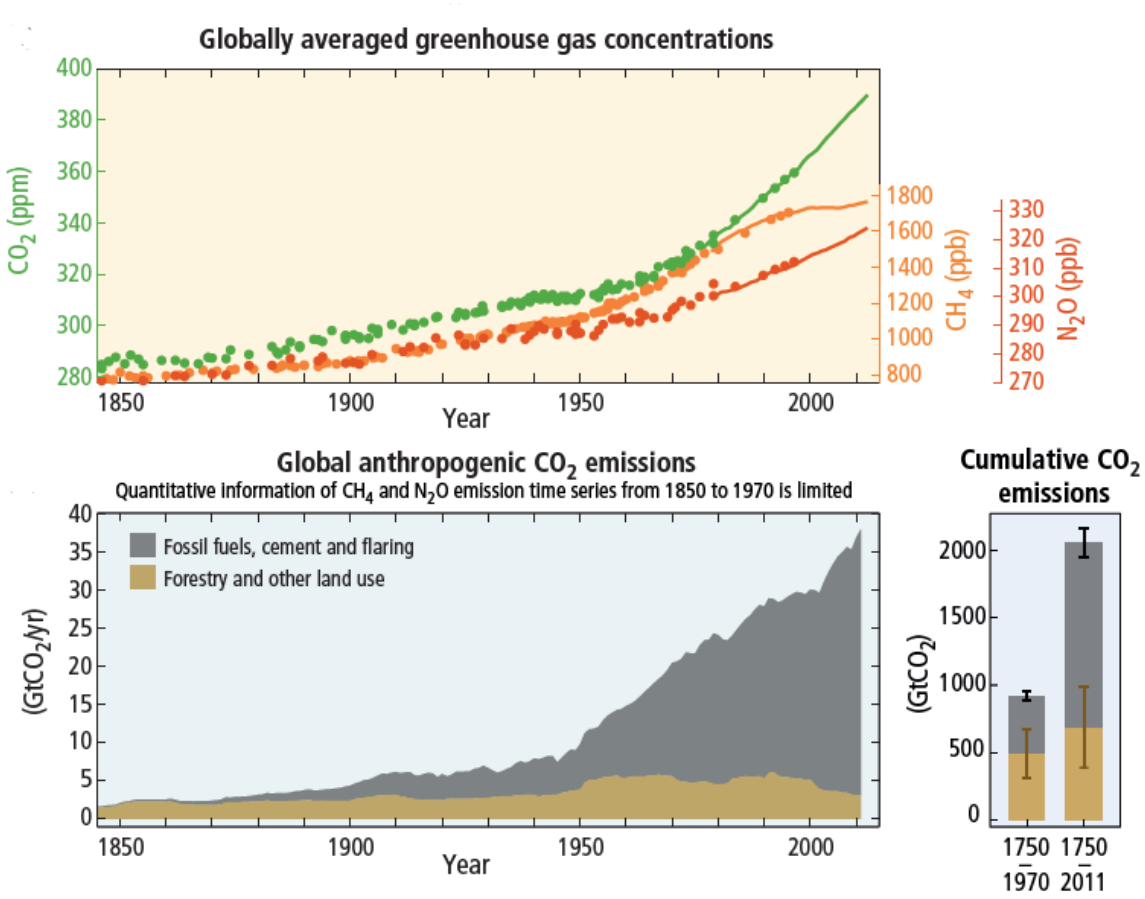

Figure 1.1 Globally averaged greenhouse gas concentrations and global anthropogenic CO_2 emissions (IPCC, 2014)

It is visible that the atmospheric CO_2 concentration rose from 280 ppm in pre-industrial times to 380 ppm nowadays. This trend is not sustainable and is expected to seriously affect world's climate.

One way to reduce the greenhouse effect of CO_2 is firstly, the deceleration of CO_2 emissions growth, then the reduction of it. Although many efforts took and take place to achieve that, a drastic change takes long, as large-scale transformation of the fossil fuel based energy system is required.

Other approach to mitigate the greenhouse effect of the CO_2 emission to the atmosphere is the underground disposal or utilization of it, by injecting it into suitable geological formations. There are four main CO_2 underground geological storage options as presented on Fig. 1.2; in depleted hydrocarbon reservoirs, in operating hydrocarbon reservoirs for enhancing oil recovery, in deep saline aquifers and for enhancing coal bed methane recovery.

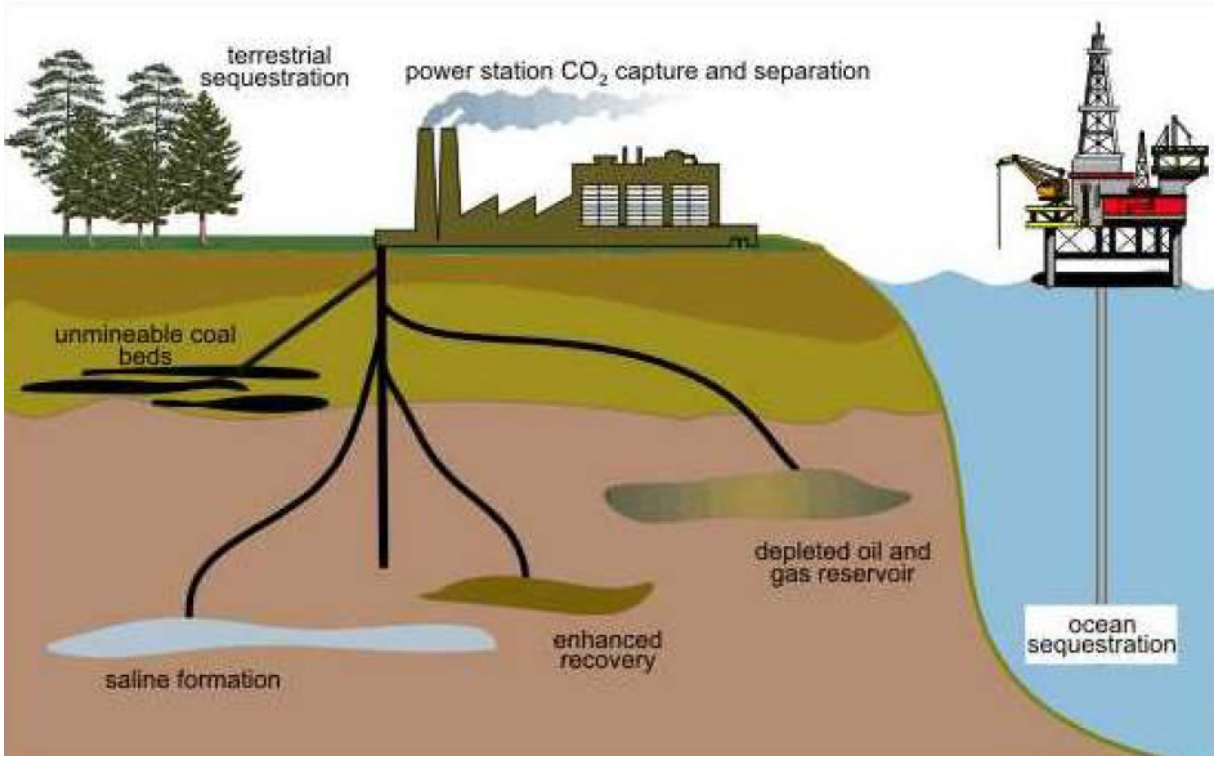

Figure 1.2 Methods for storing CO_2 in deep underground geological formations (Osman, 2007)

Vast amounts of underground storage capacity for CO_2 is available as underground saline aquifers, which is more abundant than any other underground storage option. The distribution of aquifers worldwide is shown on Fig. 1.3.

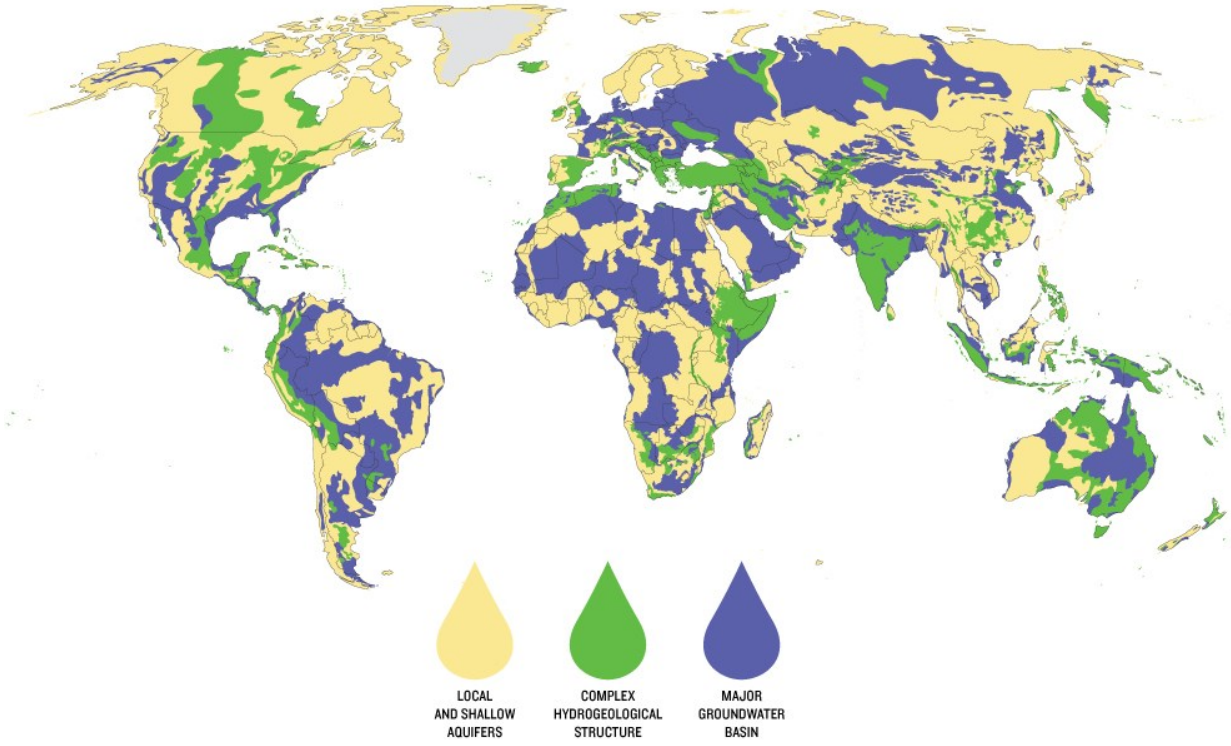

Figure 1.3 Aquifer distributions around the World (Barnett, 2015)

There are many key issues about CO_2 storage in aquifers related to storage security, such as the migration distance of the CO_2 plume in the aquifer, the amount of CO_2 dissolved in brine, the portion of CO_2 immobilized by means of capillary trapping and possible leakage scenarios. For assessing these uncertainties, the analysis of the multiphase flow system and the complex interplay of viscous, gravitational and capillary forces is required (Kuo et al., 2010).

In order to maximize storage efficiency, and to mitigate possible risks, the migration of the underground CO_2 plume is typically modelled by numerical simulations. Underground disposal of CO_2 is done under conditions, when CO_2 is in a supercritical state in order to achieve a desirable density. Even supercritical CO_2 is substantially less dense and viscous than brine, leading to displacement instabilities like gravity override and viscous fingering, preventing ideal displacement with high sweep efficiency. At the front, where CO_2 contacts the brine phase, both phases participate in each other. After equilibrium is reached, CO_2 sequestration in saline aquifers can be considered as a two-phase immiscible displacement. The two-phase CO_2-brine displacement is determined by, on top of other relevant properties, the relative permeability and capillary pressure functions. Those are specific for different rock-types and fluids present in the system. The focus of this thesis is on the effect of the parameters of the applied relative permeability model and capillary pressure functions on gravity fingering, being investigated by performing numerical simulations. In the numerical simulations two main capillary pressure functions were used, representing a typical unimodal (typical for sandstones) and bimodal (typical for carbonates) pore-size distribution. Generally, in rocks with bimodal pore structure, a high portion of the porosity belongs to the micro-

porosity, that cannot be invaded by the CO_2 phase by viscous forces. Meanwhile viscous forces cannot overcome capillary forces under conditions representative for field conditions, buoyancy forces of a high CO_2 column can be expected to occupied micro pores. As the micro-porosity does not contribute to the CO_2 flow, a mitigation of gravity fingering could be expected due to the occupation of micro-porosity by buoyancy. In this thesis, the behavior of gravity fingering was investigated with the presence of micro-porosity, by performing numerical simulations with different realizations of the relative permeability and capillary pressure functions.

2 CO_2 trapping mechanisms

CO_2 can be trapped in underground geological formation by either physical or chemical mechanisms. One major physical barrier is a tight cap rock on top of a formation that avoids the upward movement of CO_2. Other physical trapping mechanisms are provided by capillary forces. The CO_2 trapped by physical means can be either mobile (reduced mobility) or even immobile. Mobile CO_2 occurs, when the CO_2 saturation in pore space is greater than the irreducible saturation, forming a continuous phase and flowing as a result of viscous pressure gradients and buoyancy forces that can overcome viscous, interfacial and capillary forces, which oppose flow. In the case of immobile trapping, CO_2 is at residual saturation in pore space, so capillary forces are greater than viscous forces and buoyancy forces, so CO_2 is trapped without the existence of physical barrier (Bennion, 2010). In the case of geochemical trapping, the injected CO_2 reacts with the host rock. In one form, such chemical reaction takes phase that the injected CO_2 is converted to solid carbonate minerals.

Those trapping mechanisms are characteristic for different time periods during and after the injection of CO_2 to deep saline aquifers. In the injection stage, as CO_2 and brine has low mutual solubility, and it leads to a multiphase flow system driven by large pressure gradients, strong viscous and buoyant forces. With the abortion of the injection, the second characteristic time period starts. Viscous and buoyant force induced advective flow slowly eliminates, and compositional effects gain more importance; for example the dissolution of CO_2 into the brine phase, the increase of brine density, and the downward fingering of CO_2-rich brine. This stage is generally lasts decades or even centuries. Finally, the multi-phase flow process terminates, as the CO_2 plume becomes immobile and CO_2 is dissolved to the brine. Then, the geochemical effects gain importance, affecting such rock properties like porosity or permeability (Darcis et al., 2011). These stages are well represented as the function of time in Fig. 2.1.

This thesis is intended to discuss CO_2 sequestration only in the aspects of immiscible multi-phase flow behavior, so the early periods of CO_2 injection into saline aquifers.

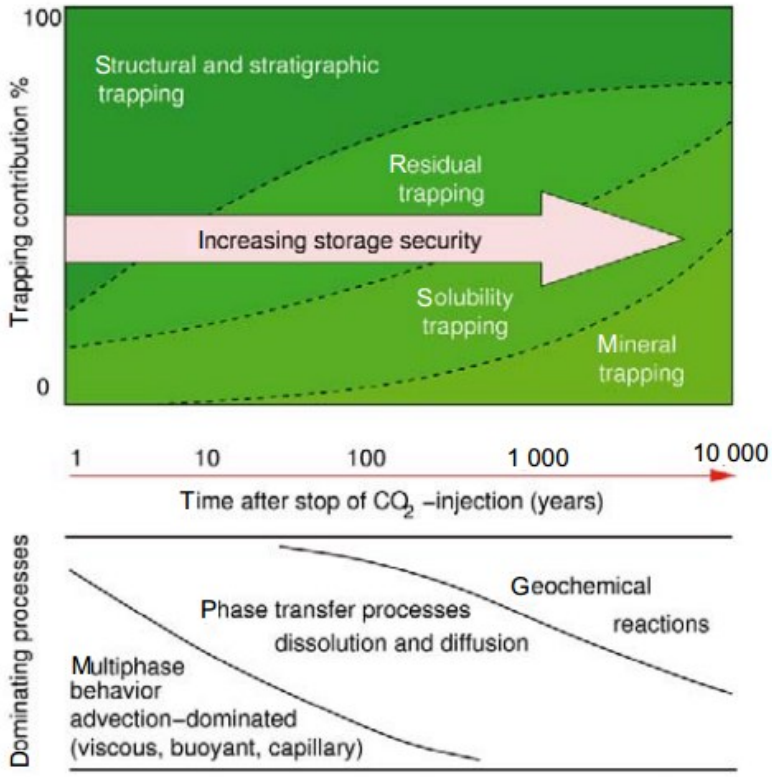

Figure 2.1Trapping mechanisms and governing processes during and after the injection of CO_2 into saline aquifers (IPCC Special Report, 2005)

3 Fundamental properties of porous media

A porous medium is a solid containing void spaces (pores) either connected or unconnected, dispersed within it in either regular or random manner. In this chapter some critical properties of porous media are described, which are utilized to describe the CO_2-brine multi-phase flow behavior.

3.1 Porosity

One major property of a porous medium is the total porosity, what is the ratio of the void spaces to the total bulk volume of the media. Porosity can be defined the following way:

$$V_b = V_p + V_s \tag{3.1}$$

$$\phi = \frac{V_p}{V_b} = \frac{V_b - V_s}{V_b} \tag{3.2}$$

Depending on the accessibility of the pore, two kinds of porosities can be distinguished; total and effective porosity. In the case of total porosity, all void spaces, even isolated ones are considered. Meanwhile only pore spaces that contribute to the fluid transport are included into effective porosity. For the underground CO_2 disposal, the latter one is relevant, as the effective porosity contributes only to the storage capacity of a reservoir.

Porous media, to a limited extent, is considered to be a slightly compressible, so pressure changes affect porosity. The isothermal compressibility of porosity is expressed as:

$$c_\phi = -\frac{1}{\phi}\left(\frac{\partial \phi}{\partial p}\right)_T \tag{3.3}$$

3.2 Capillary properties

3.2.1 Saturation

The void spaces in a porous medium might contain several fluid phases. The saturation of each phase is defined as:

$$S_\alpha = \frac{V_\alpha}{\phi_{eff}} \tag{3.4}$$

The sum of the saturations results in:

$$\sum_\alpha S_\alpha = 1 \tag{3.5}$$

3.2.2 Wettability

Wettability is the ability of one fluid to spread on a solid surface (in this case rock surface) in the presence of another and it is such property of the reservoir rock-fluid system that has a major impact on fluid saturation distributions and on multi-phase flow processes. Wettability is described by the contact angle (θ), and it is illustrated in Fig. 3.1.

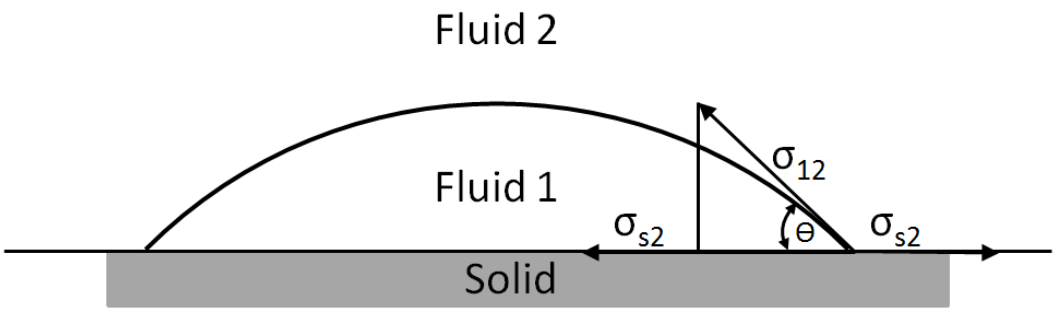

Figure 3.1 Wettability and contact angle

For this particular case (CO_2-brine system), brine (Fluid 1 in Fig. 3.1) is the wetting phase, so the value of the contact angle is less than $90°$. The contact angle can be also defined by the interfacial tensions between the fluid phases, and the fluid-solid interfaces, the following way:

$$cos\theta = \frac{\sigma_{s2} - \sigma_{s1}}{\sigma_{12}} \tag{3.6}$$

Contact angle has a substantial effect on the capillary pressure. In the case of CO_2-brine system the CO_2 is considered to be the non-wetting phase (in Fig. 3.1, Fluid 2). CO_2-brine interfacial tension is a function of pressure, temperature and brine salinity.

3.2.3 Capillary pressure

Because of the different wettability properties of immiscible fluid phases for a given rock type, the fluid-fluid interfaces are curved in the pore space. As a consequence, there is a pressure discontinuity present between the wetting and non-wetting phase, $p_{nw} > p_w$. This pressure difference is called capillary pressure, and can be expressed by the following equation:

$$p_c = \sigma_{12}\left(\frac{1}{r_1} + \frac{1}{r_2}\right) = p_{nw} - p_w = \frac{2\sigma_{12}cos\theta}{r} = (\rho_w - \rho_{nw})gh \tag{3.7}$$

Fig. 3.2 illustrates of the principal radii of the curvature from Eq. 3.7.

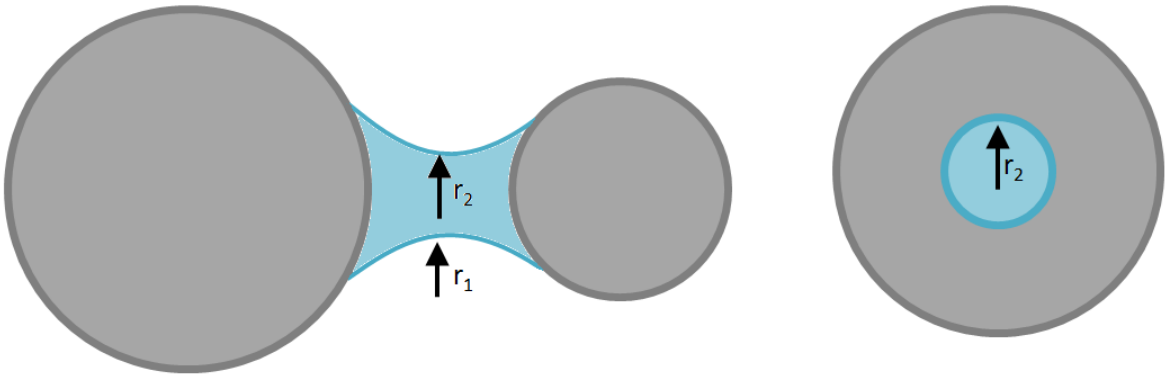

Figure 3.2 Illustration of the principal radii of the curvature

If the fluids present in the pore space equally wet rock surface, so the fluid-fluid interface is perpendicular to the solid surface, the capillary pressure is zero. The actual capillary pressure is the function of water saturation (Ott, 2015).

Fig. 3.3 shows typical drainage and imbibition capillary pressure functions. Starting from Point A, with the injection of CO_2 to the aquifer, the brine is displaced by the CO_2. In order to inject CO_2 into the pore space, one must overcome the capillary entry pressure. If the difference in phase pressure (imposed pressure differential) is plotted as a function of the decreasing water saturation the result is the dashed line on the figure. Reaching the connate water saturation (Point B), water saturation cannot be reduced further. With reversing the saturation change, imbibition takes place. Capillary hysteresis occurs due to the difference in advancing and receding contact angle (Dake, 1978).

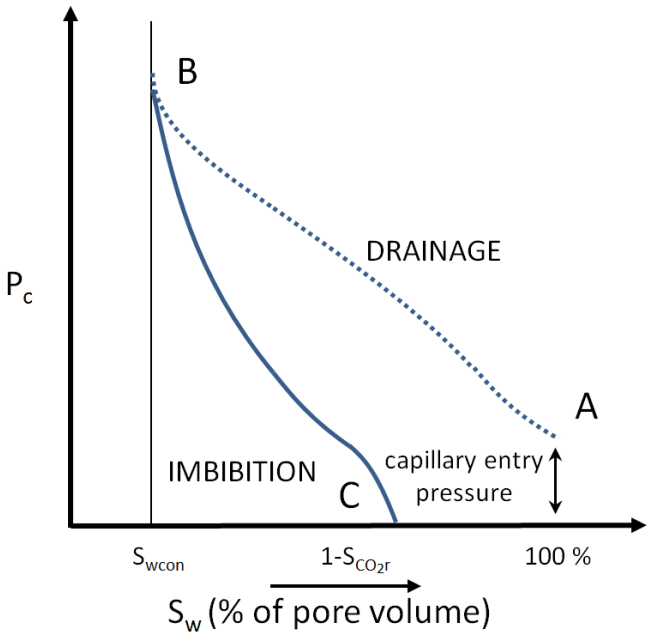

Figure 3.3 Drainage and imbibition capillary pressure function (based on Dake, 1978)

For a measurement of capillary pressure saturation functions, different methods can be used such as mercury injection capillary pressure (drainage only), the centrifuge methods (forced invasion) or AMOTT (spontaneous invasion).

3.3 Permeability

The absolute permeability is such a rock property that is assumed to be constant, irrespective of the nature of the fluid flowing through the pores. This statement is valid (with the exception of gas flow either at low pressures or very high rates); in case the rock is completely saturated with the fluid in question, and is defined as k in Darcy´s equation (Dake 1978).

$$q = A\frac{k \cdot \Delta p}{\mu \cdot L} \tag{3.8}$$

3.4 Relative permeability

When multiple fluid phases flow simultaneously in the porous media, the flowing abilities of each phase decreases with the increasing saturation of the other(s). Each of the fluids present has a so called effective permeability. Due to the diffuse nature of the multi-phase flow is porous media, the sum of these effective permeabilities will be less than the absolute permeability for given medium. The effective permeability values can be normalized and simplified for calculations, by dividing the effective permeability by the absolute permeability. The resulting measure is called the relative permeability of a fluid phase with the presence at least one more:

$$k_{r,\alpha}(S_w) = \frac{k_{eff,\alpha}(S_w)}{k} \tag{3.9}$$

The following figure shows a typical effective permeability and relative permeability curve for a CO_2-brine system. Both curves have the same shape, only difference is that the relative permeability scale has a range from zero to unity (Dake, 1978).

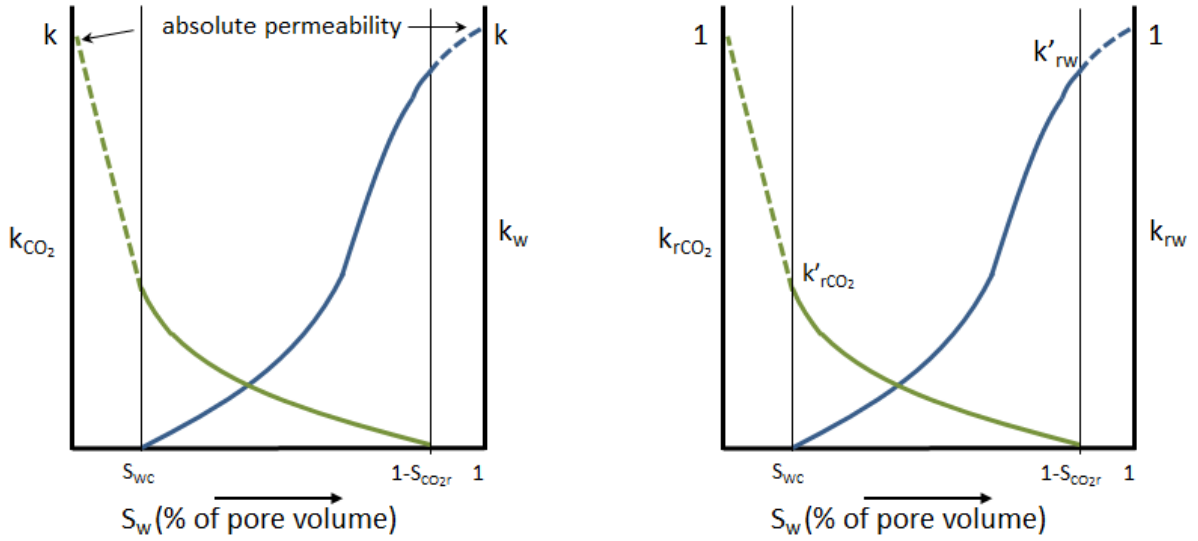

Figure 3.4 Effective permeability (left) and corresponding (right) relative permeability, as functions of the water saturation for water-oil system (based on Dake, 1978)

For a more precise description, three more terms have to be introduced; the irreducible, the critical and the connate saturation. The irreducible water saturation (S_{wir}) is the lowest water saturation that can be achieved in a core plug by displacement process. It can vary with the nature of displacement (Petrowiki), the final drive pressure or the maximum speed of rotation in a centrifuge (Oilfield Glossary). The connate water saturation $(S_{wcon})$is the in situ water saturation that is trapped in the pores during the formation of the rock (Oilfield Glossary). The S_{wcon} and S_{wir} might differ depending on if the creation of connate water can repeated by displacement processes. The critical water saturation (S_{wcrit}) is the water saturation, below which the water becomes immobile during a specific displacement process. These terms are illustrated in Fig. 3.5;

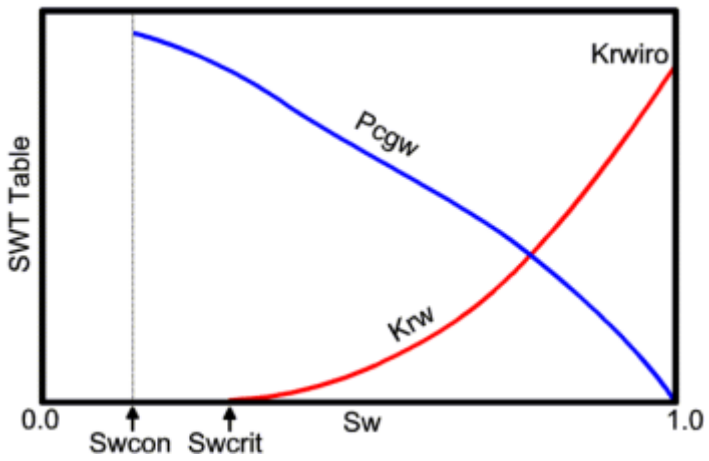

Figure 3.5 Relative permeability and capillary pressure curves (screenshot from CMG IMEX)

The S_{wcrit}, was introduced so that the capillary pressure function could be entered along the whole water saturation interval; $0 \leq S_w \leq 1$, (Fig. 3.6). As it is discussed in the coming

Chapter 5, CO_2-brine displacement relative permeability measurements in carbonate rock types generally have high remaining (or if they equal, connate or irreducible) water saturations. If in CMG IMEX (the simulation tool applied in this thesis) the remaining water saturation from relative permeability measurements is defined as connate water, there is no possibility to achieve water saturation below this water saturation, so observing the effect of the micro-porosity on displacement is not expected to be possible. The relationship between of critical water saturation with relative permeability and capillary pressure function is illustrated in Fig. 3.6.

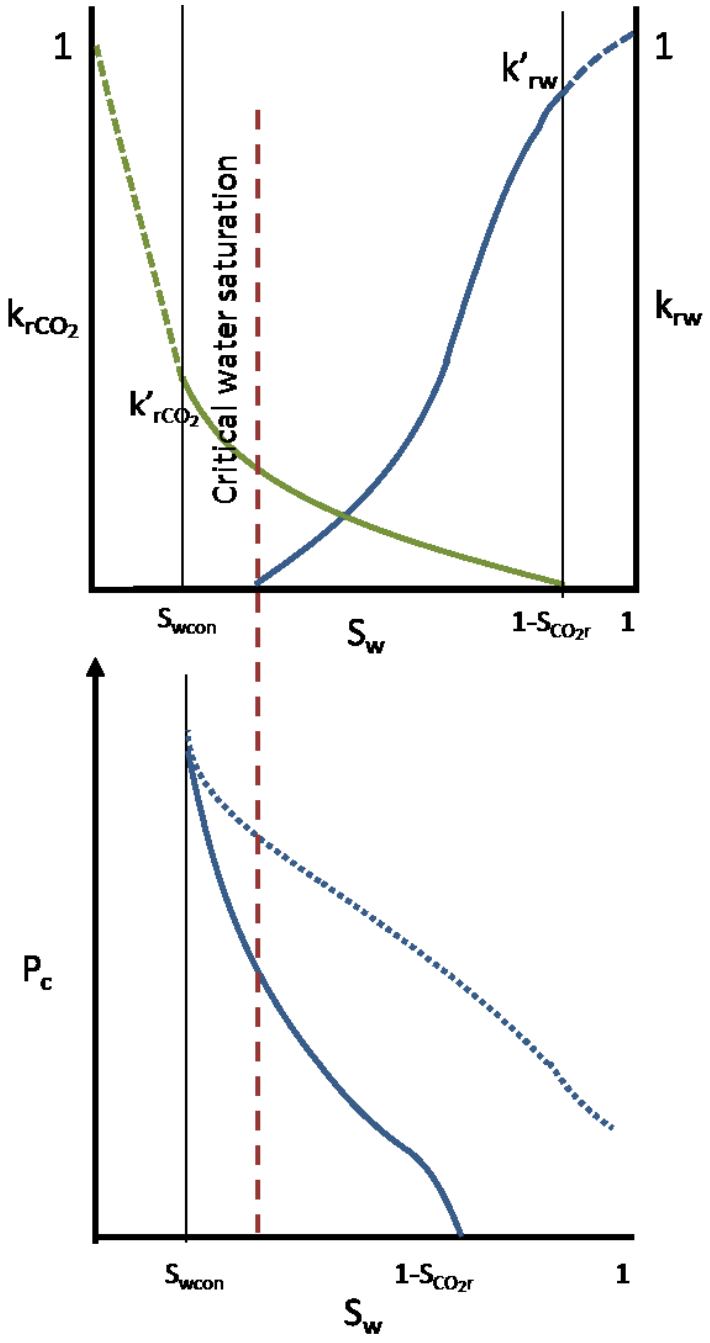

Figure 3.6 The critical water saturation

3.5 Fluid properties

3.5.1 Density

Density can be defined as the mass over the unit volume of a given material/fluid, as can be seen in the following:

$$\rho_\alpha(p,T) = \frac{m_\alpha}{V_\alpha} \tag{3.10}$$

Density is a pressure and temperature dependent property. Standard or surface conditions in petroleum engineering practice is; $1\ atm\ =\ 1.013\ bar$ and $15\ °C\ =\ 273.15\ K$.

3.5.2 Formation volume factor

As surface and reservoir conditions differ, the volume of the fluid downhole is different than the fluid volume at the surface. The measure of the change is the formation volume factor and defined by the ratio of the fluid volume at reservoir and the volume at surface condition:

$$B_\alpha = \frac{V_\alpha(p_r,T_r)}{V_\alpha(p_{sc},T_{sc})} = \frac{\frac{m_\alpha}{\rho_\alpha(p_r,T_r)}}{\frac{m_\alpha}{\rho_\alpha(p_{sc},T_{sc})}} = \frac{\rho_\alpha(p_{sc},T_{sc})}{\rho_\alpha(p_r,T_r)} \tag{3.11}$$

When conservation of mass applies, the formation volume factor can be also expressed as the ratio of the phase densities at standard and reservoir conditions.

3.5.3 Fluid viscosity

Absolute or dynamic viscosity is the measure of a fluid's internal resistance to flow, caused by the relative fluid particle movements. The measure of viscosity is the tangential force resisting to flow per unit area required to move one horizontal; plane with respect to another plane – at an unit velocity – when maintaining a unit distance apart in the fluid (Engineering Toolbox).

3.6 Multiphase-flow description

Brine and CO_2 are immiscible at target reservoir conditions ($1000\ m$ to $3000\ m$), so the CO_2 plume migration will be governed by multiphase flow physics (Kuo et al., 2010). In numerical simulation of multi-phase flow there are two major equations used, for simplicity incompressible flow is assumed without mass transfer between the fluid phases present [Lake, 1989]:

- Mass balance equation:

$$\Phi\frac{\delta S_\alpha}{\delta t} + \nabla\overrightarrow{v_i} = 0 \tag{3.12}$$

- Extended Darcy´s law for multiphase flow:

$$\overrightarrow{v_\alpha} = -\frac{k_{r,\alpha} \cdot k}{\mu_\alpha}(\nabla P_\alpha - \rho_\alpha \cdot \vec{g}) \tag{3.13}$$

Where the equation $S_w + S_{nw} = 1$ is satisfied.

4 Phase behavior of brine and super critical CO_2

In case of CO_2-brine system, the displacing CO_2 is the less viscous and dense fluid compared to brine, so CO_2 injection in saline aquifer have the tendency of forming instabilities like viscous fingering and gravity override. The pressure and temperature dependency of CO_2 and brine at zero salinity is illustrated in Fig. 4.1.

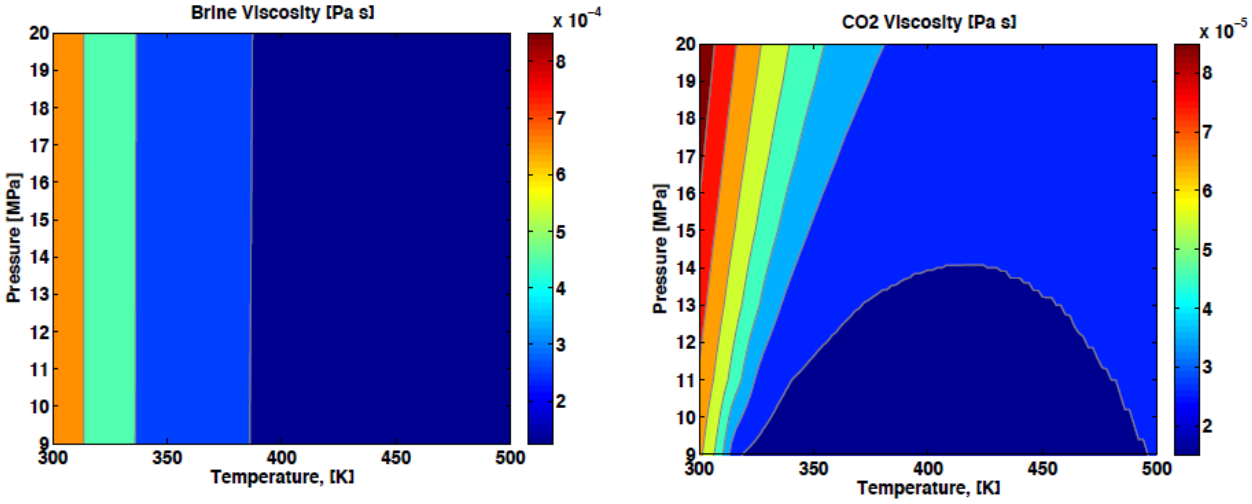

Figure 4.1 Viscosity of CO_2 and brine as functions of pressure and temperature at zero salinity (Benson et al., 2013)

In order to eliminate that effect, underground CO_2 disposal is performed at supercritical conditions for CO_2. The critical point of CO_2 is $P_{crit} = 73.82\,bar$ and $T_{crit} = 31.04\,°C = 304.55\,°K$ (Julio et al., 2013). The phase diagram of CO_2 is shown in Fig. 4.2.

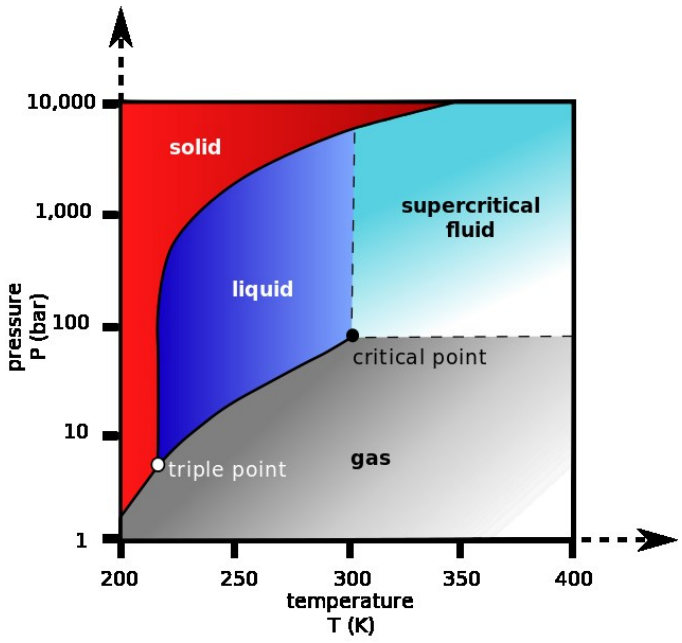

Figure 4.2 Phase diagram of CO_2 (Wikipedia)

At supercritical conditions CO_2 has the viscosity of gas, still an order lower than a liquid, but has a density closer to it. The pressure and temperature dependency of brine and CO_2 is illustrated in Fig. 4.3.

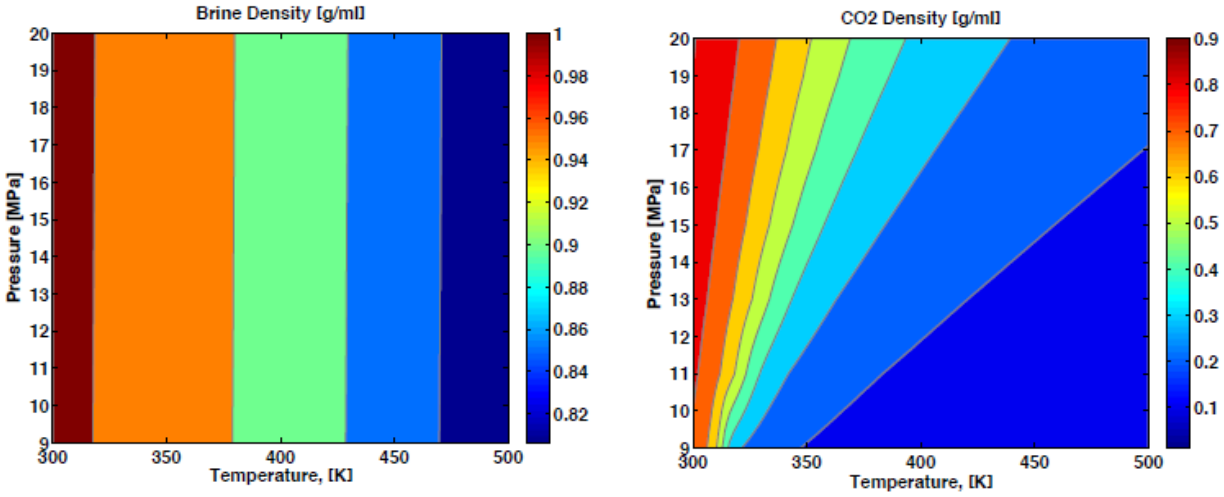

Figure 4.3 Pressure and temperature dependency of CO_2 and brine at zero salinity (Benson et al., 2013)

As an advantage lower injection pressure is required and effective utilization of pore space is achieved. On the other hand supercritical CO_2 still has lower density than water, so gravity segregation is expected due to buoyancy forces.

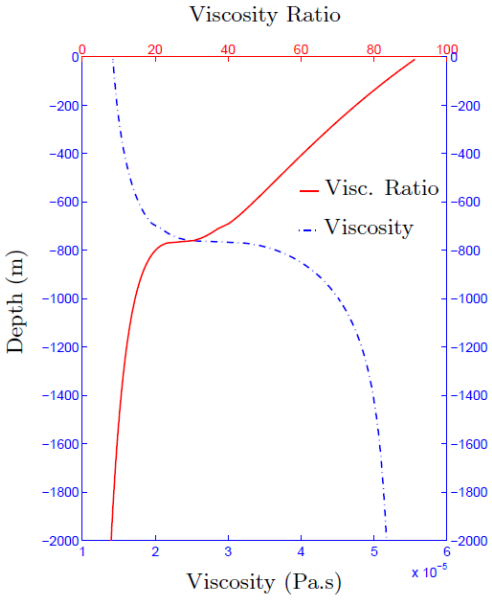

Figure 4.4 CO_2 viscosity and μ_{H_2O}/μ_{CO_2} (Julio et al., 2003)

Fig. 4.4 illustrates depth variation of viscosity of CO_2 and the CO_2 brine viscosity ratio assuming a $3\,°C/100\,m$ geothermal gradient. As it can be interpreted from the figure, the ideal aquifer for CO_2 storage is at least in $800\,m$ depth, where the pressure equals the critical pressure for CO_2, and viscosity ratio between water and CO_2 reaches nearly its minimum.

Fig. 4.5 shows the CO_2 phase diagram and the equivalent state of CO_2 with depth variation. Next to it, the density variation of CO_2 is illustrated with increasing depth. As the critical point of CO_2 is reached, the change of the volume related to surface conditions $(1\ atm, 15\ °C)$ start to decrease in less increments with depth.

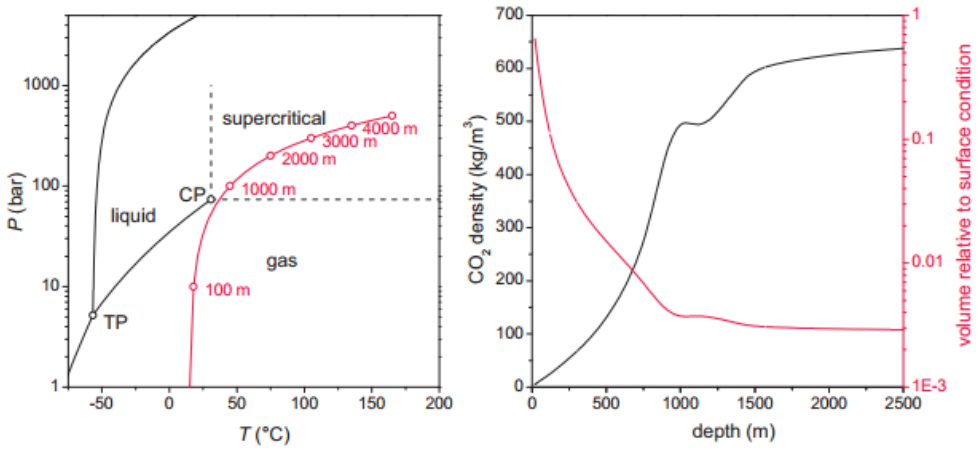

Figure 4.5 CO_2 phase diagram and relative volume variation with depth (Ott, 2015b)

Two important properties of the injected CO_2, influencing carbon sequestration operation are the density and the viscosity of the supercritical CO_2. The determination of those properties is relevant to the estimation of the extent of gravity override and the stability of the displacement front.

As in the case of supercritical CO_2, brine viscosity and density can also be estimated by correlations and measurements. As brine is only compressible to a very limited extent compared to gases, the most critical parameters for brine density and viscosity calculation are not the pressure, but temperature and brine salinity. Generally speaking, the higher the brine temperature, the lower is the viscosity and the density of it. With greater aquifer depth, the brine temperature is also higher, and the lower brine density is compensated by the elevated pressure conditions. The effects of brine salinity on viscosity and density depend on the type of salts present, and their total concentration. With increasing salt concentration, both brine density and viscosity are higher. The brine density is critical for estimating the gravity override of CO_2; meanwhile the brine viscosity affects viscous stability of the CO_2 front.

The effect of brine salinity on CO_2-brine viscosity ratios are illustrated in Fig. 4.6, as a function of pressure and temperature. With increasing brine salinity, the viscosity of it is increasing under the same temperature and pressure condition; hence CO_2-brine viscosity ratio is decreasing, leading to viscous instabilities of a higher extent.

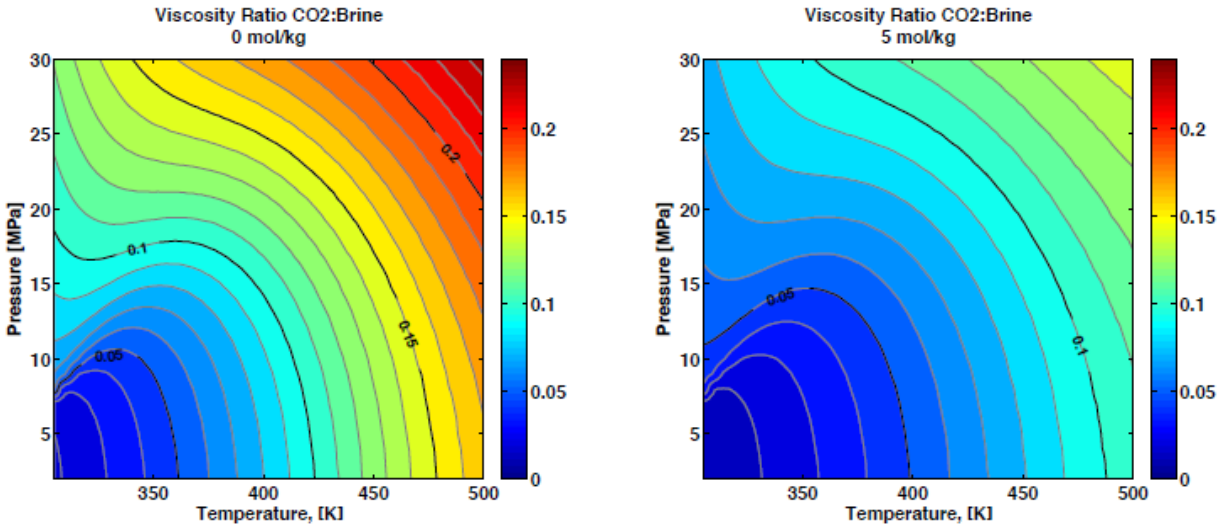

Figure 4.6 Viscosity ratios of CO_2 with respect to brine as functions of pressure and temperature at salinities of $0\ mol/kg$ and $5\ mol/kg$ (Benson et al., 2013)

Fig. 4.7 illustrates how brine salinity affects the CO_2-brine density ratio as a function of pressure and temperature.

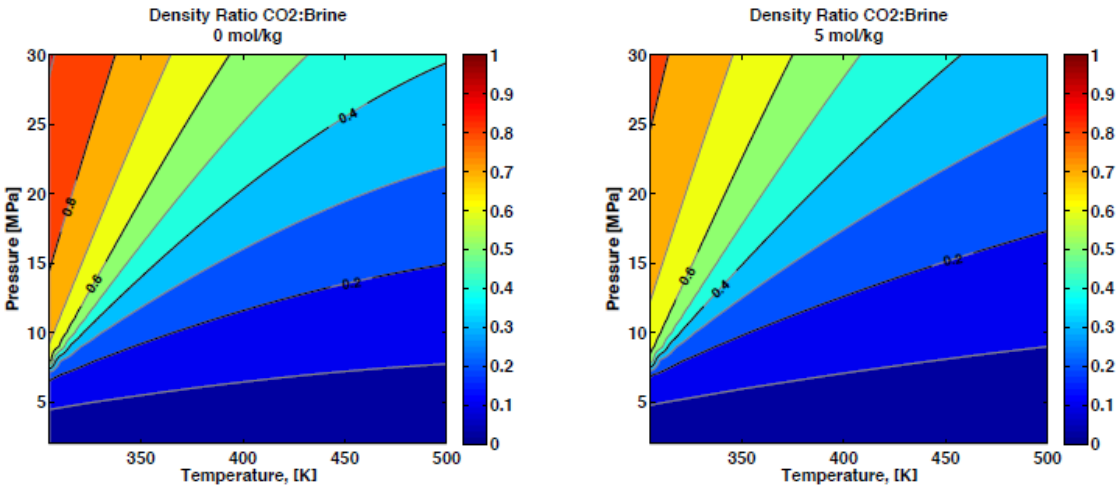

Figure 4.7 Density ratios of CO_2 with respect to brine as functions of pressure and temperature at salinities of $0\ mol/kg$ and $5\ mol/kg$ (Benson et al., 2013)

With higher brine salinity, higher pressure and lower temperature conditions would be required in order to achieve the same CO_2-brine density ratio, so increasing brine salinity enhances gravitational instabilities

4.1 Supercritical CO_2 density calculation

In the paper of Liang-Biao Ouyang (2011), correlations for predicting the density and viscosity of pure CO_2 under supercritical conditions expected in carbon capture and sequestration have been developed. The methodology applied was the generation of CO_2

properties under the target pressure and temperature ranges, based on the high accuracy CO_2 data provided by the National Institute of Standards and Technology (NIST). The data was then applied to create the two explicit correlations via a least square approach. The correlation formulae and the associated correlation coefficients were adjusted to meet the following criteria:

$$\sum\left(\rho_{pre}-\rho_{NIST}\right)^2=\sum[\rho_{pre}\,(p,T)-\rho_{NIST}]^2=minimum \tag{4.1}$$

$$\sum\left(\mu_{pre}-\mu_{NIST}\right)^2=\sum[\mu_{pre}\,(p,T)-\mu_{NIST}]^2=minimum \tag{4.2}$$

Where ρ is in kg/m^3 and μ is in cp. The subscript pre refers to data calculated by the proposed correlations, whereas subscript $NIST$ refers to data generated from the NIST table. Those correlations are applicable for CO_2 density and viscosity calculations for $7000-62000\ kPa$ pressure and $40-100$ °C temperature interval.

The density correlation is given below as the function of pressure:

$$\rho=A_0+A_1p+A_2p^2+A_3p^3+A_4p^4 \tag{4.3}$$

Where CO_2 density (ρ) is in kg/m^3, pressure (p) in $psia$, and the correlation coefficients A_0, A_1, A_2, A_3 and A_4 can be associated with temperature in Celsius in the following way:

$$A_i=b_{i0}+b_{i1}T+b_{i2}T^2+b_{i3}T^3+b_{i4}T^4 \qquad (i=0,1,2,3,4) \tag{4.4}$$

The values of the correlation coefficients (b_{i0}, b_{i1}. b_{i2}, b_{i3} and b_{i4}) are listed in Appendix A, for pressure higher than $20\,680\ kPa$ and lower.

4.2 Supercritical CO_2 viscosity calculation

Similarly to the supercritical CO_2 density calculation, a correlation for viscosity calculation was introduced by Ling-Biao Ouyang (2011), which consists of the following formulas:

$$\mu=C_0+C_1p+C_2p^2+C_3p^3+C_4p^4 \tag{4.5}$$

Where the CO_2 viscosity (μ) is in cp, pressure (p) in $psia$, and the correlation coefficients C_0, C_1, C_2, C_3 and C_4 can be calculated the following way:

$$C_i=d_{i0}+d_{i1}T+d_{i2}T^2+d_{i3}T^3+d_{i4}T^4 \qquad (i=0,1,2,3,4) \tag{4.6}$$

The temperature is in Celsius in the equation.

With these correlations CO_2 densities were calculated for reference temperature of $45\ °C$ and a pressure range of $7000\ kPa$ – $13\,000\ kPa$ for representative purpose. Using Eq. 3.11, gas

formation volume factors were determined with a standard CO_2 density of $1.8415\ kg/m^3$ .The following table summarizes the results of the calculation for the pressure interval:

Table 4.1 CO_2 density and formation volume factor at $45\ °C$ as a function of pressure with a standard CO_2 density of $1.8415\ kg/m^3$

P [kPa]	ρ_{CO2} [kg/m^3]	B_{CO2} [-]	μ_{CO2} [cp]
7000	105.2259	0.017500	0.01782
8000	252.6559	0.007289	0.02153
9000	379.1962	0.004856	0.02882
10000	485.2846	0.003795	0.03617
11000	571.7688	0.003221	0.04315
12000	639.9064	0.002878	0.04962
13000	691.3645	0.002664	0.05490
14000	728.2202	0.002529	0.05936

5 Relative permeability and capillary pressure function in the aspect of underground CO_2 storage

The displacement efficiency of brine by CO_2 is determined by relative permeability $(k_r(S_w))$ and capillary pressure $(p_c(S_w))$ saturation functions (Ott et. al, 2014)). These functions are important for the estimation of CO_2 plume migration and reservoir confinement, because of the long-term nature of the underground CO_2 storage. Both macroscopic and microscopic displacement efficiency are determined by relative permeability and capillary pressure functions. As brine and CO_2 relative permeability relationship and capillary pressure functions are the governing properties of immiscible displacement, several experiments have been performed to determine those.

On pore scale level the phase distribution and their mobilities are controlled by (Egermann et al., 2016):

- The interfacial tension between CO_2 and brine: determines the accessibility for each phase for certain fraction of the pore space
- The wettability of rock-fluid system: in CO_2-brine system, CO_2 is considered to be the non-wetting phase, even though some recent studies claim that under some mineralogical conditions CO_2 wettability could be mixed-wet

5.1 Relative permeability derivation

Knowledge of the relative permeability curve endpoints and shape characteristics are detrimental for the approximation of the CO_2 plume migration in deep saline aquifers, as they have a great influence on CO_2 saturation distribution. It affects many important factors of a CO_2 sequestration project: the spatial extent of the CO_2 plume, the injectivity of the well, and the extent of capillary trapping. Relative permeability is an empirical parameter that depends on the specific context that is being applied for (Benson et al., 2013). In the case of CO_2 injection to deep saline aquifers, the pores are saturated with the wetting phase (brine), what is displaced by the non-wetting CO_2 phase. This is called the drainage process, and relative permeabilities for CO_2 injection modeling should be determined under these conditions. As CO_2 injection stops, the wetting brine phase imbibes back to the CO_2 flooded pores, so relative permeability under such conditions are also relevant. The measured relative permeability also can depend on the rock heterogeneity; scale, and questionably, on the method being used for the measurement.

The derivation of relative permeability curves is generally done by core-flood experiments. For the relative permeability function determination, different types of core-flooding experiments are performed, in case of CO_2-brine displacement in deep saline aquifers, the main focus is on drainage measurements. After performing the core-flood experiments the fluid saturation profiles, fluid production curves and differential fluid pressures are further investigated by numerical simulation. After performing the history matching, the relative

permeability functions can be derived, and used in reservoir simulations to predict CO_2 plume migration. A procedure for the history matching of core-flood experiment is shown in Fig. 5.1:

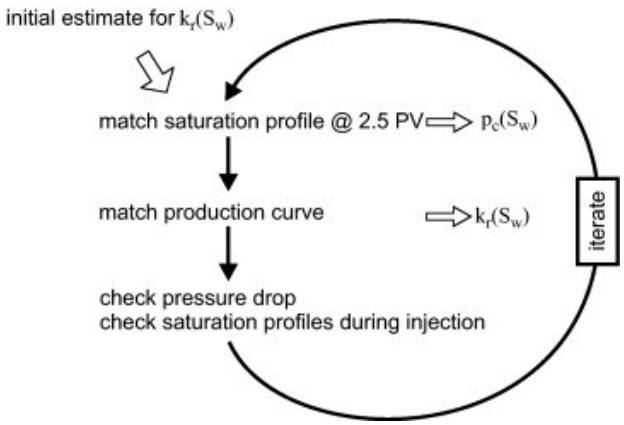

Figure 5.1 Strategy for history matching of unsteady-state experiment (Berg et. al., 2013)

5.1.1 Experimental setup

Those core flood experiments are generally performed at reservoir conditions, e.g. $50\ ℃$ and $100\ bar$ that equals to around $1000\ m$ depth (Ott et al., 2015). A typical sample size is $7.5\ cm$ by $15\ cm$. Berg et al. (2013) and Ott et al. (2015) performed two types of experiment for the relative permeability data determination; the CO_2-brine primary drainage experiment, and then decane was used as displacing phase. The same core sample was used for both experiments; the decane-brine displacement was performed to serve as base, water-wet, case. For the experiments, unsteady-state method was used. One example for experimental setup and procedure are described in the previously mentioned publications.

There are two main types of core-flood experiments; unsteady-state and steady-state methods (illustrated in Fig. 5.2).

5.1.2 Unsteady-state method

While an unsteady-state experiment is being performed, the used core sample is saturated with the wetting-phase (brine), and then brine is displaced by the non-wetting phase (CO_2). The pressure decay over the core and water saturation is time dependent and results are recorded (Berg et al., 2011). The time required to complete an experiment is significantly less than for steady-state experiments. The relative permeability and capillary pressure during unsteady-state experiments must be determined separately. Unsteady-state methods can be further divided to four categories: high-rate methods, low-rate methods, centrifuge methods and stationary liquid methods (Christiansen et al., 1995).

5.1.3 Steady-state method

The core sample is initially fully saturated with brine solution, both fluid phases are injected simultaneously at different proportions. The fractional flow of non-wetting phase is increased stepwise; meanwhile total flow rate is kept constant. For changing the fractional flow, as

pressure drops and saturations have stabilized, so steady-state condition is reached (Berg et al., 2013). Thus steady-state methods require a sequence of experiments performed over a range of discrete, steady flow conditions. Each sequence step may take up to a week to complete, depending on rock properties. The group of steady-state methods can be divided to four sub-groups, based on the experimental approach to minimize capillary-end effect; the multiple-core methods, the high-rate methods, the stationary liquid methods and the uniform capillary pressure method (Christiansen et al, 1995).

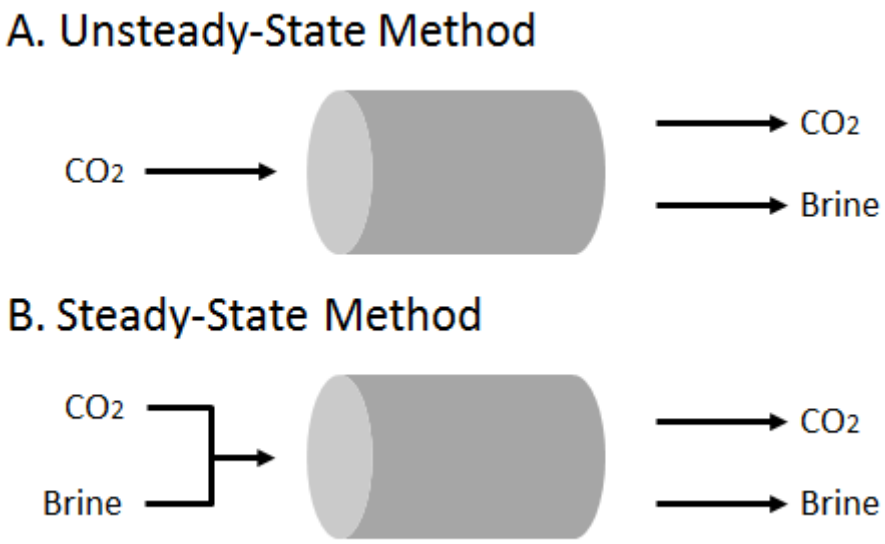

Figure 5.2 Illustration of unsteady-state and steady state methods of measuring two-phase CO_2 and brine relative permeability (based on Lucia, 1999)

5.1.4 Other relevant relative permeability considerations for CO_2-brine displacement

The displacement type: the CO_2 saturation history is relevant, due to the saturation dependent hysteresis mechanism between drainage and imbibition. As CO_2 is considered to be the non-wetting phase, drainage dominates for the primary invasion.

Bennion and Bachu (2008) presented a detailed experimental protocol for the relative permeability measurements performed at reservoir conditions, using supercritical CO_2 and H_2S, on samples of intercrystalline sandstone, carbonate shale and anhydrite rocks from the Wabamun and Zama areas in Alberta, where several acid gas injection operations exist. They observed that relative permeability curve Corey-exponents are generally much higher for the target gas phase than for the brine phase, and the maximum CO_2 saturation was 50% during drainage.

In the study of Benson et al. (2015), on CO_2-brine relative permeability functions, the following observations were made. Based on numerical simulation results, both unsteady-state and steady-state methods can provide reliable relative permeability measurement

results for CO_2 saturation below 30% and for homogeneous rocks. However neither of the measurement methods can provide accurate end-point saturation values. As there is relatively high interfacial tension and unfavorable mobility ratio between CO_2 and brine, the necessary capillary pressure for reaching high CO_2 saturations and/or end-point water saturation is difficult to achieve with such core-flood experiments. So the resulting high irreducible water saturation $(> 40\%)$ and the low end-point CO_2 permeability $(< 50\%)$ might be an artifact of unsuitable measurement technique.

The following figure illustrates the pressure and temperature conditions under what CO_2-brine relative permeability measurements were performed, reported from literature. On the right side, all published CO_2-brine drainage relative permeability curves are superimposed onto one plot. One can observed the high CO_2 residual saturation, and low end-point CO_2 relative permeability described before.

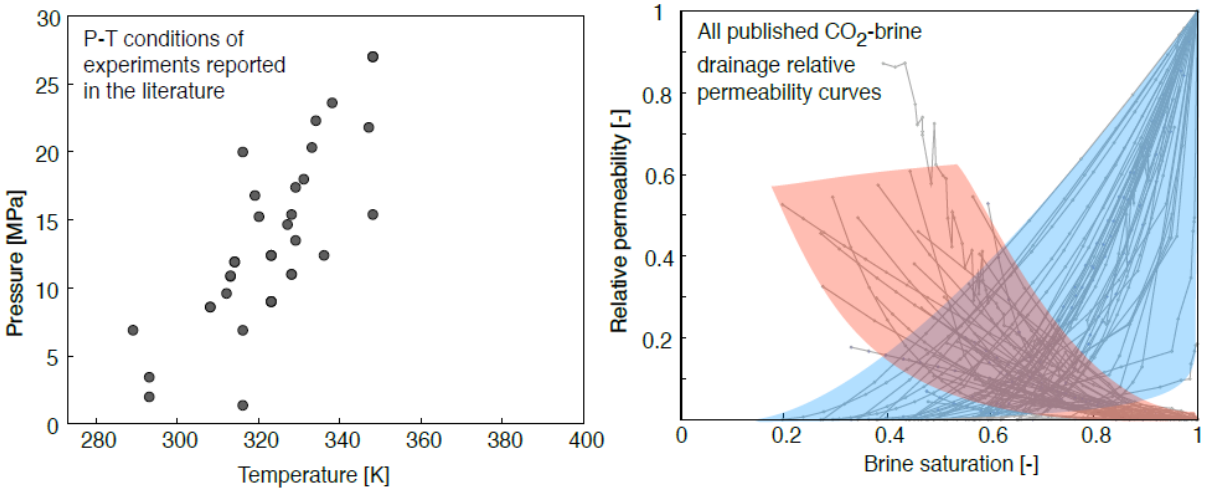

Figure 5.3 Pressure and temperature conditions of all of the drainage CO_2-brine relative permeability measurements reported in literature, with many experiments repeated at the same conditions, but on different rock samples. Right: all the relative permeability curves superimposed onto one plot (Benson et al., 2013).

More accurate results could be provided by stationary-liquid or centrifuge methods. In centrifuge method, the measurement of wetting phase production takes place at several angular velocities (Christiansen et al, 1995). When the angular velocity kept constant, the wetting phase is produced until equilibrium is reached between the capillary pressure and centrifugal force. The relative permeability data is derived from the non-equilibrium data, for instance the production of the wetting phase, meanwhile capillary pressure is determined based on the equilibrium wetting saturation data within the core at multiple centrifuge speed. In case of stationary liquid method, the relative permeability of a phase (generally gas) is measured in a rock sample with known immobile fluid saturation. The relative permeability curve is obtained by repetition of the permeability measurements at different known saturations. The disadvantage of this measurement technique is that the relative permeability curve development is only possible for the mobile phase.

In the study of Benson et al. (2015), several experiments were performed examining the influence of typical CO_2–brine interfacial tension values (from 35 to $65\ mN/m$) on the relative permeability curves. The alteration of CO_2-brine interfacial tension with pressure and temperature is illustrated in Fig. 5.4.

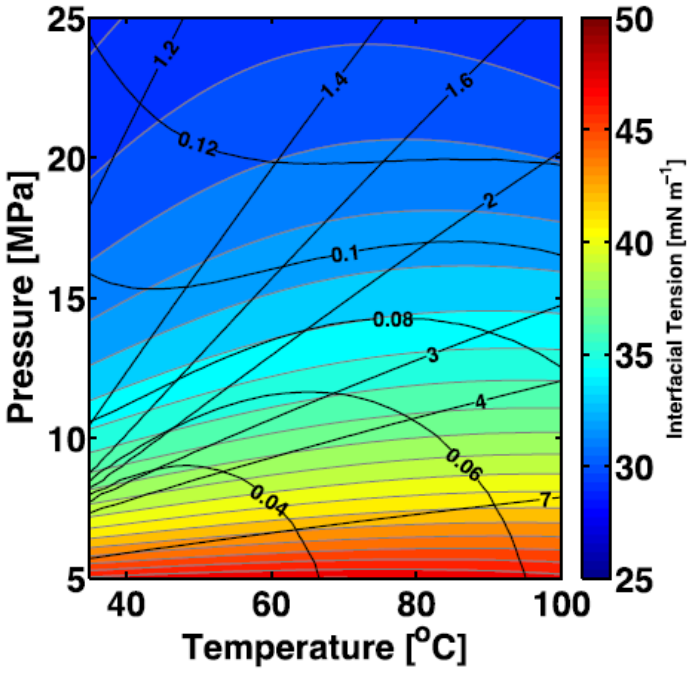

Figure 5.4 CO_2-water interfacial tension map with constant density (straight lines) and viscosity (curving lines) ratio superimposed as a function of pressure and temperature (Benson et al., 2015)

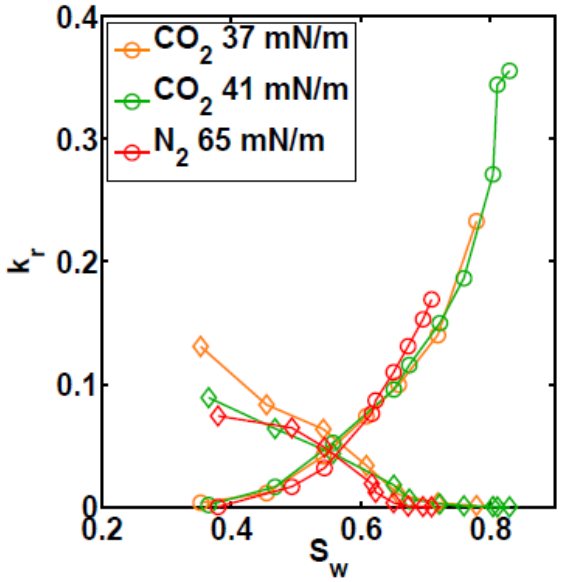

Figure 5.5 CO_2-brine and N_2-brine relative permeability curves with different interfacial tension values (Benson et al., 2015)

The study suggests that interfacial tension, within the relevant interval, of CO_2-brine system has no major effect on the relative-permeability curves. Some experimental results are shown in Fig. 5.5. The relative permeability curves are identical, regardless the applied interfacial tension between CO_2-brine.

5.2 Relative permeability model applied in the simulation cases

With the utilization of reservoir simulators, history matching of the measured data can be performed. There are a variety of possible relative permeability functions to be used for describing relative permeability; Berg et al. (2013) used an extended Corey-model for sandstone rock-type (Corey, 1954):

$$k_{r,w} = k_{r,w}(S_{nw,r})\left(\frac{S_w - S_{wcon}}{1 - S_{wcon} - S_{nw,r}}\right)^{n_w} \tag{5.1}$$

$$k_{r,nw} = k_{r,nw}(S_{wcon})\left(\frac{1 - S_w - S_{nw,r}}{1 - S_{wcon} - S_{nw,r}}\right)^{n_{nw}} \tag{5.2}$$

where S_{wcon} and $S_{nw,r}$ are the residual wetting and non-wetting saturations, and $k_{r,nw}(S_{wcon})$ and $k_{r,w}(S_{nw,r})$ are the corresponding relative permeability endpoints. For a carbonate rock type, an extended study was performed by Ott et al. (2015), comparing several relative permeability models, for the displacement of brine by CO_2. The experiments were performed using the USS technique. Based on those results, the best match for CO_2-brine displacement primary drainage relative permeability modelling was achieved by Corey-functions. For this thesis, it is important to note, if S_{wcon} and S_{wcrit} are taken to be different, Eq. 5.1 and 5.2 has to be used with S_{wcrit} instead of S_{wcon}.

5.3 Capillary pressure function scaling for testing different brine-CO_2 interfacial tension values

Mercury injection capillary pressure measurements are often performed in order to determine the drainage capillary pressure function for a given rock sample. In that case the resulting capillary pressure curve is for mercury-air system, as those two fluids are present. The following equation enables the utilization of the measured curve with the scaling of interfacial tension.

$$p_c(\sigma) = \frac{\sigma}{\sigma_{ref}} p_{c,ref} \tag{5.3}$$

Between mercury and air the average interfacial tension is $480\ mN/m$, meanwhile a typical interfacial tension value for CO_2-brine is $30\ mN/m$, and as it was mentioned previously previously was mentioned, is function of pressure temperature and brine salinity.

6 The unimodal versus bimodal pore-size distribution

Knowing the pore geometry of a reservoir rock type is essential to understand the fluid dynamics of the given system. One can further categorize porosity based on the pore throat size, for what there are several classification systems available. A good approximation is to take the boundary between macro and micro-porosity at $1\ \mu m$ pore throat radius.

Fig. 6.1 illustrates two typical examples for unimodal and bimodal pore systems. The Berea sandstone has the majority of its pore volume within the macro-porosity range, meanwhile the Estaillades limestone, shows a typical bimodality with inter-granular macro-porosity and micro-porous grains. In the Estaillades, because of the substantial amount of pore volume is within the micro-porosity range present, differences on the MICP measurements compared to the Berea sample can be observed, as higher mercury injection pressure is required in order to invade the micro-porosity. In rocks containing micro-porosity, a lower CO_2-brine displacement efficiency is expected, than in the rocks having the same effective porosity, but no micro-porosity. This leads to higher residual brine saturation, so lower storage capacity of micro-porosity bearing carbonate rocks and longer CO_2 plume migration distances (Ott, 2015a).

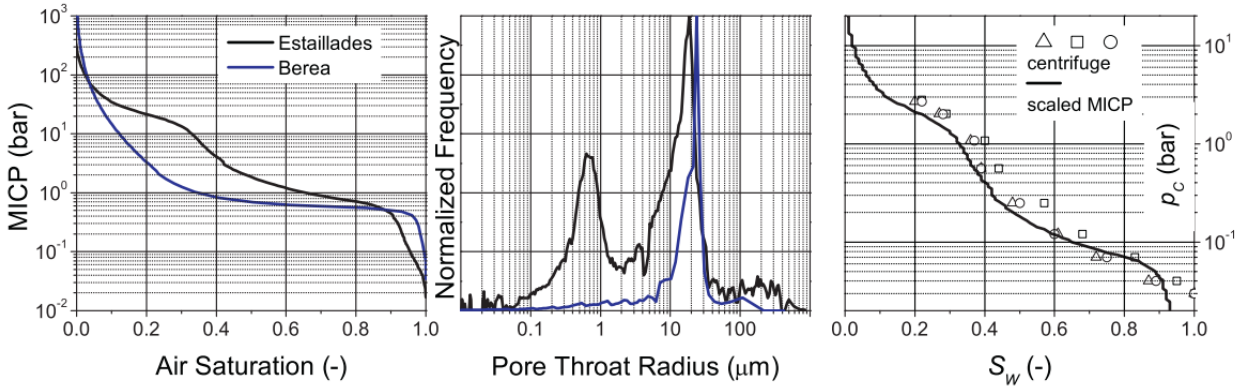

Figure 6.1 Left: MICP curves of Estaillades limestone and Berea sandstone. Middle: normalized pore throat distribution of the same rock types. Right: Decane–brine primary drainage capillary pressure curve of three different Estaillades plugs obtained by centrifuge measurements and the respective MICP curve scaled by interfacial tension (Ott et al. 2015)

As in a CO_2-brine system CO_2 is the non-wetting phase, the viscous forces has to overcome the capillarity, so that micro-pores could be invaded. The capillary entry pressure can be estimated from the pore throat radii by $p_c = 2\sigma/r$. If the assumption is made, that the macro-pores are invaded prior to the micro-pores, the wetting aqueous phase is no extensively longer interconnected. Since CO_2 forms a connected phase, one can estimate the viscous pressure drop on the trapped brine phase within a single micro-porous grain by Darcy's law (Ott et al., 2015). So CO_2 can invade to the micro-pores if:

$$\frac{l_{grain} \cdot \mu_{CO_2} \cdot v_{Darcy}}{k} \geq \frac{2\sigma}{r} \qquad (6.1)$$

The required v_{Darcy} to invade micro-porosity can be estimated knowing the general conditions and parameters of CO_2 sequestrations, and it is 3 to 4 orders larger, even in near wellbore, than realistic injection flow velocities (Ott et al., 2015). On the other hand, micro-porosity might be able to be invaded by buoyant forces. It can occur, if buoyancy is able to overcome capillary forces which is possible under the following condition:

$$\Delta\rho g h \geq \frac{2\sigma}{r} \tag{6.2}$$

Similarly to hydrocarbon migration to the reservoir rock, CO_2 can displace brine even in micro-pores by buoyant forces, if this condition is fulfilled. In case of relevant CO_2 density $(300 - 500\ kg/m^3)$ and CO_2-brine interfacial tension range $(30 - 40\ mN/m)$, a minimum CO_2 column heights of $12\ m$ (for $r = 1\ \mu m$) to $250\ m$ (for $r = 0.1\ \mu m$) are required for CO_2 to enter micro-porosity. Such CO_2 column heights might be expected during storage operations, with higher CO_2 saturations at the top of the reservoir. As the micro-pores do not contribute to the CO_2 mobility, micro-porosity might act as a reservoir and might mitigate gravity overrun of the CO_2 plume (Ott el al., 2015). The way, how buoyancy acts below a seal is illustrated in Fig. 6.2.

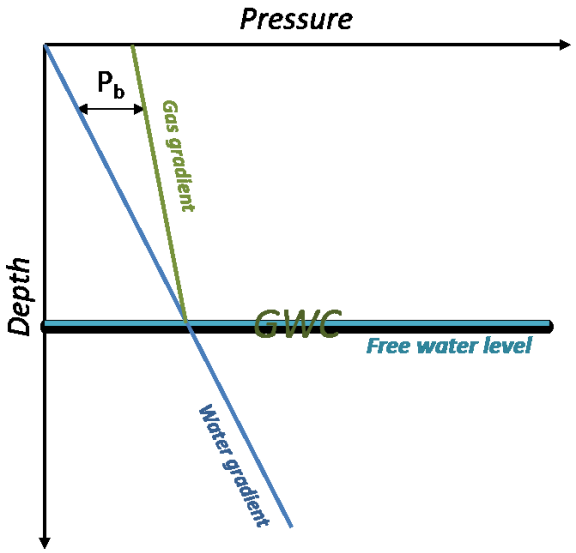

Figure 6.2 Buoyancy pressure (p_b) illustration

Generally, lower percentage of micro-porosity leads to improved permeability, and reservoir/aquifer quality in carbonate rocks. In the paper of Bennion and Bachu (2010), several carbonate samples were tested for CO_2-brine drainage relative permeability. The residual brine saturation was relatively high for all cases $(0.40 - 0.60)$. Their finding was that in the rock samples from the same lithological unit, higher median pore size leads generally to higher porosity and permeability to brine and to less concave relative permeability curves. This might occurs due to sample heterogeneities, resulting in bypassing and channeling through more permeable paths. As a result, a lower value for CO_2 end-point relative permeability was observed for the samples having higher permeability.

7 Displacement instability

In case of CO_2 injection to deep saline aquifers instable displacement is likely to occur due to the contrast in fluid properties. The term fingering, means the bypassing of a resident fluid by a displacing agent, and does not include bypassing caused by permeability heterogeneities. The bypassing mechanisms induced by permeability variations are called channeling. However, channeling can be enhanced by the viscous instability of the displacement. Fingers are either caused by gravity forces (gravity fingers) or viscous forces (viscous fingers) (Lake, 1989). The source of instability is the viscous pressure gradient which leads to a steeper pressure gradient of the displaced phase ahead of the finger, which lets the finger grow (Berg and Ott, 2012). In the following picture, displacement instability, particularly viscous fingering is illustrated. For the case discussed in this thesis, Fluid 1 represents the more mobile CO_2 and Fluid 2 represents brine.

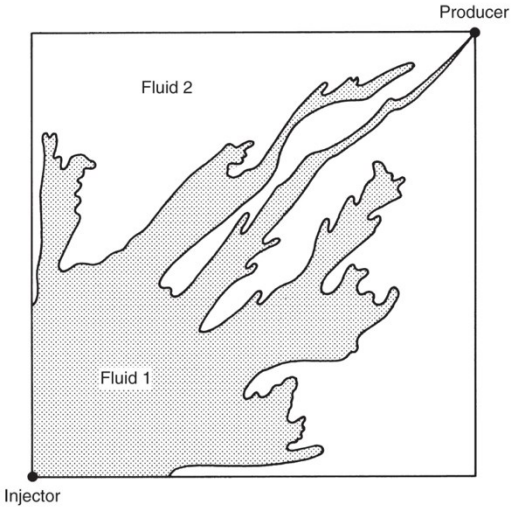

Figure 7.1 Front instability (Lake, 1989)

As an instable displacement front has a negative effect on sweep efficiency, so on the occupiable pore volume for CO_2 storage, it is critical to determine under what conditions a displacement gets instable. As during CO_2 injection to saline aquifers, the displacing CO_2 has the larger mobility, than the displaced brine, such instabilities are likely to occur.

7.1 Mobility ratio

According to the linear stability analysis (Chuoke et al., 1959), “when an initially planar interface between two immiscible liquids is displaced at a constant rate, u, normal to the front, instability will occur for all rates greater than the critical rate, u_{crit} given by:

$$\left(\frac{\mu_2}{k_2}-\frac{\mu_1}{k_1}\right)\cdot u_{crit}+(\rho_2-\rho_1)\cdot g\cdot\cos(zz')=0 \qquad (7.1)$$

provided the Fourier decomposition of spatial perturbation or deformation of the moving displacement front contains modes with wavelengths, λ, greater than the critical wavelength, λ_{crit}," given by Eq. 7.2.

In other words, for immiscible viscous fingering, perturbations with bigger wavelength than the critical (λ_{crit}) can grow (Berg and Ott, 2012). For determining the critical wavelength Hele-Shaw cell can be used, which consists of two parallel plates with infinitely small gap. The critical wavelength in Hele-Shaw cells can be analytically calculated with the following equation;

$$\lambda > \lambda_{crit} = 2\pi \cdot \sqrt{\frac{\sigma}{\left(\frac{\mu_2}{k_2} - \frac{\mu_1}{k_1}\right) \cdot (u - u_{crit})}} \qquad (7.2)$$

Where σ is the interfacial tension between the two phases, μ_1 and $\mu_2$are their viscosities, $k_1 = k_2 = k$ is the permeability of the Hele-Shaw cell (Fig. 7.2), u is the flow velocity and u_{crit} is the critical velocity (Feder, 1998). Large amounts of immiscible flow observations were performed in Hele-Shaw cells, and this stability criterion can be translated to porous media flows (Feder, 1998), despite of the different displacement nature.

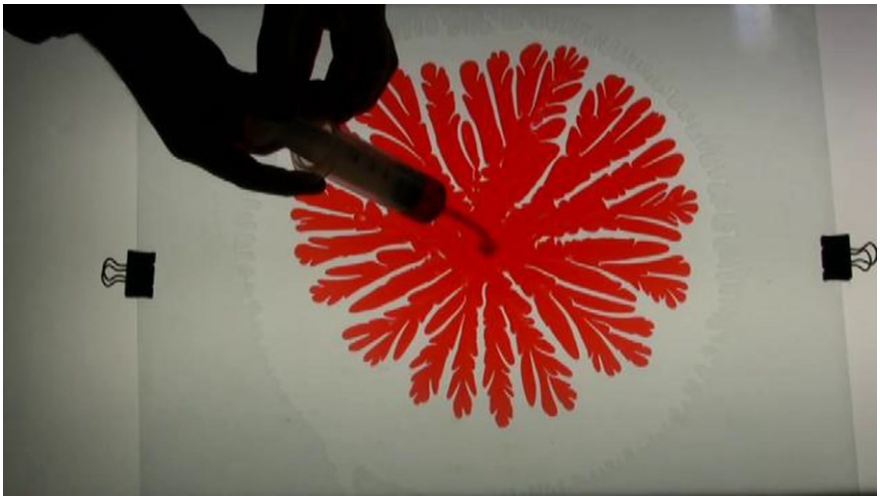

Figure 7.2 Hele-Shaw cell (Vimeo)

Meanwhile, in a Hele-Shaw cell, one phase is flowing in front of the displacing phase, in porous media immiscible displacement is characterized by simultaneous flow of both phases before and behind the front (Julio et al., 2003). For that reason, in order to assess displacement stability, mobility ratio was introduced, which means ratio of the mobilities of displacing (CO_2) and displaced (brine) phase:

$$M = \frac{k_{r,nw}/\mu_{nw}}{k_{r,w}/\mu_w} \qquad (7.3)$$

In case of horizontal flow, favorable, so stable displacement only occurs if the mobility ratio is larger than 1. Initially, for the relative permeability of the wetting and non-wetting phase, the end-point relative permeabilities were considered. In that case Eq. 7.3 is modified to:

$$M_e = \frac{k_{r,nw}(x \to -\infty)/\mu_{nw}}{k_{r,w}(x \to +\infty)/\mu_w} > 1 \qquad (7.4)$$

Where $x \to -\infty$ refers to a saturation where the displacing phase has reached its maximum saturation and $x \to +\infty$ refers to a saturation where the displaced phase has reached its maximum saturation. However, many authors doubt the validity of using end-point relative permeability (Berg and Ott, 2012). Recently, the commonly accepted concept is to use the shock front relative permeability, as it is illustrated in Fig. 7.3.

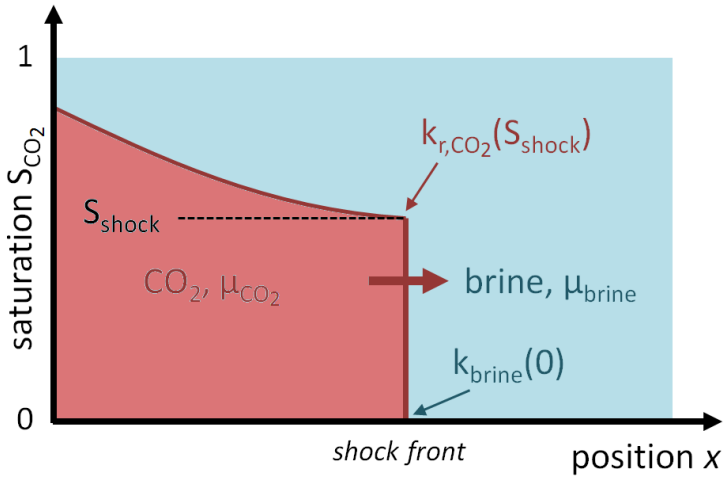

Figure 7.3 Immiscible displacement of brine by CO_2 (based on Berg and Ott, 2012)

For that case Eq. 7.3 for CO_2 brine system can be written in a form of:

$$M_s = \frac{k_{r,CO_2}(S_{shock})/\mu_{CO_2}}{k_{r,brine}(S_w = 1)/\mu_{brine}} > 1 \qquad (7.5)$$

The main difference between the M_e and M_s criteria is that M_e indicates instability in more cases than M_s. If both the end-point relative permeability equal to 1, for any cases, when the viscosity of the displaced fluid is larger than the displacing fluid, instability will be indicated by M_e, even if the displacement under the given condition would be stable (Berg and Ott, 2012).

In Fig, 7.4, shock-front mobility ratio is plotted as a function of Corey-exponents, where n_{CO_2} and n_{brine} correspond to n_{nw} and n_w from Eq. 5.1 and Eq. 5.2 respectively. The displacement stability map as a function of Corey-exponents, for primary drainage and $p_c = 0$, was determined based on Buckley-Leverett method. For the calculation and numerical simulations $\mu_{brine}/\mu_{CO_2} = 20$, $S_{wcon} = 0.2$, $S_{CO_2,r} = 0$ and $k_{r,brine}(S_w) = 1$ were used. On the left side, $k_{r,CO_2}(S_w = S_{wcon}) = 1$ was used for better representation of stability and instability

transition, meanwhile on the right-hand side a k_{r,CO_2} of 0.5 was utilized, which represents the best experimental result of core-flood measurements (Berg et al., 2013). Red line indicates the boundary between stable and unstable displacement (the shock-front mobility ratio of 1).

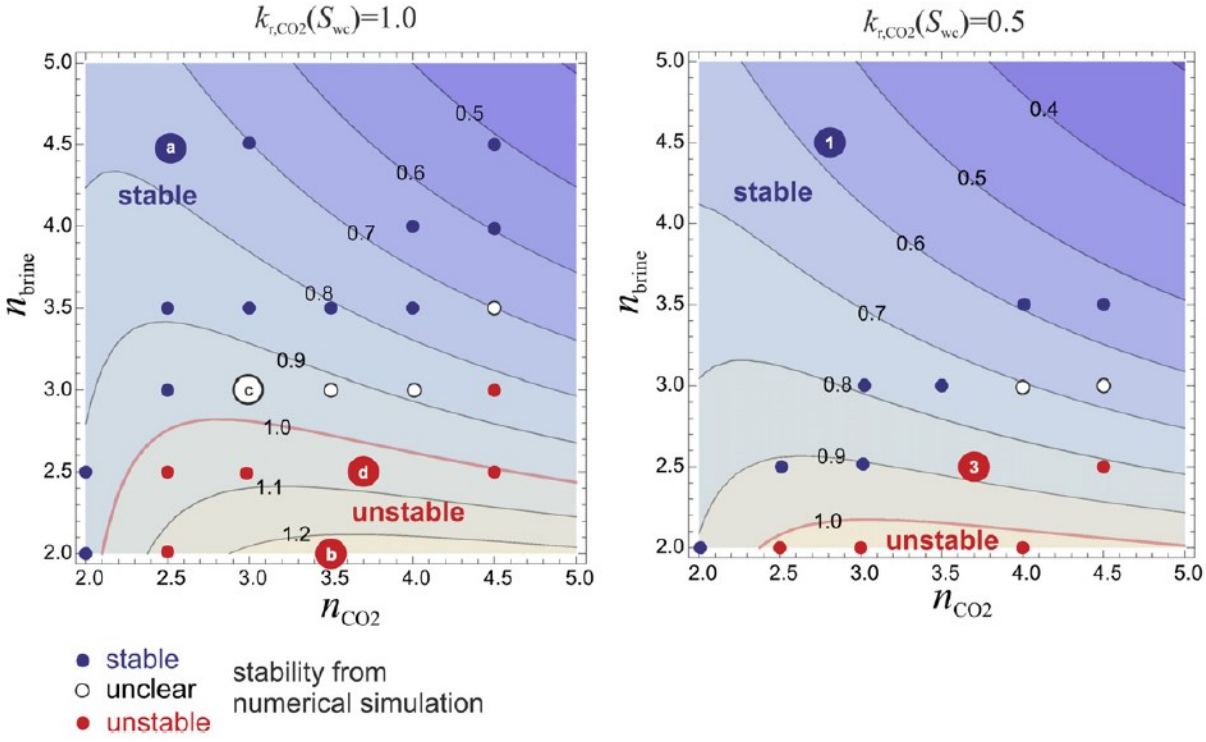

Figure 7.4 Shock-font mobility ratio $M_s$and displacement stability map as a function of Corey-exponents (Berg and Ott, 2012)

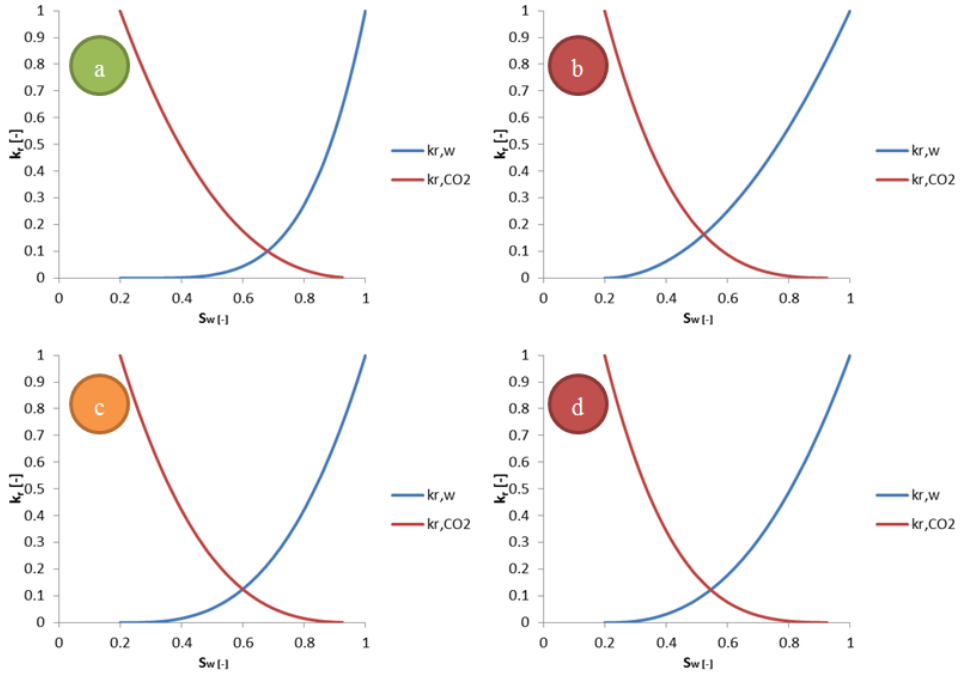

Figure 7.5 Relative permeability curves with $S_{wcon} = 0.2,\ S_{CO_2,r} = 0\ and\ k_{r,brine}(Sw) = 1$ (Brooks & Corey)

Based on the publication of Berg and Ott (2012), numerical simulations for four distinct cases (in Fig. 7.5; a, b, c and d) were tested in CMG IMEX to demonstrate the effect of the Corey-exponents on viscous stabilities. The conditions of the simulations are explained in Chapter 8. The results of the simulations and the transition between stable to unstable displacement with the modified Corey-exponents are illustrated in Fig. 7.6.

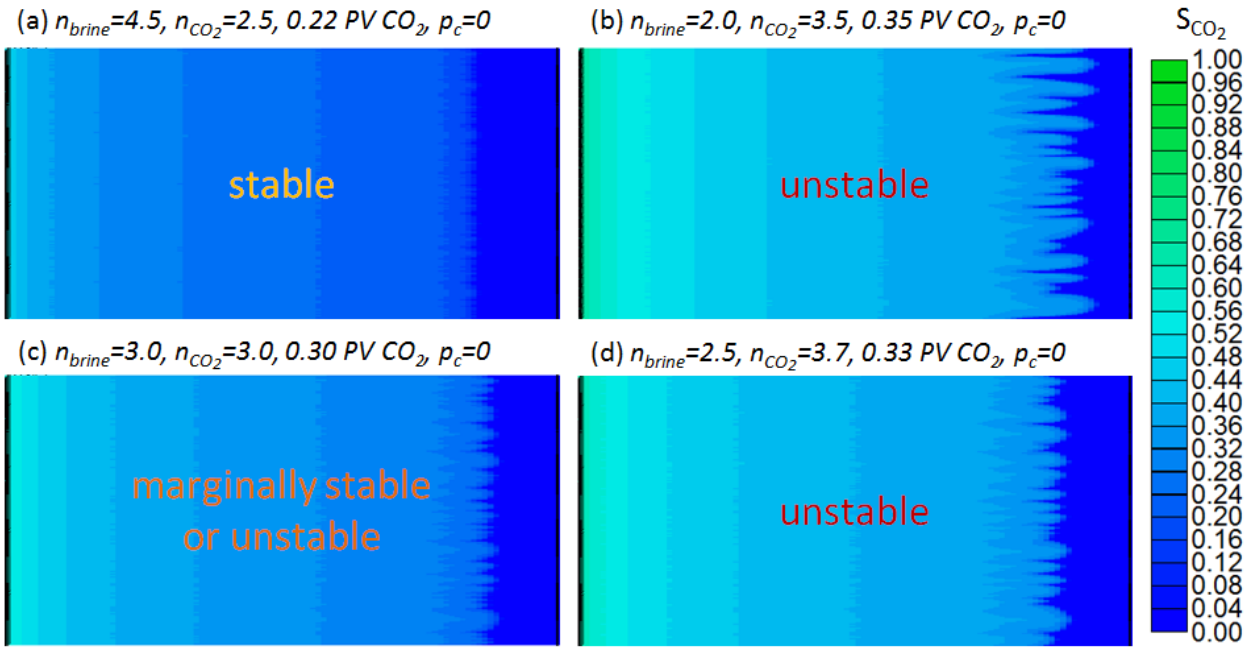

Figure 7.6 Simulation models for $k = 100 \pm 2mD$ neglecting capillary forces and gravity with a μ_{brine}/μ_{CO_2} of 20 (own simulation reproducing the results of Berg and Ott, 2012)

7.2 Viscosity ratio effects

From the term mobility ratio, it is evident, that the lower the viscosity ratio between displacing and displaced phases, the likelihood of instable displacement increases. To observe the effects of viscosity ratio, simulations were run with the modification of it. The results are presented in Fig 7.7. It is visible that the larger the viscosity contrast, the smaller the wavelength is, and more elongated the fingers are, as a consequence of larger finger growth rate.

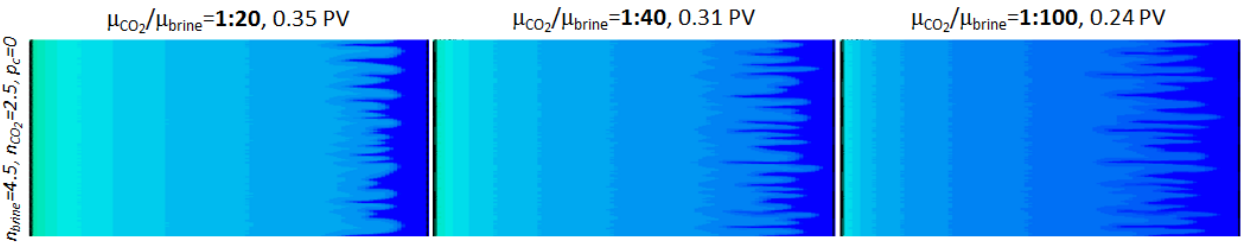

Figure 7.7 Fingering pattern with the viscosity ratio of $1:20$, $1:40$ and $1:100$, and $p_c = 0$, neglecting gravity (own simulation reproducing the results of Berg and Ott, 2012)

7.3 Effect of capillary pressure

Capillary forces have stabilizing effect on the growth of viscous fingering, so they are assisting to the stability of the displacement, but only on relatively short length-scales. That equals to the same length-scale as the shock-front is dispersed due to capillary forces as shown in Fig. 7.8.

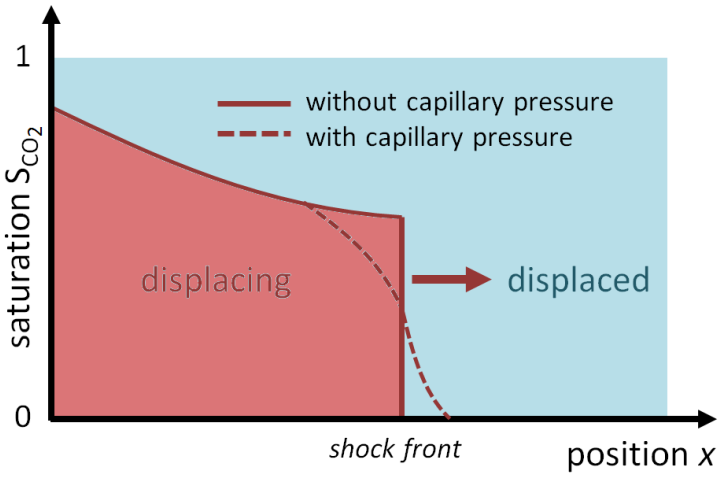

Figure 7.8 Capillary effect on shock-front (adapted by Lake, 1978)

The sharpness of the shock-front is basically dependent on the ratio of viscous to capillary forces, described by the capillary number:

$$N_{cap} = \frac{\mu_w \cdot v_{int}}{\sigma} \tag{7.6}$$

Locally, flow in porous media is generally considered to be capillary dominated. On a longer scale it is typically viscous dominated. To account for the length-scale dependency of capillary stabilization, the onset of fingering is better described by the macroscopic capillary number (Hilfer and Oren, 1996):

$$N_{cap}^{M} = \frac{\mu \cdot v_l \cdot L}{\overline{p_c}.\, k} \tag{7.7}$$

where $\overline{p_c}$ is a characteristic capillary pressure, which has a value of $\approx 0.04\ bar$ in the study of Berg and Ott (2012).

Based on the work of Berg and Ott (2012), some simulations were repeated to observe the effect of different IFTs on viscous fingering, and the transition from stable to instable displacement. The results are displayed on Fig. 7.9.

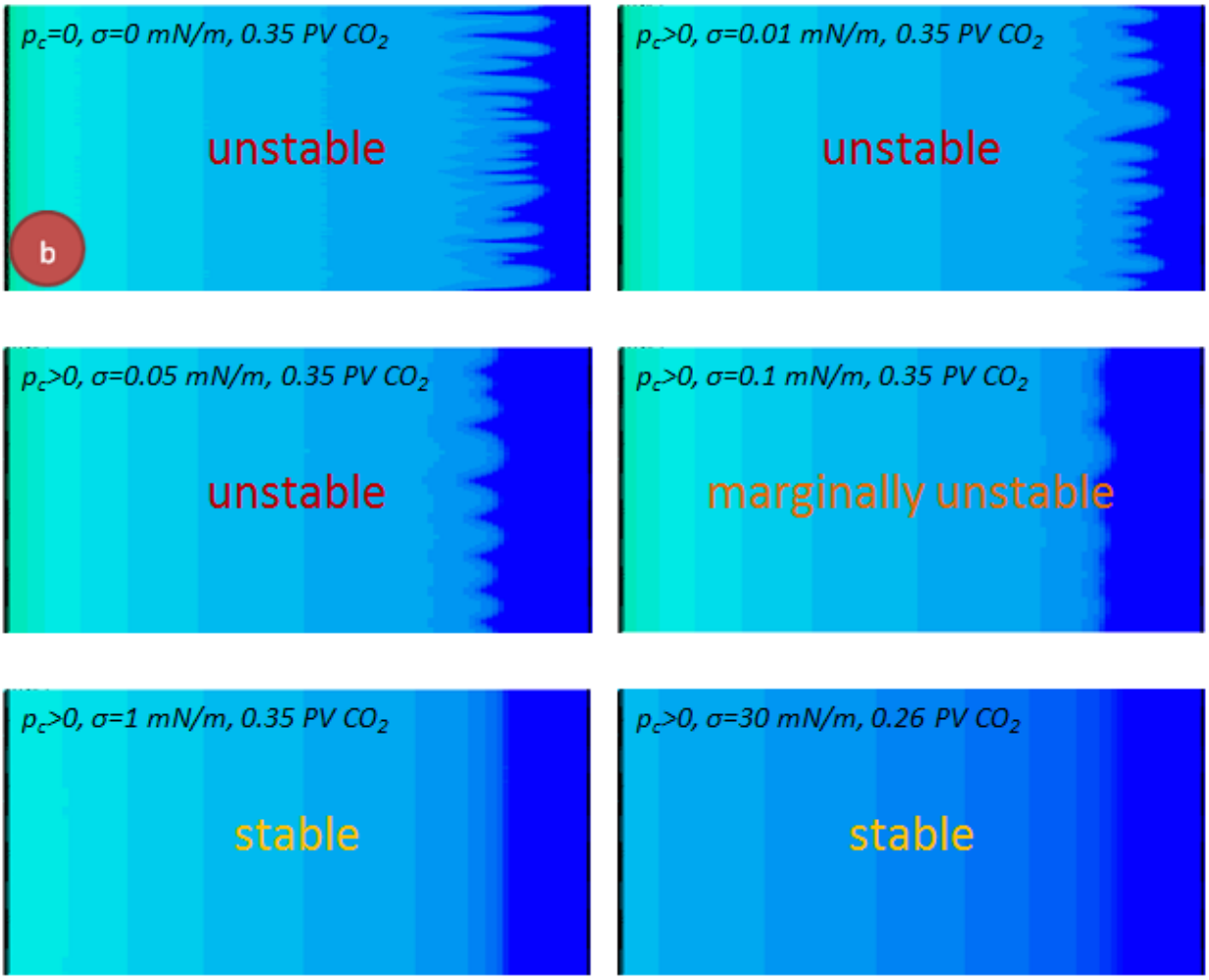

Figure 7.9 Transition between unstable to stable displacement with the modification of p_c with relative permeability model "b" (based on Berg and Ott, 2012)

For the different core-scale numerical simulations, the Berea capillary pressure function (Fig. 8.4) was scaled by the gradually increased IFT. For the relative permeability model the earlier mentioned Brooks and Corey (Eq 5.1 and 5.2) was used, with the coefficients of $n_{CO_2} = 3.5$ and $n_{brine} = 2$. A viscosity ratio of 20 was assumed and a flow rate of $0.25\, ml/min$. Without capillary pressure taken into account, unstable displacement can be observed. As the interfacial tension was increased from $0\, mN/m$ to $0.01\, mN/m$ and to $0.05\, mN/m$, the displacement remained unstable, but wavelength of fingering increased substantially, accordingly to Eq. 7.2. With further increasing the IFT, the displacement becomes marginally stable then it is stabilized.

7.4 Gravity effects

The relation between gravity and viscous forces are given by the gravity number, what is defined by Anton and Hilfer (1999) and Riaz and Tchelepi (2004) as:

$$N_{grav} = \frac{k \cdot g \cdot \Delta\rho}{\mu \cdot v_l} \qquad (7.8)$$

If $N_{grav} \gg 1$, gravity overrun can be expected. If $N_{grav} \ll 1$ the flow gets more dominated by viscous forces. As CO_2 even at supercritical conditions has significantly less density than brine ($0.41\ g/cm^3$ and $1\ g/cm^3$ were used for the experiments reported by Berg and Ott, 2012), gravity will have a great effect on the plume migration.

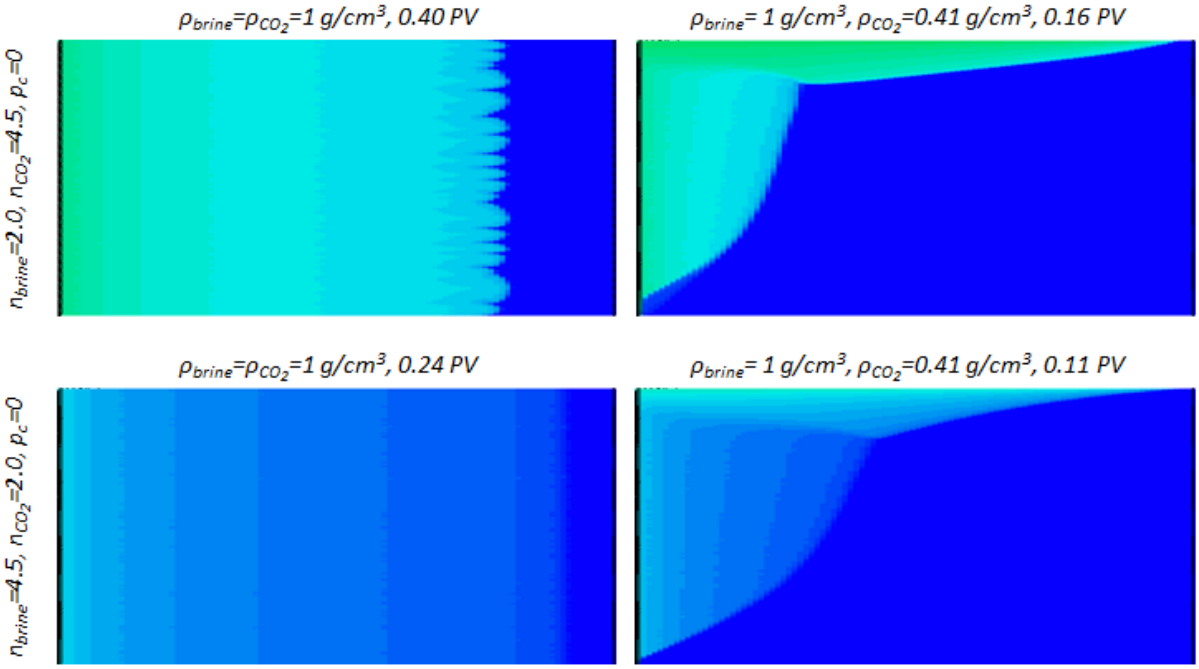

Figure 7.10 Unstable (top) and stable (bottom) displacement with (left) and without (right) gravity effects

To detect the effects of gravity on plume migration, Berg and Ott (2012) ran several core-scale numerical simulations. The Corey-exponents were modified to achieve stable and unstable displacement in viscous means. On the right figures, gravity effects were included by attaching different density values to the two phases. Those values equal to the conditions reported by Berg end Ott (2012). As the gravity effects were included, gravity override can be observed on Fig. 7.10.

8 Simulation models and results

8.1 The applied simulator tool

To perform the necessary numerical simulations for this thesis, the IMEX module of CMG software package was used, which is a three-phase black-oil simulator developed by the Computer Modelling Group Ltd, including gravity and capillary terms. CMG consists of the following three modules:

- IMEX: three phase black-oil simulator
- GEM: compositional simulator
- STARS: non-isothermal simulator

For the simulations, performed in this thesis, a black-oil simulator like IMEX is suitable as it enables the modeling of displacement instabilities in case of immiscible displacement. A black-oil model has the advantages over a compositional model that it has more reliable performance and takes less computational effort.

For a black-oil model, in general, pressure dependent tables of the formation volume factor and viscosity of the fluids of interest have to be created to model phase property variations with changing conditions.

The basis of the reservoir simulations performed in this thesis is that the whole volume of interest is primarily flooded by brine. That was achieved by setting the water-oil or gas-oil contact to be above the depth of the top of the reservoir $(1000\ m)$. Then the in place brine was displaced by the injection of CO_2.

8.2 Geometry of the reservoir simulation models

The 2D models have the following geometry and boundary conditions, illustrated in Fig. 8.1:

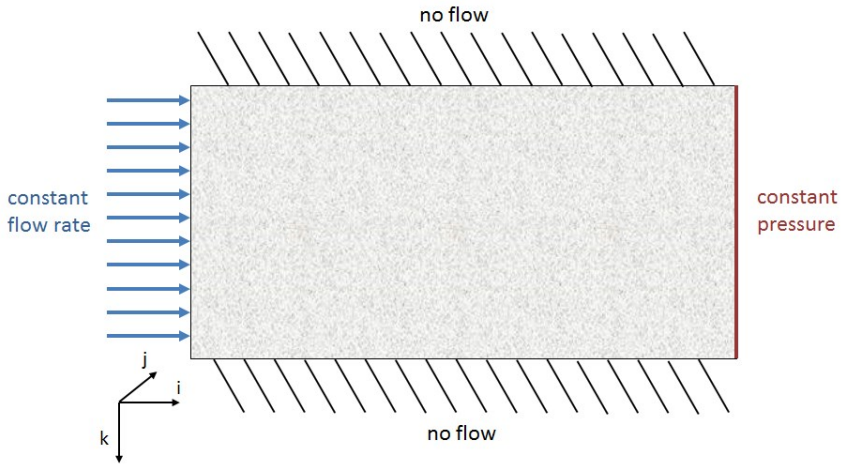

Figure 8.1 Boundary conditions of the 2D simulations

The constant rate boundary was created by a well perforated throughout the thickness of the reservoir, set to inject CO_2 with a constant rate, to achieve desired linear flow velocity. The constant flow boundary was achieved by a producer well also perforated through the whole thickness of the reservoir, having the minimum bottom BHP to be set to $10\,000 kPa$, which equals the reference pressure at reference depth $(1000\,m)$. A grid with $100\,x\,1\,x\,200$ grid blocks was created, representing $\vec{\imath}, \vec{\jmath}\, and\, \vec{k}$ directions respectively, to provide sufficient resolution for viscous fingering. The total thickness in $\vec{\jmath}$ and $\vec{k}$ directions are equal, despite of the difference in the grid number, meanwhile in $\vec{\imath}$ direction it is double. Different length-scales were tested during the simulations, with the maintenance of the same aspect ratio.

For the simulations, basically an isotropic, homogeneous model was created. The porous medium representative for Berea sandstone with a porosity of 25% and permeability of $k = 100 \pm 2\, mD$ was created (Berg and Ott, 2012). The applied absolute permeability field is shown in Fig. 8.2 and Fig 8.3. The permeability field was randomized to enable the triggering of such disturbances like viscous fingers and the same randomization is used throughout the simulations. At the inlet side, a permeability of $k = 100 \pm 4\, mD$ was applied in order to allow for finger nucleation inside the rock and to avoid artifacts (Berg and Ott, 2012). The permeability in both $\vec{\imath}, \vec{\jmath}\, and\, \vec{k}$ directions were taken to be isotropic.

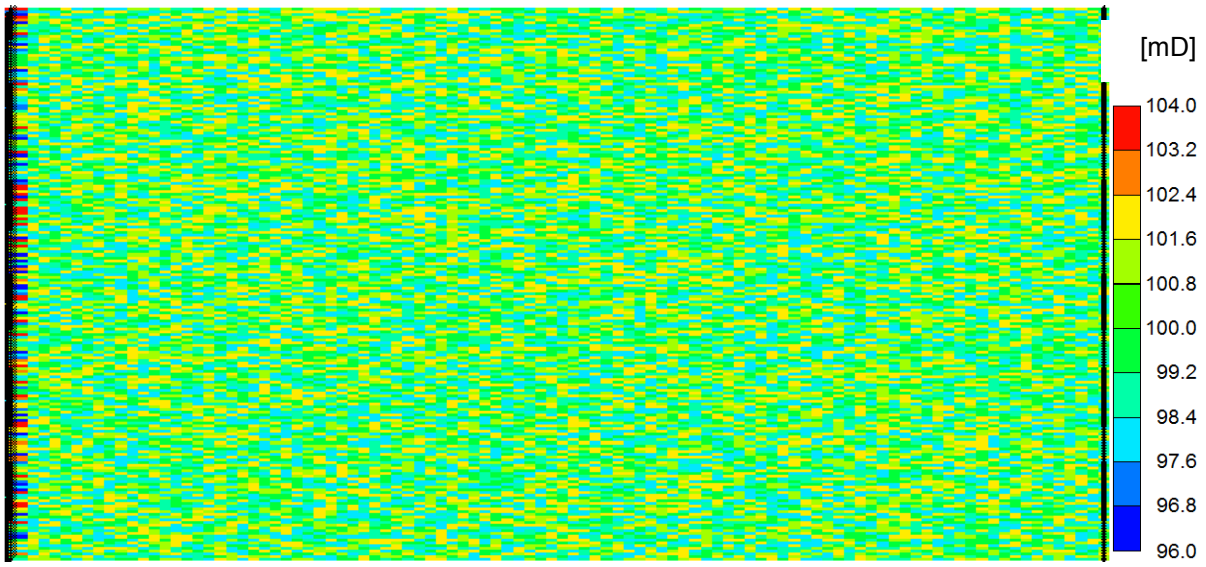

Figure 8.2 Applied permeability field in the 2D simulations

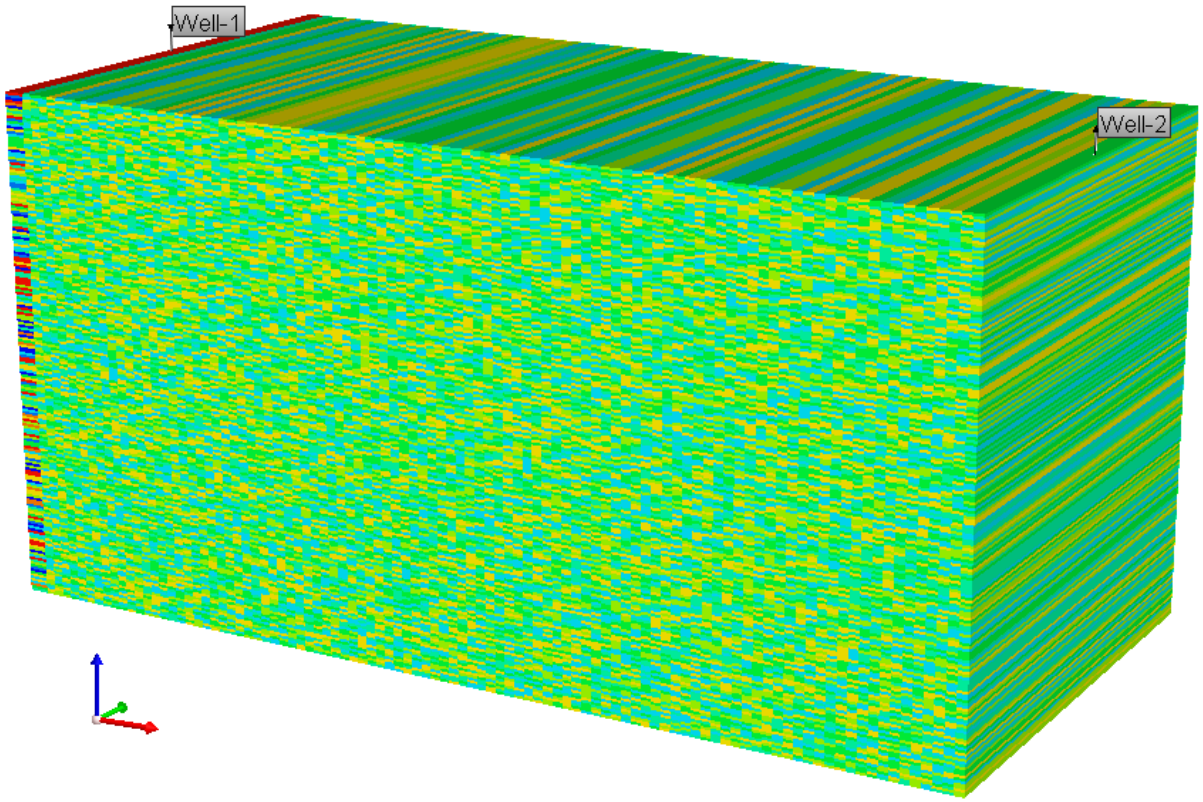

Figure 8.3 Applied permeability field in 3D view

8.3 Fluid property modeling

The reference temperature and pressure in the simulation experiments are $45\,°C$ and $10\,000\,kPa\,(100\,bar)$, representing realistic sequestration conditions as discussed earlier. For water compressibility in all cases the minimum default compressibility was used $(4.57\,x\;10^{-7}\,1/kPa)$, which can be considered negligible for these experiments. Moreover, as the reference water formation volume factor was given to be 1 at $10\,000\,kPa$, so that the water compressibility plays no role, especially in the case of smaller length-scales, when the height of the fluid column, so the pressure growth with depth, is small. The pressure dependency of water viscosity was set to be zero.

In case of immiscible flow, the density and viscosity contrast are the relevant fluid properties for modeling gravity and viscous instabilities. In this thesis some simulations were run with either including or neglecting gravitational forces. Excluding gravity from the simulations was done by making both CO_2 and brine having the same density at reservoir conditions $(1000\,kg/m^3)$. In IMEX it was performed by using a two-phase oil-water model, where oil represented CO_2, with a surface density of $1000\,kg/m^3$, and formation volume factor of 1 at the reference pressure. The necessity of modeling CO_2 as oil comes from the fact that CO_2 could not have such density at the tested condition. In case of the model excluding gravity forces, the following oil-model PVT table was implemented:

Table 8.1 Oil PVT table (with standard density of oil, $1000\ kg/m^3$)

p [kPa]	R_s [m^3/m^3]	B_o [-]	B_g [-]	μ_o [cp]	μ_g [cp]
10000	0.0000	1.0000	0.0050	0.03380	0.03380
20000	0.0001	1.0000	0.0049	0.03379	0.03379

In case of the models including gravity forces a gas-water two-phase reservoir fluid model was implemented. For achieving a better understanding on gravity fingering, CO_2 compressibility was not encountered. The CO_2 density was implemented by the formation volume factor calculated from Eq. 3.11. The pressure dependency of CO_2 and brine viscosity at each simulation case was neglected. The CO_2 density at reservoir condition is noted before each simulation; otherwise it was taken to be $410\ kg/m^3$.

Table 8.2 Gas PVT table (with a standard density of gas, $2\ kg/m^3$)

p [kPa]	B_g [-]	μ_g [cp]
10000	0.0049	0.03380
20000	0.0049	0.03381

8.4 Rock-fluid modeling

The applied CO_2-brine relative permeability curves were calculated based on the extended Corey-model described in Eq. 5.1 and 5.2. S_{wcon} was taken to be 0 for all cases. The S_{wcrit} was taken to be either 0.0 or 0.5 for examining its effect on CO_2-brine displacement simulation results. When S_{wcrit} is different, than S_{wcon}, the latter one has to be substituted by the former one, in Eq. 5.1 and 5.2. The S_{wcrit} is taken to be 0.5, because that is in alignment with the measured residual brine saturation from literature (based on those, water becomes immobile below relatively high water saturation in carbonate rock types). The relative permeability end-points are taken to be $k_{r,brine}(S_w = 1) = 1$ in all cases, as CO_2 injection to brine is a drainage process. For CO_2, $k_{r,CO_2}(S_w = S_{wcon})$ and $k_{r,CO_2}(S_w = S_{wcrit})$ were selected to be either 1 or 0.5. The shape of the relative permeability curves were modified with changing the Corey-coefficients of the extended Corey-model, representing different rock-types and wetting conditions. The used values are noted at each simulation round.

The presence of micro-porosity can be observed on the MICP measurements, where capillary pressure function shows a step-like increase, if plotted on logarithmic scale.

Some of the simulations were run with either including or excluding capillary pressure. The MICP measurement results of each p_c model applied in the reservoir simulation cases are presented in Fig. 8.4. The Berea sample is a well-sorted sandstone rock, and is serving as a base p_c. The Estaillades sample is a carbonate rock often used as a model for bimodal porosity distribution including micro-porosity. Due to the irregular shape of the Estaillades core sample, the performance of pressure closure correction was required.

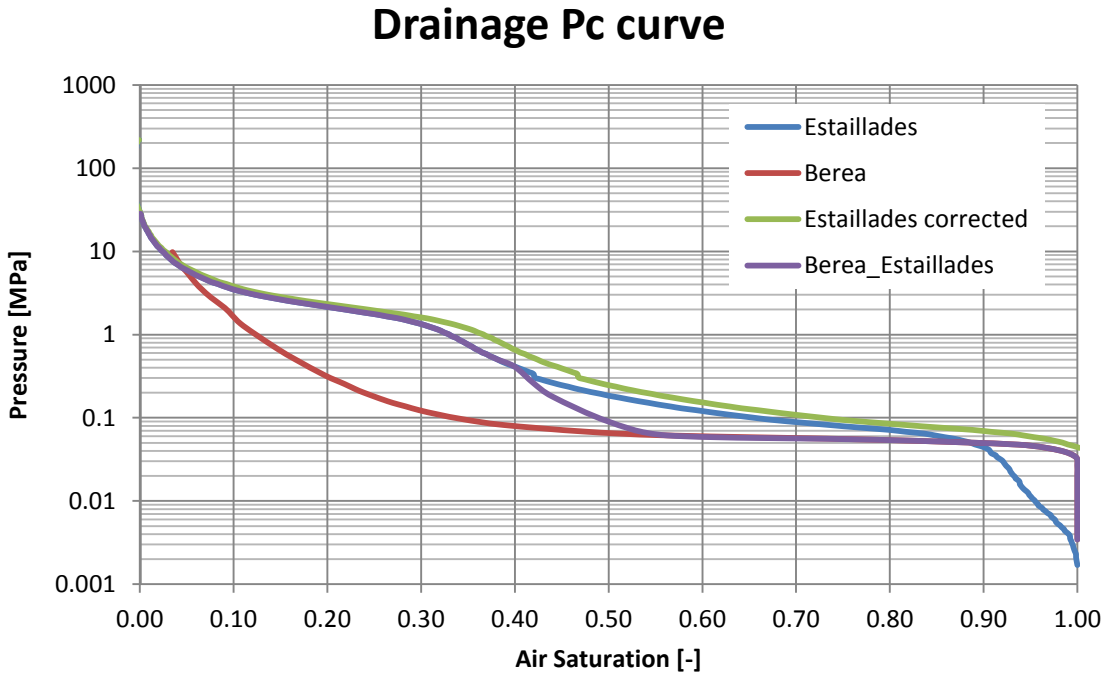

Figure 8.4 The applied MICP measurements

A simple approximation is to take the capillary pressure at the point of 90% air saturation, take it as it was for 100% air saturation, and stretch the capillary pressure curve, as it is shown in Fig. 8.4. As a third p_c case, an artificial one was created by merging the Berea and Estaillades measurements.

It is possible to scale MICP measurements by the interfacial tension, based on Eq. 5.3. A typical interfacial tension value for CO_2-brine system under reservoir condition is $30\ mN/m$, which was used in the following simulation experiments.

Using Eq. 3.7, the neccesary CO_2 column height to achieve a given saturation, by buoyancy forces can be determined. Firstly, the MICP measurements were scaled with an IFT of $30\ mN/m$ for the three p_c cases, then saturation versus height function was determined, and plotted (Fig. 8.5).

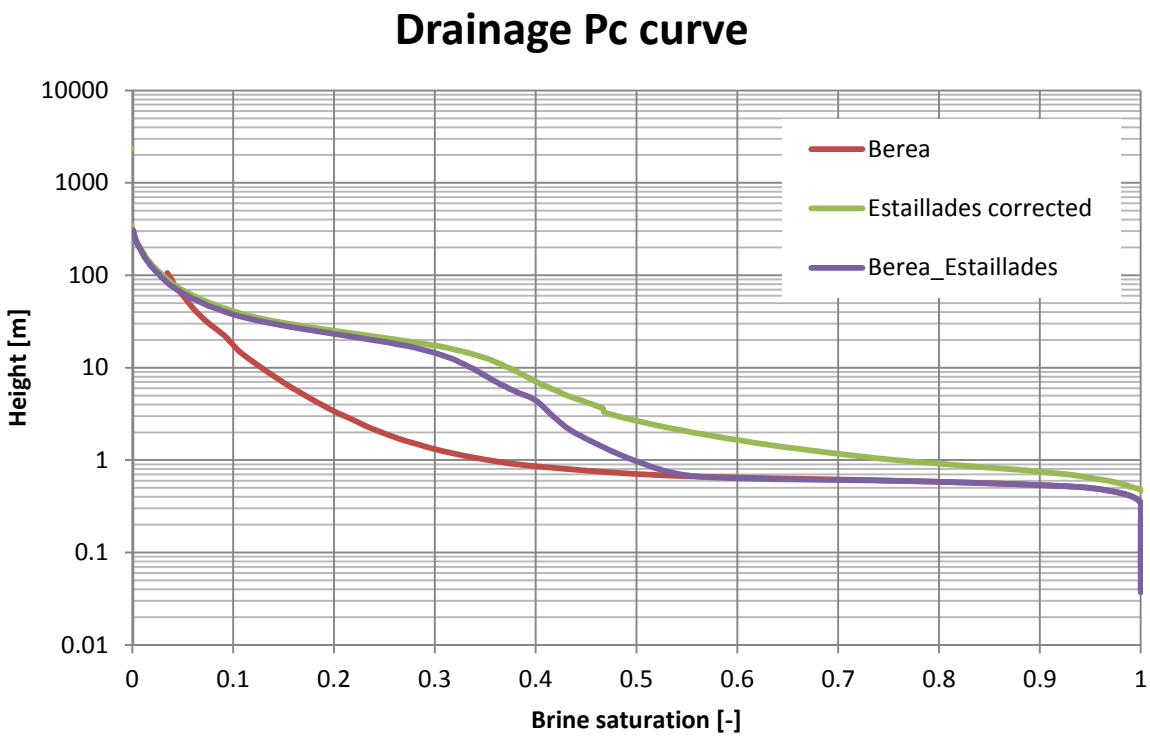

Figure 8.5 Drainage p_c curves scaled by an IFT of $30\ mN/m$, converted to saturation height function

To better illustrate the effect of capillary pressure function on the vertical phase saturation distribution, the three capillary pressure functions (scaled with $30mN/m$ interfacial tension) were implemented to CMG IMEX. That can also show at what CO_2 column height the invasion of micro-porosity can be expected.

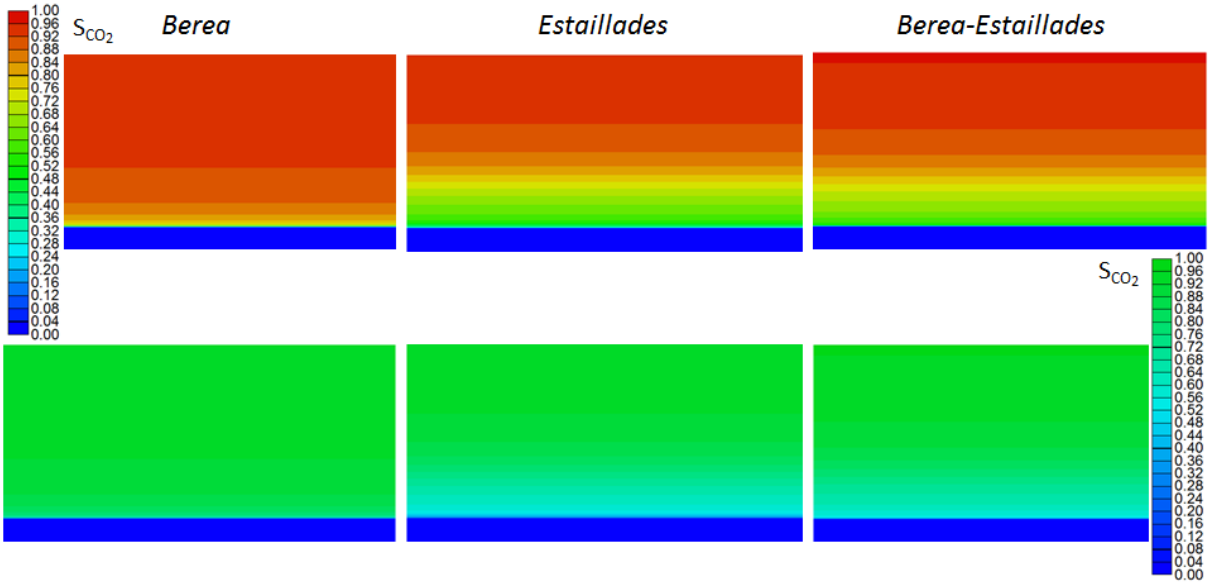

Figure 8.6 CO_2-brine capillary transition zones for three different cases, illustrated by two different color scales

The dimensions of this experiment were $180\,m$ in $\vec{\imath}$ and $90\,m$ in $\vec{k}$ direction, and the CO_2-brine densities were taken to be 410 and $1000\,kg/m^3$ at reservoir conditions respectively. CO_2 compressibility was no incorporated. The saturation initialization was done automatically, with a given CO_2-brine contact at $1080\,m$ and a reservoir top at $1000\,m$ depth. In Fig. 8.6, one can observe, how the presence of micro-porosity expands the transition zone between CO_2 and brine. In the case of the micro-porosity bearing Estaillades, the required buoyant forces to overcome capillary forces of micro-pores are higher, so for achieving the same CO_2 saturation, a higher CO_2 column is needed with accordance Eq. 6.2. That results in a a higher CO_2 saturation in of a given depth in case of the initialization with the Berea p_c curve, than with the Estaillades. For example, achieving a 0.9 CO_2 saturation, in case of Berea capillary pressure curve, an almost $30\,m$ less CO_2 column is required, than is the case of Estaillades.That also shows that the same volume of reservoir rock containing micro-porosity has less CO_2 storage capacity, than the one without, even with the same porosity. That can lead to CO_2 plume migration to longer distances in micro-porosity bearing rocks

8.5 Effect of micro-porosity on the $90\,m\,x\,180\,m$ model with $S_{wcrit} = 0.5$

The previous experiments had shown that already at that length scale, the presence of micro-porosity causes a drastic difference in the vertical saturation distribution of the phases. So the $90m\,x\,180\,m$ model could be appropriate for further investigation. For this sequence of simulations, the drainage relative permeability curve illustrated in Fig. 8.7 was used.

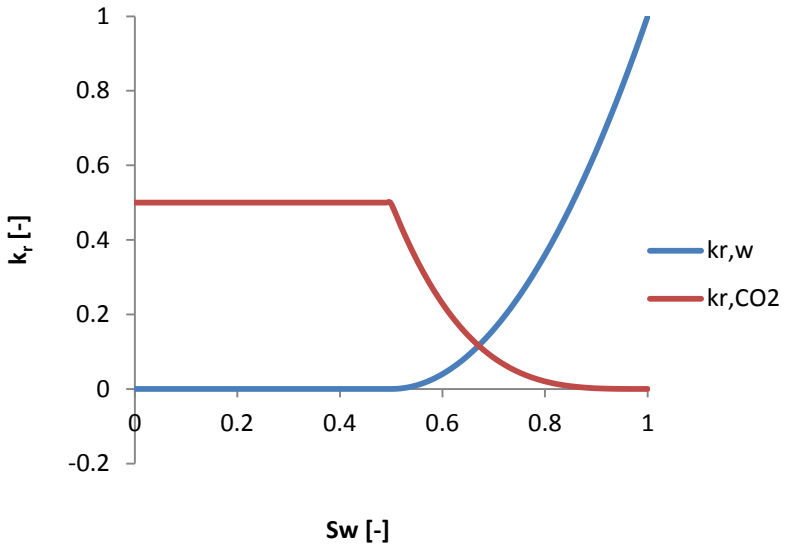

Figure 8.7 The applied relative permeability curve ($S_{wcon} = 0.0, S_{wcrit} = 0.5, n_{brine} = 2, n_{CO_2} = 3.5$)

The S_{wcrit} was taken to be 0.5, so that the occupation of micro-porosity with CO_2 would not happen by viscous displacement process. The end-point relative permeability of CO_2 was selected to be $k_{r,CO_2}(S_w = S_{wcrit}) = 0.5$ and $(S_w = S_{wcon}) = 0.5$. The applied Corey-exponents are $n_{brine} = 2$ and $n_{CO_2} = 3.5$, which will lead to a more instable displacement, as it can be observed on the stability map, based on Corey-exponents (Fig. 7.4).

The CO_2 PVT properties are summarized in Table 8.2; the B_g provided in the table results in a $410\ kg/m^3$ CO_2 density at reservoir conditions. This means a density ratio of 0.41. The viscosity of water was taken to be $0.674\ cp$ for all the coming simulation cases (after Berg and Ott, 2012); this gives a CO_2-brine viscosity ratio of $\approx 1:20$, being typical value for CO_2 sequestration projects. The other properties of the model are described in earlier paragraphs. In Fig. 8.8, the displacement front with the described model is shown, with an applied IFT of $0mN/m$. Then a sequence of simulations were performed including the MICP measurement results of the previously introduced Berea, Estaillades and their mixture scaled by an IFT of $30\ mN/m$ and implemented to IMEX.

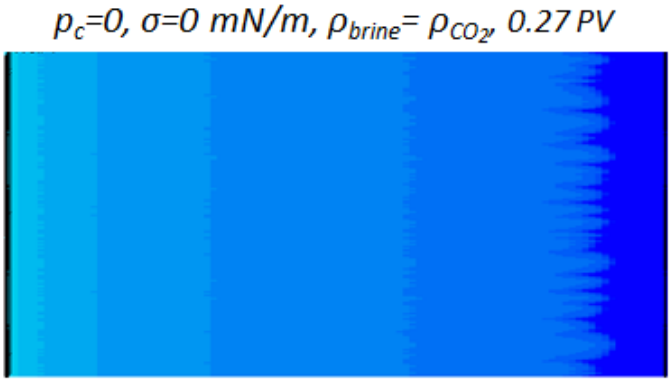

Figure 8.8 Simulation results excluding gravity

Two different linear displacement velocities were tested; one was $2.96\ x\ 10^{-6}\ m/s$, which is typical velocity for reservoir flows (Berg and Ott, 2012), the other is $7.4\ x\ 10^{-7} m/s$. These linear velocities result in a gravity number of ≈ 6 and ≈ 23 respectively. So the latter case results in a more gravity dominated system. A more gravity dominated system is expected to show more substantial effect micro-porosity on gravity fingering, as viscous forces play smaller role. Firstly, the simulation models of different linear velocities were run with neglecting gravity. The results are illustrated in Fig. 8.9. Secondly, simulations were run for the two linear velocities and including a CO_2/brine gravity ratio of 0.41, as can be seen in 8.10.

One can observe on the simulation sequence excluding gravity that the viscous fingering has shorter wavelengths, so the displacement is more instable in the case of higher linear velocity, which is in accordance with the macroscopic capillary number. Furthermore, it is clearly visible that Estaillades p_c suppresses the viscous fingering the most. This is because even in in macro-porosity range of capillary saturation function (not only in the micro-porosity range), the Estaillades has higher capillary pressure at a given water saturation interval, than Berea, which can be invaded by viscous forces according to the relative permeability curve. The simulation results with Berea and Berea-Estaillades p_c are identical, as they are equal in the brine saturation range of $0 - 50\ \%$.

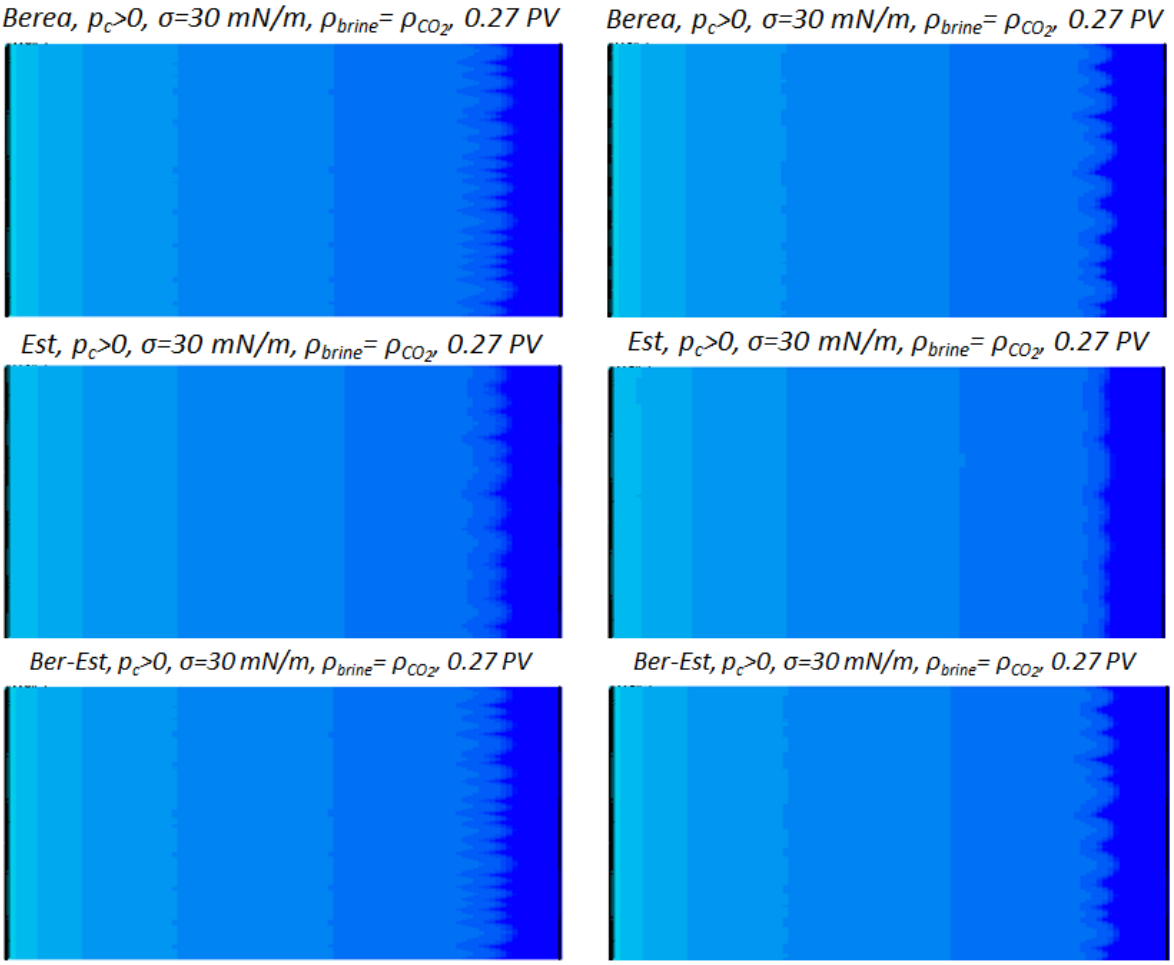

Figure 8.9 Simulation results neglecting gravity (linear velocity of $2.96 \text{ x } 10^{-6}$ m/s *on the left and* $7.40 \text{ x } 10^{-7}$ m/s *on the right,* $90\ m\ x\ 180\ m$*)*

In the simulation runs including gravity, but excluding capillary forces the viscous fingers are still noticeable in case of the higher linear velocity, which is less dominated by gravity. When the linear velocity is decreased, the system becomes more influenced by gravity and that leads to the suppression of viscous fingers, but to the elongation of gravity fingers. By decreasing the linear velocity of CO_2, the displacement becomes more instable gravity wise.

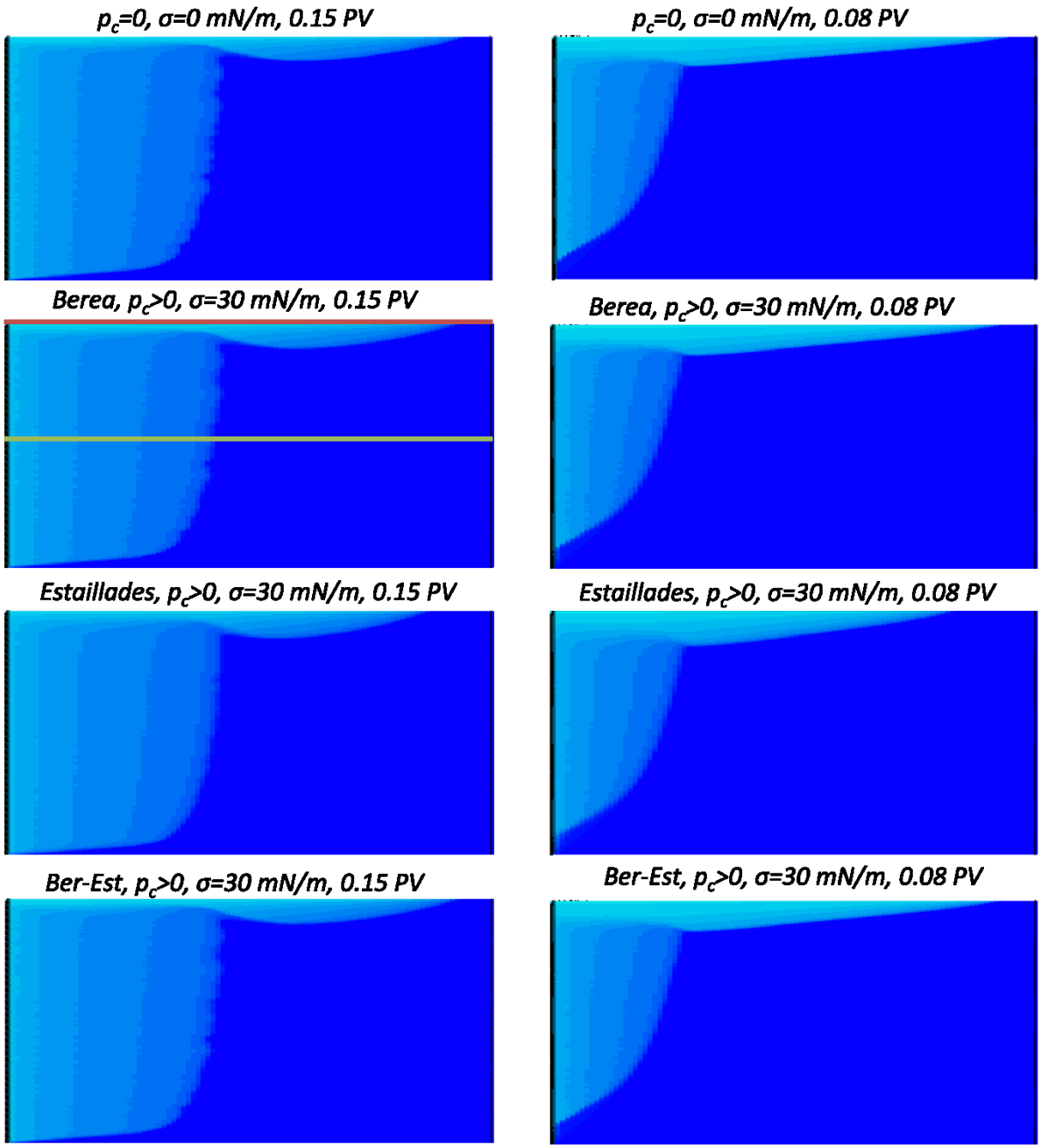

Figure 8.10 Simulation results with a gravity ratio of 0.41 *(linear velocity of* $2.96\ x\ 10^{-6} m/s$ *on the left and* $7.40\ x\ 10^{-7} m/s$ *on the right,* $90\ m\ x\ 180\ m$*)*

When both capillarity and gravity are encountered, there is a visible difference between the simulation runs with Estaillades or Berea capillary pressure curves. The Berea and Berea-Estaillades combination are seemingly identical just as in the case when gravity was neglected. In the case of Estaillades and higher linear velocity, the viscous fingering is smeared out. To quantify the differences between the six different simulation cases, the CO_2 saturation profiles of a given time step were plot along the two lines (top and mid), illustrated in 8.10. The results firstly, for the higher CO_2 displacement velocity cases are shown in Fig. 8.11:

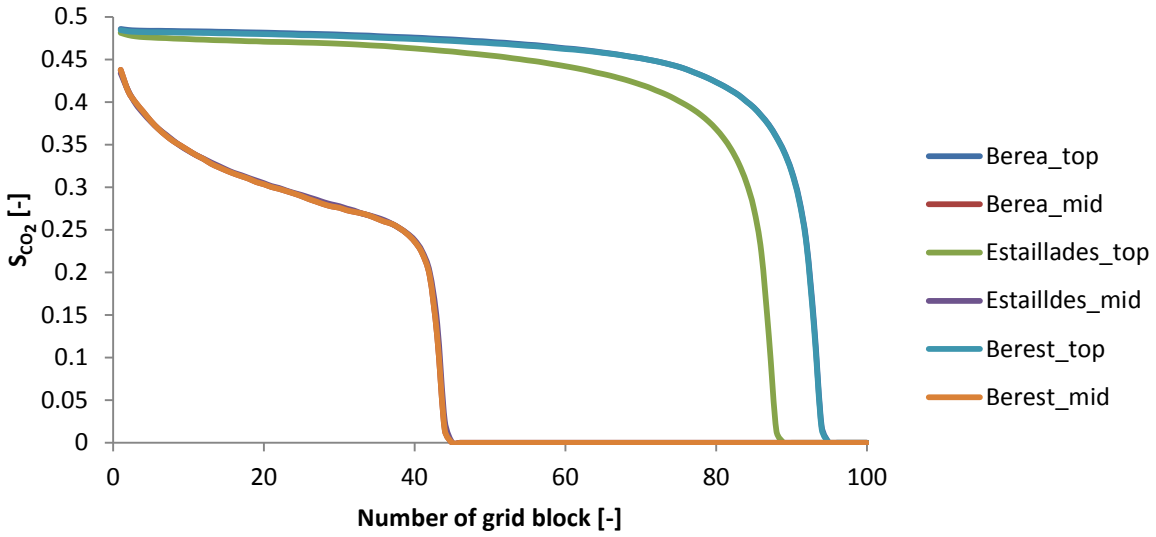

Figure 8.11 CO_2 saturation profile (linear velocity of $2.96 \text{ x } 10^{-6}$ m/s, $90\ m\ x\ 180\ m$*)*

As it was already noticeable, the simulations including the Berea and Berea-Estaillades mixture capillary pressure curves appear to have more elongated gravity fingers even at the same average CO_2 saturations, than the Estaillades one. Meanwhile, the saturation profile at the midline was the same for the three cases. The CO_2 saturation profiles for the lower linear velocity cases are shown in Fig. 8.12.

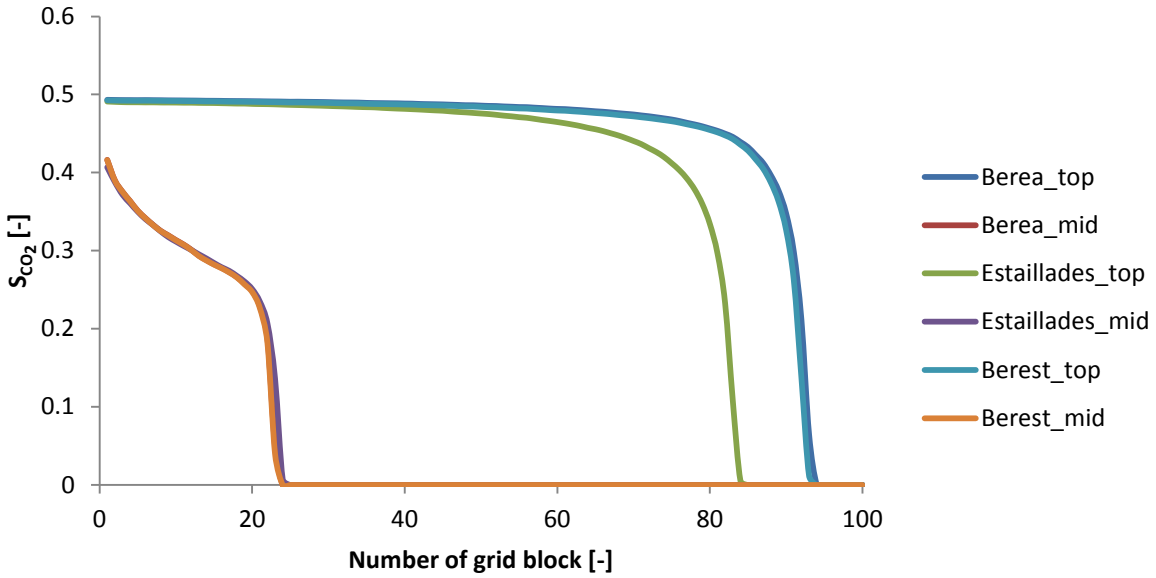

Figure 8.12 CO_2 saturation profile (linear velocity of $7.40 \text{ x } 10^{-7}$ m/s, $90\ m\ x\ 180\ m$*)*

As in the previous case, simulations with Berea and Berea-Estaillades combined capillary pressure curves are almost identical. But in this instance, the difference in the elongation of gravity fingers is higher between Berea and Estaillades, than in the case of higher linear velocity. So with increasing linear velocity, the retention effect of Estaillades $p_c$on gravity

fingering is less powerful. On can also observe; that the CO_2 saturation did not surpass the critical water saturation of 0.5 during any of the simulation cases.

8.6 Effect of micro-porosity on the $720\,x\,1440\,m$ model with $S_{wcrit} = 0.5$

The next simulation sequence was performed on a length scale of $720\,x\,1440\,m$. Although, it is not a realistic case, the buoyancy forces act stronger as the CO_2 column height increases. So with increasing column height, more spectacular results on the gravity fingering mitigation by micro-porosity could be expected. Moreover, the same capillary pressure curve has less stabilizing effect on viscous stability with increasing the length scale with accordance the definition of macroscopic capillary number. The simulations were run with the same constraints as the $90\,m\,x\,180\,m$ ones, but only for the linear velocity of $2.96\,x\,10^{-6}\,m/s$. The results for the same time step and three different p_c cases are shown in Fig 8.13. The saturation profile of the top and middle of reservoir geometry are illustrated in Fig. 8.14.

For this length-scale, the difference of the three capillary pressure cases became less obvious. Moreover, the maximum achieved CO_2 saturation was close to 0.5, despite of the larger length-scale, so the capillary curves could only affect displacement in this saturation window, which is still in the macro-porosity range.

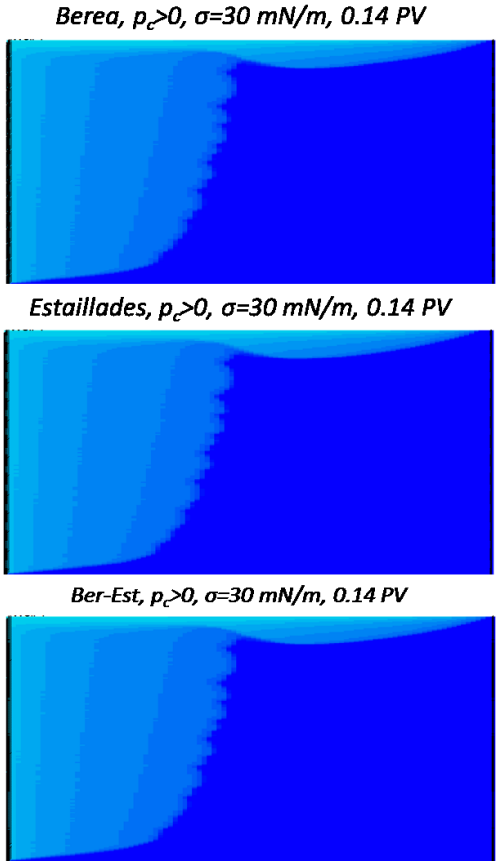

Figure 8.13 Simulation results with a gravity ratio of 0.41 *(linear velocity of* $2.96\,\mathrm{x}\,10^{-6}\,\mathrm{m/s}$*)*

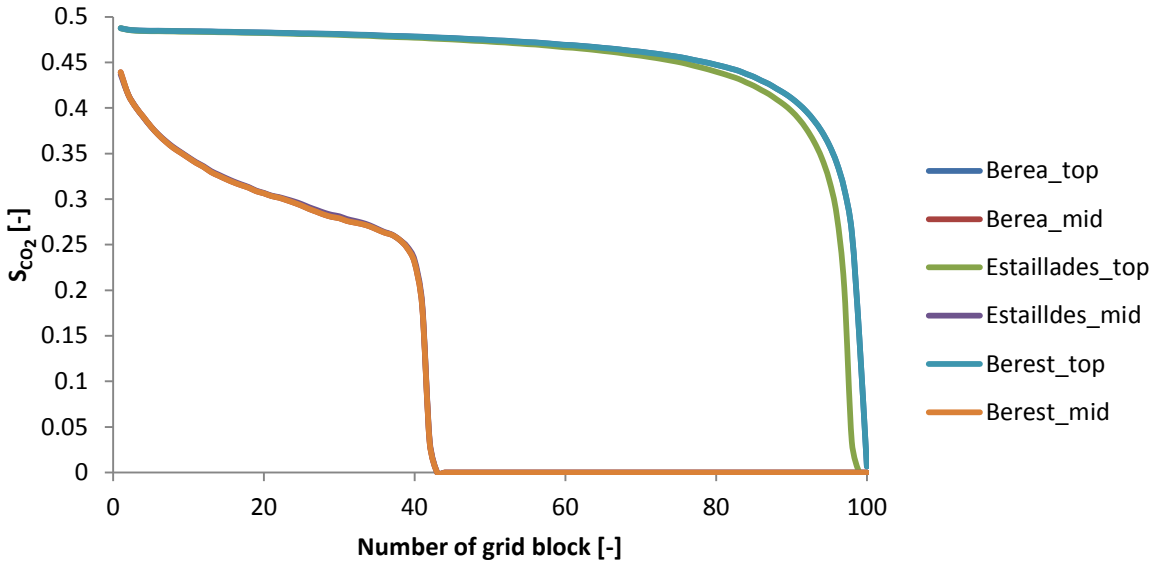

Figure 8.14 CO_2 saturation profile (linear velocity of 2.96×10^{-6} m/s)

8.7 Discussion of the simulation results with $S_{wcrit} = 0.5$

During the previous simulation sequence, the CO_2 saturation could not reach the micro-porosity, which would happen if the CO_2 saturation was higher than 0.5. The brine saturation could not go below the critical water saturation, even though with initialization, when the brine-CO_2 transition zone was modeled for the $90\ x\ 180\ m$ length-scale, it was possible. To further elaborate this, the model of $720\ x\ 1440\ m$ length-scale was run for a year, and then CO_2 injection was shut. Despite of such large length-scale, and a simulation time of 30 000 years, no higher CO_2 saturation than 0.5 was achieved. Even though, a length-scale of $90\ x\ 180\ m$ already provided sufficient CO_2 column height for the occupation of a substantial range of micro-porosity by CO_2. This led to the conclusion that by setting up a static saturation height model, even with a relative permeability curve having a critical water saturation of 0.5, the micro-porosity can be occupied by buoyancy, with a sufficiently high CO_2 column. Despite of this fact, the invasion of micro-porosity by CO_2 was not durable through dynamic modeling. This could arise from the fact, that CMG IMEX does not allow water flow below critical water saturation, even though it would be possible by physical means (buoyancy).

Knowing that with this relative permeability model the invasion of micro-porosity is not possible; the mitigation effect of micro-porosity on gravity fingering was not tested under these conditions. Moreover, the available saturation window for CO_2 with higher critical water saturation is narrower. In the following picture the simulation results of Estaillades and Berea are compared, with typical relative permeability models for carbonate and sandstone implemented. As Berea is well-sorted sandstone with most of the pore volume in the macro-porosity range, the critical water saturation is lower, than for carbonates with micro-porosity in general. In the following simulation runs, for the Estaillades p_c, the previously introduced, meanwhile for Berea the best matched parameters of the study Berg et al. (2013) was

applied. The results of the $90\ x\ 180\ m$ model are illustrated with a linear velocity of $7.4\ x\ 10^{-7} m/s$ in Fig. 8.15:

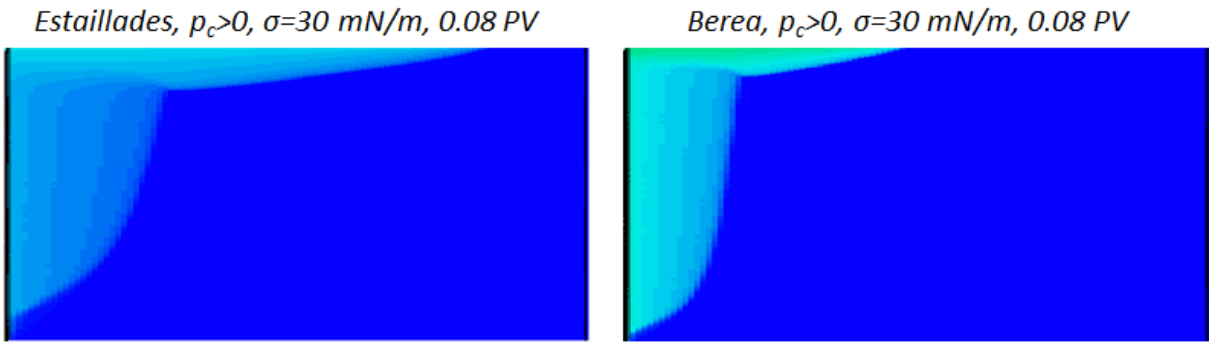

Figure 8.15 Left, $k_{r,CO_2}(S_{wcrit} = 0.5) = 0.5$, $n_{brine} = 2.0$, $n_{CO_2} = 3.5$*; right,* $k_{r,CO_2}(S_{wcrit} = S_{wcon} = 0.2) = 0.5$, $n_{brine} = 2.5$, $n_{CO_2} = 3.7$

With such model configuration, the presence of micro-porosity has even an adverse effect on displacement stability by bearing with narrower available saturation window, leading to more elongated gravity fingers.

8.8 Effect of micro-porosity with on displacement stability with $S_{wcrit} = S_{wcon} = 0$

As it was discussed previously, it was not possible to simulate the invasion of CO_2 to the micro-porosity by buoyancy forces, with the previously introduced relative permeability model. So the need of the application of another relative permeability model was obvious. For that purpose, the critical water saturation was made equal to the connate water saturation, both to be 0.0. The Corey-coefficient was selected to be $\mathrm{n_{brine}} = 4.0$, so that the water relative permeability curve until the brine saturation of 0.2 basically acts like immobile, but still allows water flow to a limited extent. The end-point relative permeability values were selected to be 1 for both phases, as this provides a relative permeability value for CO_2 (with $n_{CO_2} = 3.5$) at a water saturation of 0.2 close to 0.5, which is a reasonable value for CO_2-brine displacement based on literature (Berg et al, 2013).

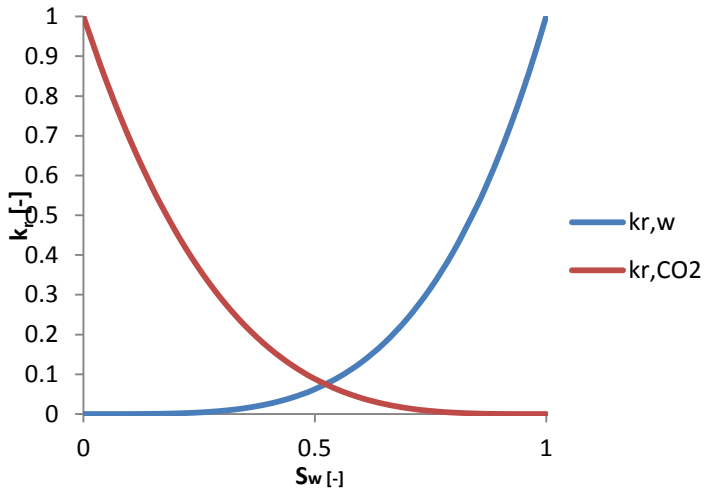

Figure 8.16 The applied relative permeability curve ($S_{wcon} = S_{wcrit}$=0, $n_{brine} = 4.0$, $n_{CO_2} = 3.5$)

The simulation results for the previously introduced relative permeability curve, ignoring capillarity, excluding and including gravity forces are shown in Fig. 8.17. The applied linear velocity was $7.4\ x\ 10^{-7} m/s$ for the coming simulation sequence.

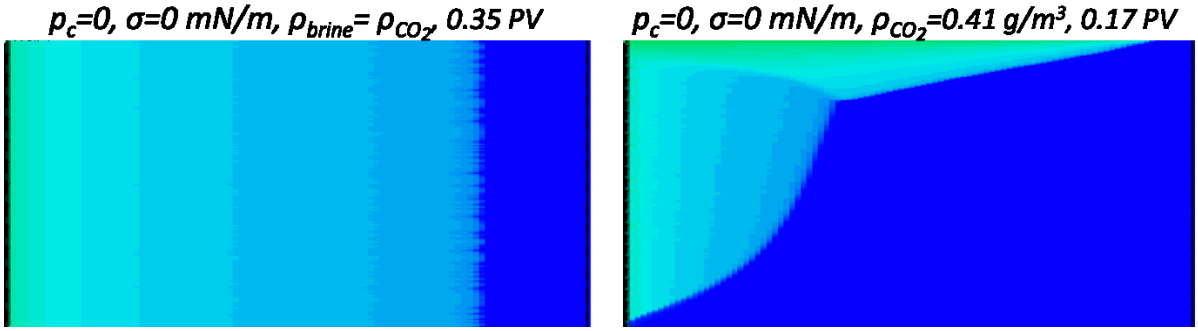

Figure 8.17 Simulation results with $S_{wcon} = S_{wcrit}$=0, $n_{brine} = 4.0$, $n_{CO_2} = 3.5$ and end-point relative permeabilities of 1

Then the three p_c cases were introduced and tested over different length-scales, firstly for the cases excluding gravity forces, as it can be seen in Fig. 8.18.

One can observe that with increasing length-scale, the effect of capillary pressure function diminishes, as it is predictable from the macroscopic capillary number. When gravity is introduced, with increasing length-scale the displacement front gets less stable, as it can be seen in Fig. 8.19. The difference between the models with the three different p_c curves is also getting less spectacular with larger length-scales. It is visible that the gravity fingering is more severe for the Berea model, than Berea-Estaillades. The Estaillades p_c shows the most potential of stabilizing gravity fingering. The Berea p_c model shows the highest CO_2 saturation at the top of the reservoir and the most elongated gravity fingers.

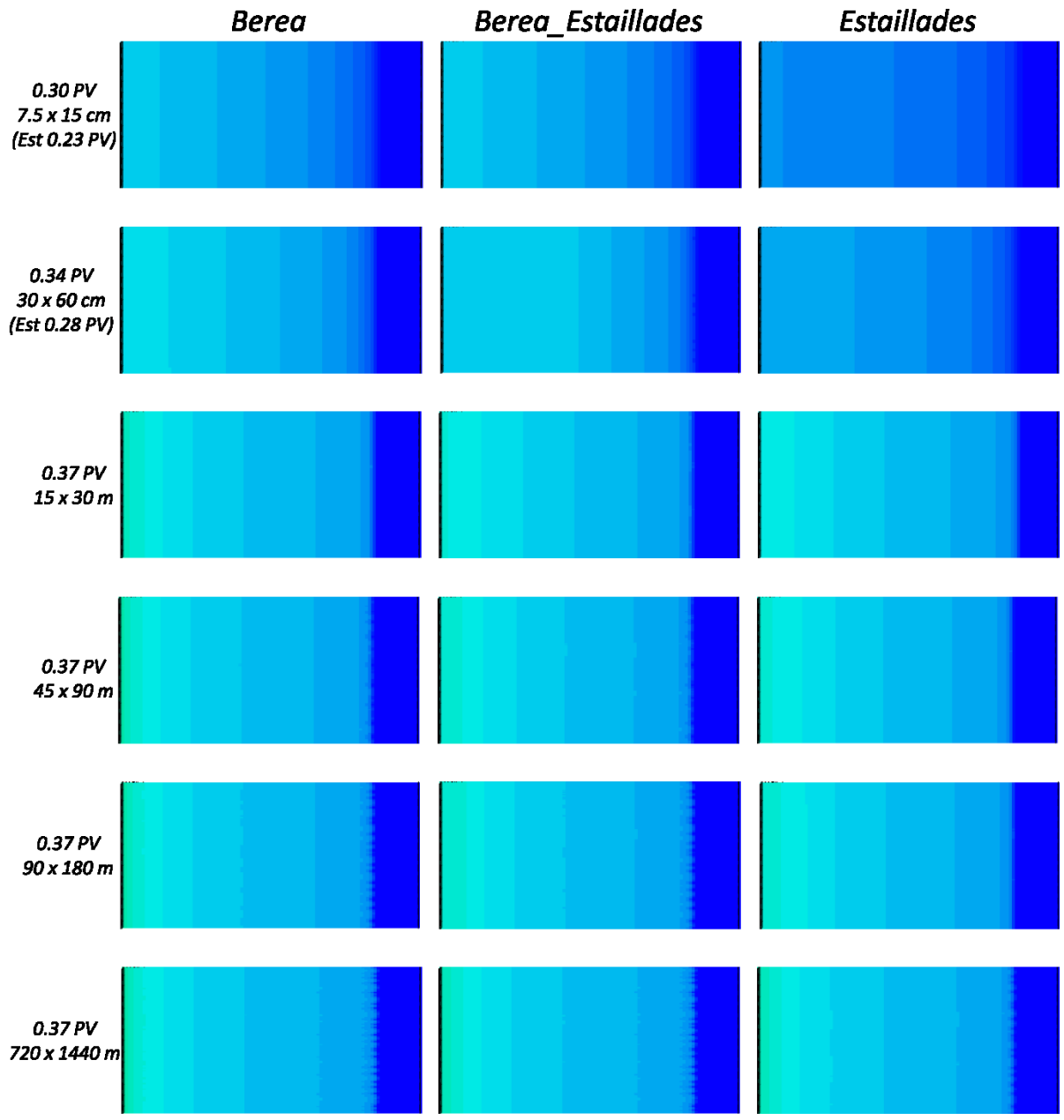

Figure 8.18 Simulation results with $S_{wcon} = S_{wcrit}$=0, $n_{brine} = 4.0$, $n_{CO_2} = 3.5$ and end-point relative permeabilities of 1, excluding gravity

Despite of the fact that with larger length-scales, a higher CO_2 saturation can be achieved in the top of the reservoir, and even micro-porosity can be invaded, the mitigation effect of micro-porosity on gravity fingering is less powerful with increasing length-scales.

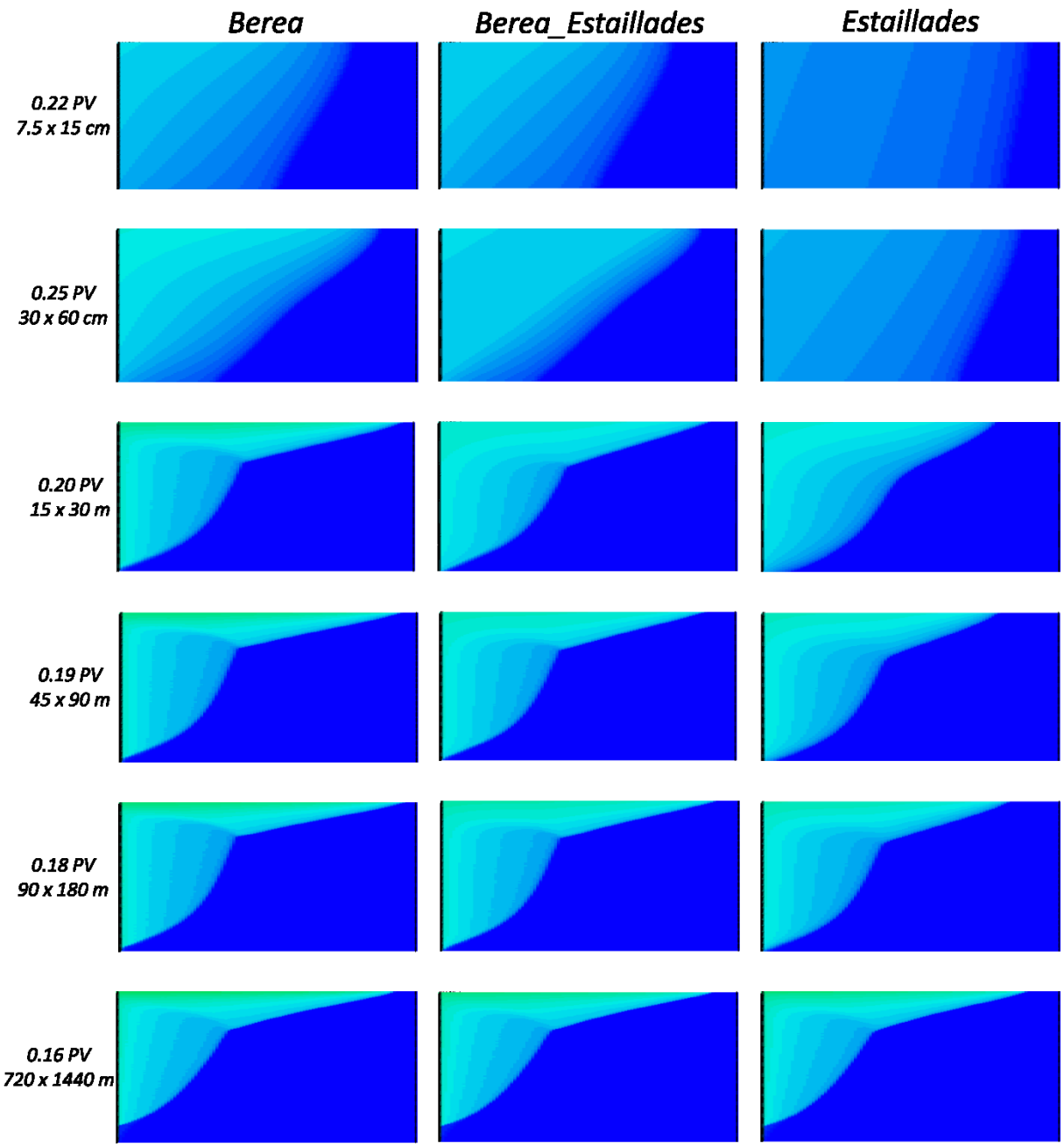

Figure 8.19 Simulation results with $S_{wcon} = S_{wcrit}$=0, $n_{brine} = 4.0$, $n_{CO_2} = 3.5$ and end-point relative permeabilities of 1, with a $CO_2/brine$ gravity ratio of 0.41

8.9 Effect of micro-porosity on displacement stability with a critical water saturation of $S_{wcrit} = S_{wcon} = 0$ and the alteration of linear velocity

According to the term, gravity number, as the linear velocity increases, the model gets more dominated by viscous forces and less by gravity forces. The effect of altering the linear velocity was tested also for the relative permeability model introduced in Chapter 8.8, on the length scale of $90\ m\ x\ 180\ m$ as in Chapter 8.5. As it was predictable, increasing the linear velocity resulted in a more stable displacement, so less severe gravity fingering, as it can be seen in Fig. 8.20.

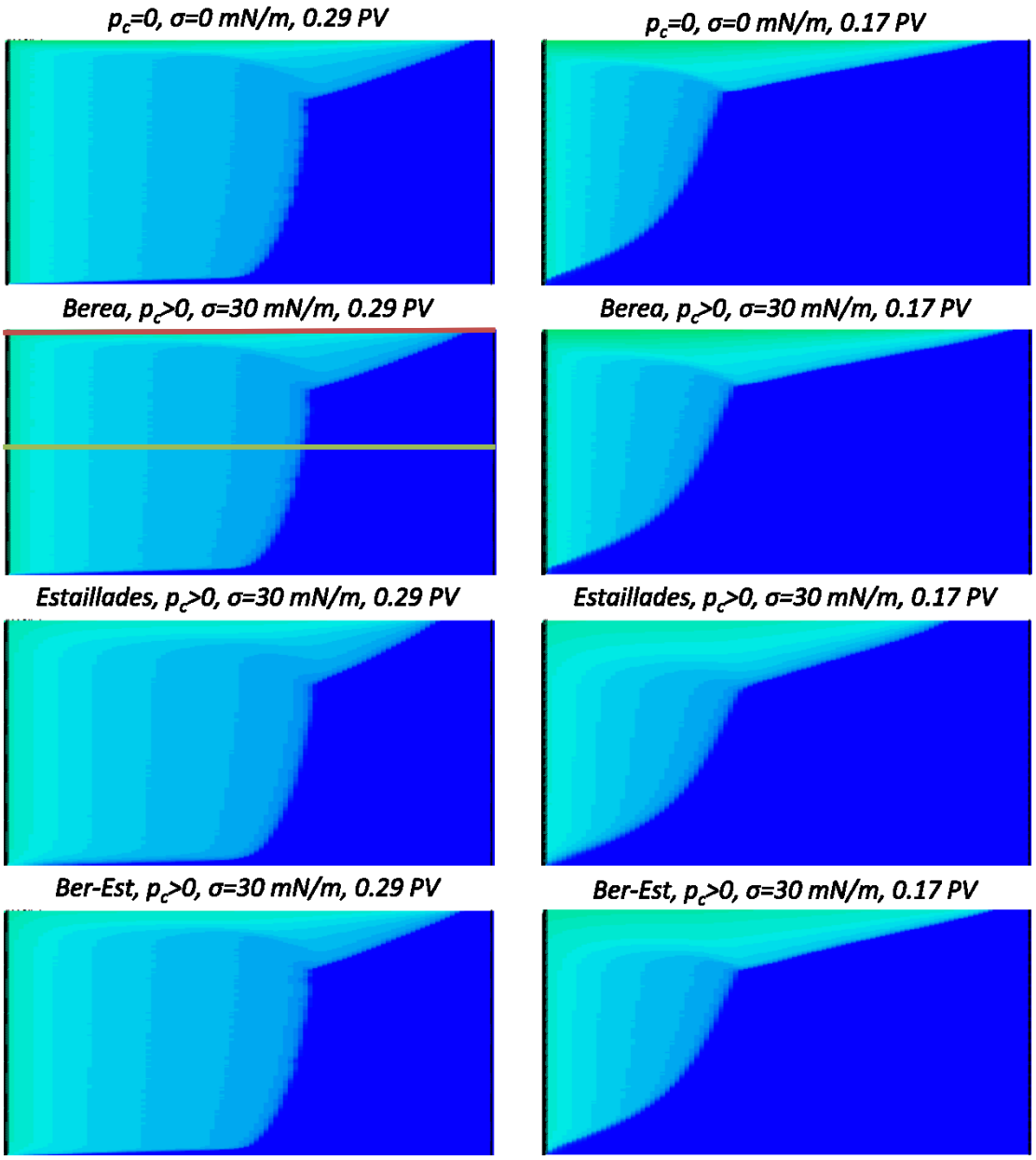

Figure 8.20 Simulation results with a gravity ratio of 0.41 *(linear velocity of* $2.96 \text{ x } 10^{-6}$ m/s *on the left and* $7.40 \text{ x } 10^{-7}$ m/s *on the right,* $90\ m\ x\ 180\ m$)

If the saturation profiles are plot along the top and midline of reservoir geometry in $\vec{\imath}$direction (Fig, 8.21 and Fig. 8.22), the different models show more variation compared to the ones from Chapter 8.5. With reducing the S_{wcrit} to 0, higher CO_2 saturation were achieved. In both linear velocity cases, the Berea model showed the highest CO_2 saturation in the top of the reservoir and the most prominent gravity fingering; meanwhile the midline saturation profiles are similar.

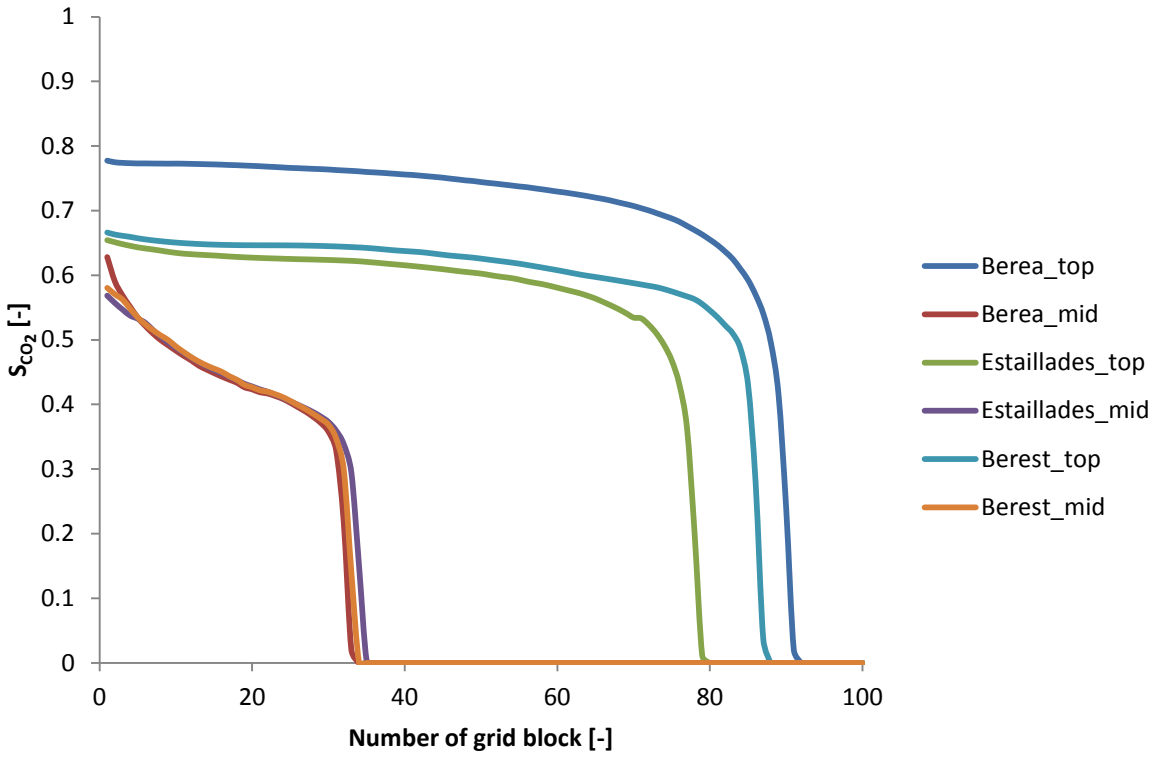

Figure 8.21 CO_2 saturation profile (linear velocity of $7.40 \text{ x } 10^{-7}$ m/s, $90\ m\ x\ 180\ m$, $S_{wcon} = S_{wcrit} = 0$*)*

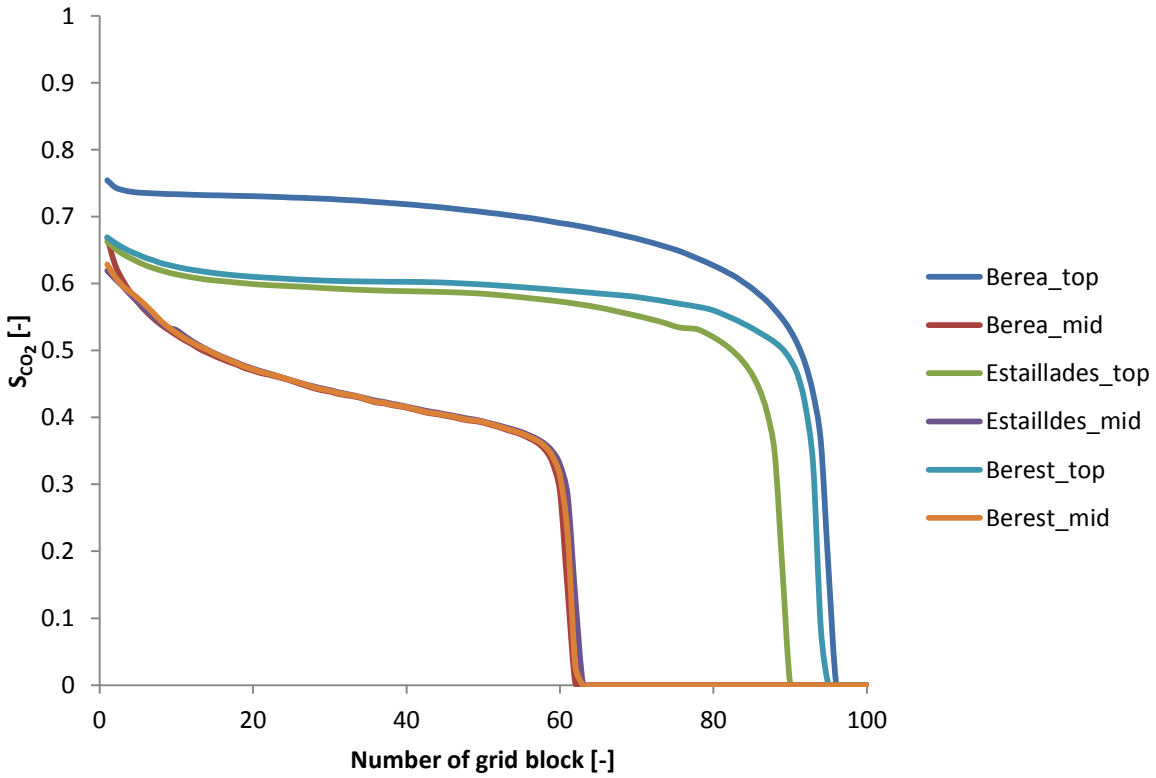

Figure 8.22 CO_2 saturation profile (linear velocity of $2.96 \text{ x } 10^{-6}$ m/s, $90\ m\ x\ 180\ m$, $S_{wcon} = S_{wcrit} = 0$*)*

One can observe that when higher linear velocity, the midline saturation front gets closer to saturation front plotted along the top of the reservoir, meaning more stable displacement. Important to note, that in case of faster CO_2 flow, the retention effect of Estaillde s and Berea-Estaillades p_c on gravity fingering becomes less prominent as the system gets less gravity dominated. Decreasing the S_{wcrit} to 0 had such positive effect on the simulations that CO_2 could reach higher saturation, than 0.5, meaning the occupation of micro-porosity was enabled by the application of this relative permeability model.

8.10 Effect of alteration of density ratio on displacement stability

For testing the effect of CO_2-brine density ratio on displacement stability, the relative permeability model from the previous chapter was used. As gravity fingering occurs due to the density difference between displacing and displaced phases, the smaller the density difference is the more gravity-wise stable displacement front is expected as the gravity number gets smaller. Three different CO_2-brine density ratios were tested; 0.20, 0.41 that was used in previous cases and 0.60. A displacement velocity of $7.4\,x\,10^{-7} m/s$ was selected, as it results in more prominent gravity fingering, so more spectacular differences and easier comparison as well. In these simulation results, different color scale was applied, because that makes the saturation distribution easier to observe. The simulation results for the three density ratio cases excluding capillary effects are shown in Fig. 8.23.

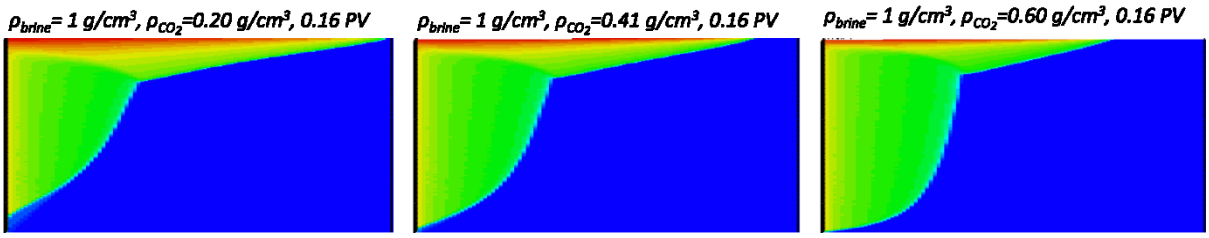

Figure 8.23 Simulations with three different density ratios, excluding capillarity

As it was predicted, the higher the density ratio, the more stable the displacement front is. It is also visible that higher CO_2 saturation can be achieved at the top of the reservoir, if the density ratio is smaller. This is due to the fact, that buoyancy acts stronger, with decreasing density ratio.

Then simulations were run with introducing the three $p_c$cases, scaled with an IFT of $30\,mN/m$. The results can be seen in Fig. 8.24. It is clearly visible that increasing the density ratio has a substantial stabilizing effect on the displacement front. As in the previous chapter, the Berea model has the highest CO_2 saturation in the top of the reservoir, and the most elongated gravity fingers followed by Berea-Estaillades and Estaillades.

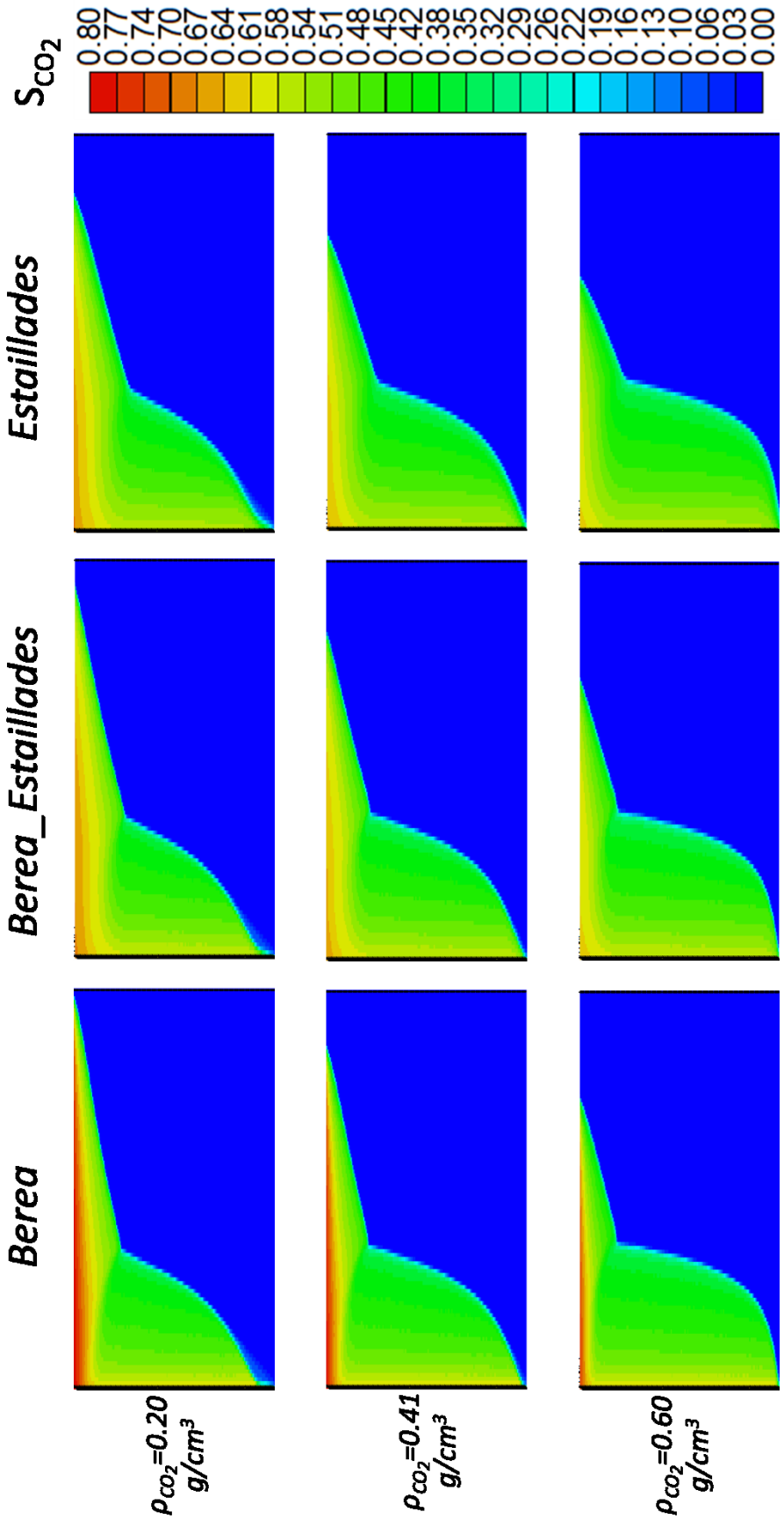

Figure 8.24 Simulation results with three different density ratios, including capillarity (0.16 PV)

8.11 Effect of micro-porosity with on displacement stability with $S_{wcrit} = S_{wcon} = 0$ and $n_{brine} = 2.0$

As reducing S_{wcrit} to S_{wcon}=0, had a positive impact on simulation results by enabling the simulation of flow in the micro-porosity range, increasing brine relative permeability mostly in the range of micro-porosity (up to 0.5 brine saturation) could even result in more spectacular differences. To achieve that, n_{brine} of 2.0 was used, so the rock-type became less water-wet. This is not a realistic case, as in a CO_2-brine system, the brine is the wetting phase, and only used for representation. The relative permeability model is illustrated in 8.25.

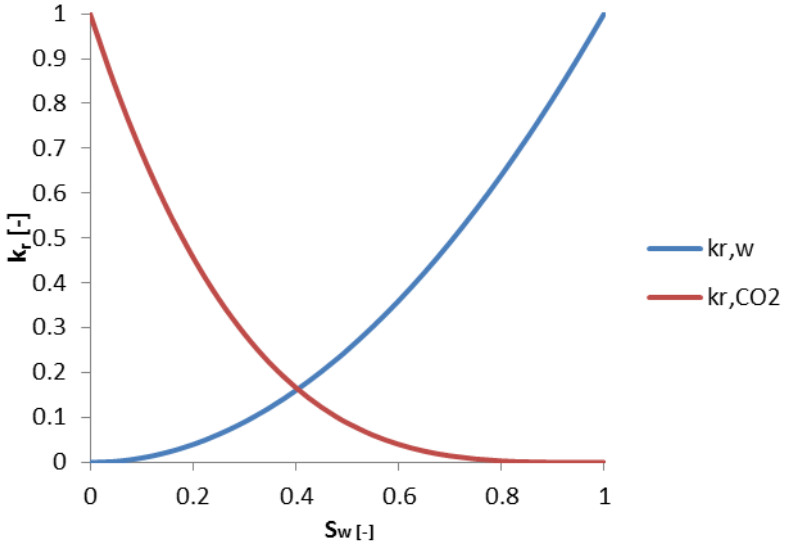

Figure 8.25 The applied relative permeability curve ($S_{wcon} = S_{wcrit}$=0,, $n_{brine} = 2.0$, $n_{CO_2} = 3.5$)

As it was predicted, even more spectacular differences occurred between the different p_c models (Fig. 8.26), than in Chapter 8.9, which is considered to be a more realistic case. With this relative permeability curve model, the retention effect of micro-porosity on gravity fingering is clearly visible. When the saturation profile if plot along the top and midline of the reservoir (Fig. 8.27) one can observe that at the top of the reservoir, higher than 0.7 CO_2 saturation was achieved for all cases. As previously, the highest CO_2 saturation in the top was achieved in the Berea model, which has no micro-porosity. Due to lacking micro-porosity, in the Berea model, the gravity fingers are more elongated, than in Berea-Estaillades and Estaillades.

The saturation profiles along the midline are mostly identical for the three cases, but in the case of Berea model, there is significantly higher CO_2 saturation at the injection point, than the other two have.

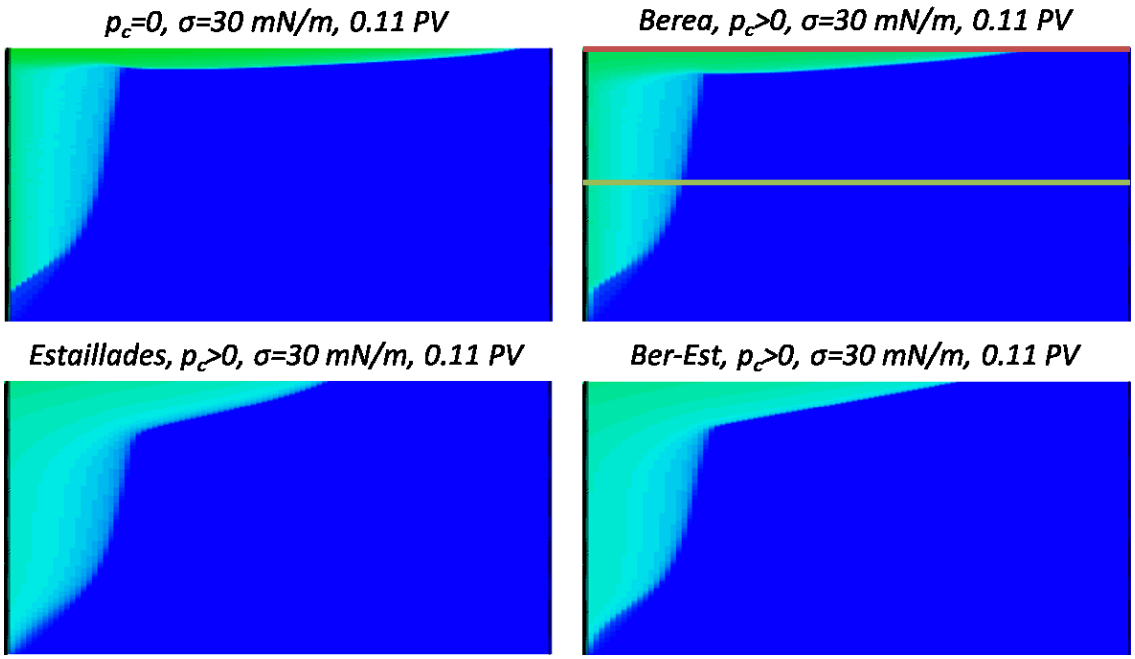

Figure 8.26 Simulation results with the linear velocity of $7.4\ x\ 10^{-7}\ m/s$, a CO_2-brine density ratio of 0.41 and $S_{wcon} = S_{wcrit}$=0, $n_{brine} = 2.0$, $n_{CO_2} = 3.5$

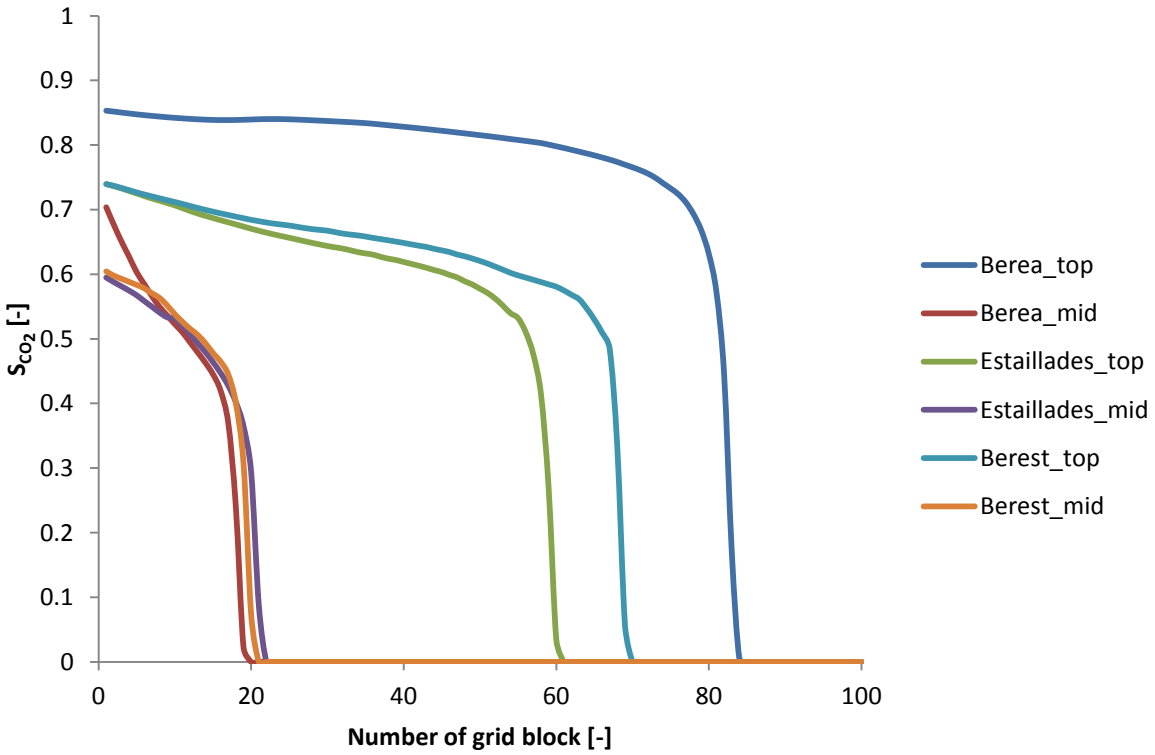

Figure 8.27 Saturation profiles with a CO_2-brine density ratio of 0.41, $S_{wcon} = S_{wcrit}$=0, $n_{brine} = 2.0$, $n_{CO_2} = 3.5$

8.12 Summary of the results

By performing the previously introduced simulations, the importance of proper selection of relative permeability function gained even more importance. Meanwhile, occupation of micro-porosity was possible by the initialization of CO_2-brine transition zone (Fig. 8.6), when S_{wcrit} was selected to be 0.5 (which is a realistic case), no CO_2 could enter to the micro-porosity (meaning no higher CO_2 saturation, than 0.5 was achieved) by dynamic means despite of trying unrealistically high length-scales as well (even though S_{wcon} was 0.0). Even the Berea model, which lacks micro-porosity, had the maximum of 0.5 CO_2 saturation reached throughout the reservoir geometry under these conditions. For these cases, the Berea and Berea-Estaillades were basically identical, as they have the same capillary pressure values for the CO_2 saturation range of $0.0 - 0.5$. Because of the fact that Estaillades has higher capillary pressure values for that CO_2 saturation window, the gravity fingering is substantially reduced, even though the invasion of micro-porosity by CO_2 did not happen by this simulation model.

When S_{wcrit} was set to be equal to S_{wcon} (both equal to 0.0), the effect of the presence of micro-porosity on gravity fingering became more evident, as it enabled the invasion of CO_2 to larger porosity range. In general, the Berea model has the most elongated gravity fingers and the highest CO_2 saturation at the top of the reservoir, regardless the applied linear velocity, CO_2-brine density ratio and relative permeability model parameters. The difference in the gravity finger elongation, for the three models, diminishes as the linear velocity increases though, as the relative significance of viscous forces to gravity forces increases. Further observation was that even though, larger length-scales result in higher CO_2 saturations at the top of the reservoir, so the micro-porosity can be invaded by CO_2, the retention effect of micro-porosity becomes less visible with increasing length-scales (as it can be seen in Fig 8.19), despite of expectations.

If the CO_2-brine density ratio is modified, it also has a major impact on gravity fingering. When the density difference becomes less, the buoyancy plays smaller role. This leads to a more stable displacement front. If the density difference is higher, this happens vice versa.

9 Conclusions and recommendations

Underground CO_2 storage in deep saline aquifers can provide a promising solution for reducing greenhouse gas emissions, but in order to enable a safe and efficient storage, the multiphase behavior of CO_2-brine displacement for given conditions needs to be understood. Due to the higher residual water saturation, the available saturation window for CO_2 is narrower in micro-porosity bearing rocks. From this perspective, micro-porosity has an adverse effect on gravity-fingering, resulting in longer gravity fingers and hence a higher penetration depth of the CO_2 plume in the aquifer.

The appropriate relative permeability model for the simulation and modeling of CO_2 plume flows and plume displacement stability is vital. Previously, many concerns were raised if the generally low end-point relative permeability of CO_2 and high remaining water saturation during CO_2-brine relative permeability measurements is indeed realistic, or the result of the limitations of the measurement techniques. Unrealistically high residual water saturations could remain in the core sample also as a result of bypassing through more permeable channels, so reducing the sweep efficiency. As the significance of the selection of the appropriate water saturation point, under what it becomes immobile, was presented in this thesis; further investigations are recommended to be performed. It is also required due to the limited available on CO_2-brine relative permeability data.

The further investigation of CO_2-brine relative permeability behavior is especially important for modeling the effect of micro-porosity on gravity fingering. In larger length-scales, such CO_2 column height can be achieved that enables the invasion of CO_2 to micro-porosity by buoyancy forces, what is not possible under the conditions of typical core-flood relative permeability measurements. The formulation of CMG IMEX did not make it possible to model CO_2-brine displacement reaching lower, than critical brine saturation for carbonate rocks dynamically, although it would have been possible physically by buoyant forces. For that reason, the widening of mobile water saturation window was required, to achieve better results. With the reduced critical water (or remaining) saturation, the retention effect caused by micro-porosity on gravity fingering became more realistic, and the occupation of micro-porosity by CO_2 also happened during the simulations, but this retention effect is decreasing with the increasing length-scale, despite of expectations. Consequently, by underestimating the end-point relative permeability and overestimating the critical water saturation by an inappropriate for the purpose relative permeability measurement can result in the overestimation of gravity fingering. For avoiding that, it is recommended to revise the applied relative permeability measurement methods, and find the most suitable one.

As the models created in this thesis were created to provide understanding on the effect of different relative permeability parameters and capillary pressure curves on the displacement stability, many otherwise important conditions were not tested. These are for example CO_2 compressibility, general reduced absolute permeability in vertical direction and rock heterogeneity. Those could be the objective of further studies, along 3D modeling of gravity fingering with a tool enabling appropriate gridding.

10 References

Barnett, C., 2015. Groundwater Wake-up. [Online] Available at: http://ensia.com/features/groundwater-wake-up/

Bennion, D. B., & Bachu, S. (2008, January 1). Drainage and Imbibition Relative Permeability Relationships for Supercritical CO_2 /brine and H_2S -/Brine systems in intergranular Sandstone and Carbonate Formations. Society of Petroleum Engineers.

Bennion, D. B., & Bachu, S. (2010, January 1). Drainage and Imbibition CO2/Brine Relative Permeability Curves at Reservoir Conditions for High-Permeability Carbonate Rocks. Society of Petroleum Engineers. doi:10.2118/134028-MS

Benson, S.M., Pini, R., Reynolds, C., & Krevor, S. C.M. (2013). Global CCS Institute Targeted Report No. 2. Relative Permeability Analysis to Describe Multiphase Flow in CO_2 Storage Reservoirs.

Benson, S.M., Pini, R., Reynolds, C., & Krevor, S. C.M. (2015). Global CCS Institute Targeted Report, Relative Permeability for Multiphase Flow in CO2 Storage Reservoirs, Part II

S. Berg, S. Oedai, H. Ott, Displacement and mass transfer between saturated and unsaturated CO_2–brine systems in sandstone, International Journal of Greenhouse Gas Control, Volume 12, January 2013, Pages 478-492, ISSN 1750-5836, http://dx.doi.org/10.1016/j.ijggc.2011.04.005.

S. Berg, H. Ott, Stability of CO2–brine immiscible displacement, International Journal of Greenhouse Gas Control, Volume 11, November 2012, Pages 188-203, ISSN 1750-5836, http://dx.doi.org/10.1016/j.ijggc.2012.07.001.

S. Berg, S. Oedai, H. Ott, Displacement and mass transfer between saturated and unsaturated CO2–brine systems in sandstone, International Journal of Greenhouse Gas Control, Volume 12, January 2013, Pages 478-492, ISSN 1750-5836, http://dx.doi.org/10.1016/j.ijggc.2011.04.005.

Richard L Christiansen, Susan M. Howarth, Literature review and recommendation of methods for measuring relative permeability of anhydrite from the Salado Formation at the Waste Isolation Pilot Plant, Sandia National Laboratories Albuquerque, New Mexico 87185 and Livermore, California 94550, 1995, DOI: 10.2172/100218

Chuoke, R. L., van Meurs, P., & van der Poel, C. (1959, January 1). The Instability of Slow, Immiscible, Viscous Liquid-Liquid Displacements in Permeable Media. Society of Petroleum Engineers.

Corey, A.T., 1954. The interrelation between gas and oil relative permeabilities. Producers Monthly 19 (1), 38–41.

Darcis, M., Class, H., Flemisch, B., & Helmig, R. (2011). Sequential Model Coupling for Feasibility Studies of CO_2 Storage in Deep Saline Aquifers. Oil and Gas Science and Technology, 66(1), 93-103

L.P. Dake, Fundamentals of reservoir engineering, Shell Internationale Petroleum Maatschappij B. V., The Hague, 1978, The Netherlands

Egermann, P., Chalbaud, C. A., Duquerroix, J., & Le Gallo, Y. (2006, January 1). An Integrated Approach to Parameterize Reservoir Models for CO2 Injection in Aquifers. Society of Petroleum Engineers. doi:10.2118/102308-MS

Feder, J., 1998. Fractals, Plenum Publishing, New York

Garcia, Julio E., Pruess, Karsten, Flow Instabilities During Injection of CO_2 into Saline Aquifers, 2008, http://escholarship.org/uc/item/8b23d72k

Hilfer, R., Oren, P-e., 1996. Dimensional analysis of pore scale and field scale immiscible displacement. Transport in Porous Media 22, 53-72

Egermann, P., Chalbaud, C. A., Duquerroix, J., & Le Gallo, Y. (2006, January 1). An Integrated Approach to Parameterize Reservoir Models for CO2 Injection in Aquifers. Society of Petroleum Engineers. doi:10.2118/102308-MS

Kuo, C., Perrin, J.-C., & Benson, S. M. (2010, January 1). Effect of Gravity, Flow Rate, and Small Scale Heterogeneity on Multiphase Flow of CO2 and Brine. Society of Petroleum Engineers. doi:10.2118/132607-MS

L.W. Lake, Fundamentals of Enhaced Oil Recovery, 1989, Prentice Hall.

F. Jerry Lucia, Carbonate Reservoir Characterization: An integrated Approach, 1999

Luo, P., and H. G. Machel. “Pore Size and Pore Throat Types in a Heterogeneous Dolostone Reservoir, Devonian Grosmont Formation, Western Canada Sedimentary Basin.” AAPG Bulletin 79.11 (1995): n. pag. Print.

Osman, P., 2007. climate & energy. [Online] Available at: http://www.energysustained.com/managing_impacts.htm [Accessed 21 January 2017].

H. Ott, C.H. Pentland, S. Oedai, CO2–brine displacement in heterogeneous carbonates, International Journal of Greenhouse Gas Control, Volume 33, February 2015, Pages 135-144, ISSN 1750-5836, http://dx.doi.org/10.1016/j.ijggc.2014.12.004.

H. Ott, CO_2-BRINE PRIMARY DISPLACEMENT IN SALINE AQUIFERS Experiments, Simulations and Concepts Fakultat fur Georessourcen und Materialtechnik Der RWTH Aachen, 2015 **A**

H. Ott, Geological carbon storage: processes, risks and opportunities, Imperial College, Shell Global Solutions International B.V, 2015 **B**

Prabir Daripa · G. Pas, On Capillary Slowdown of Viscous Fingering in Immiscible Displacement in Porous Media, Received: 31 January 2007 / Accepted: 10 January 2008 / Published online: 12 February 2008 © Springer Science+Business Media B.V. 2008

Riaz, H.A. Tchelepi, Influence of relative permeability on the stability characteristics of immiscible flow in porous media Transport in Porous Media, 64 (2006), pp. 315–338

Riaz, H.A. Tchelepi, Linear stability analysis of immiscible two-phase flow in porous media with capillary dispersion and density variations. Physics of fluids 16 (12), 4727-4737

Shah, S. M., Yang, J., Crawshaw, J. P., Gharbi, O., & Boek, E. S. (2013, September 30). Predicting Porosity and Permeability of Carbonate Rocks From Core-Scale to Pore-Scale Using Medical CT, Confocal Laser Scanning Microscopy and Micro CT. Society of Petroleum Engineers. doi:10.2118/166252-MS

IPCC, 2005: IPCC Special Report on Carbon Dioxide Capture and Storage. Prepared by Working Group III of the Intergovernmental Panel on Climate Change [Metz, B., O. Davidson, H. C. de Coninck, M. Loos, and L. A. Meyer (eds.)]. Cambridge University

Press, Cambridge, United Kingdom and New York, NY, USA, 442 pp.

IPCC, 2014: Climate Change 2014: Synthesis Report. Contribution of Working Groups I, II and III to the Fifth Assessment Report of the

Intergovernmental Panel on Climate Change [Core Writing Team, R.K. Pachauri and L.A. Meyer (eds.)]. IPCC, Geneva, Switzerland, 151 pp.

Liang-Biao Ouyang, New Correlations for Predicting the Density and Viscosity of SupercriticalCarbon Dioxide Under Conditions Expected in Carbon Capture and Sequestration Operations, The Open Petroleum Engineering Journal, 2011, 4, 13-21, Chevron Corporation, P. O. Box 5095, Bellaire, TX 77402-5095, USA

http://www.engineeringtoolbox.com/dynamic-absolute-kinematic-viscosity-d_412.html (12/29/2016)

https://commons.wikimedia.org/wiki/File:Carbon_dioxide_pressure-temperature_phase_diagram.svg (1/10/2017)

http://www.glossary.oilfield.slb.com/Terms/c/connate_water.aspx (2/28/2017)

http://www.glossary.oilfield.slb.com/Terms/i/irreducible_water.aspx (2/28/2017)

http://petrowiki.org/Relative_permeability#Residual_water_saturation (2/28/2017)

CMG IMEX

11 Appendices

11.1 Appendix A

Table 11.1 Value of bij coefficients in Eq. 4.2 for pressure $<$ 207 $bara$ (Liang-Biao, 2011)

	b_{i0}	b_{i1}	b_{i2}	b_{i3}	b_{i4}
i = 0	-2.148322085348E+05	1.168116599408E+04	-2.302236659392E+02	1.967428940167E+00	-6.184842764145E-03
i = 1	4.757146002428E+02	-2.619250287624E+01	5.215134206837E-01	-4.494511089838E-03	1.423058795982E-05
i = 2	-3.713900186613E-01	2.072488876536E-02	-4.169082831078E-04	3.622975674137E-06	-1.155050860329E-08
i = 3	1.228907393482E-04	-6.930063746226E-06	1.406317206628E-07	-1.230995287169E-09	3.948417428040E-12
i = 4	-1.466408011784E-08	8.338008651366E-10	-1.704242447194E-11	1.500878861807E-13	-4.838826574173E-16

Table 11.2 Value of bij coefficientsin Eq. 4.2 for pressure $>$ 207 $bara$ (Liang-Biao, 2011)

	b_{i0}	b_{i1}	b_{i2}	b_{i3}	b_{i4}
i = 0	6.897382693936E+02	2.730479206931E+00	-2.254102364542E-02	-4.651196146917E-03	3.439702234956E-05
i = 1	2.213692462613E-01	-6.547268255814E-03	5.982258882656E-05	2.274997412526E-06	-1.888361337660E-08
i = 2	-5.118724890479E-05	2.019697017603E-06	-2.311332097185E-08	-4.079557404679E-10	3.893599641874E-12
i = 3	5.517971126745E-09	-2.415814703211E-10	3.121603486524E-12	3.171271084870E-14	-3.560785550401E-16
i = 4	-2.184152941323E-13	1.010703706059E-14	-1.406620681883E-16	-8.957731136447E-19	1.215810469539E-20

Table 11.3 Value of dij coefficients in Eq. 4.4 for pressure $<$ 207 $bara$ (Liang-Biao, 2011)

	d_{i0}	d_{i1}	d_{i2}	d_{i3}	d_{i4}
i = 0	-1.958098980443E+01	1.123243298270E+00	-2.320378874100E-02	2.067060943050E-04	-6.740205984528E-07
i = 1	4.187280585109E-02	-2.425666731623E-03	5.051177210444E-05	-4.527585394282E-07	1.483580144144E-09
i = 2	-3.164424775231E-05	1.853493293079E-06	-3.892243662924E-08	3.511599795831E-10	-1.156613338683E-12
i = 3	1.018084854204E-08	-6.013995738056E-10	1.271924622771E-11	-1.154170663233E-13	3.819260251596E-16
i = 4	-1.185834697489E-12	7.052301533772E-14	-1.500321307714E-15	1.368104294236E-17	-4.545472651918E-20

Table 11.4 Value of dij coefficients in Eq. 4.4 for pressure $>$ 207 $bara$ (Liang-Biao, 2011)

	d_{i0}	d_{i1}	d_{i2}	d_{i3}	d_{i4}
i = 0	1.856798626054E-02	3.083186834281E-03	-1.004022090988E-04	8.331453343531E-07	-1.824126204417E-09
i = 1	6.519276827948E-05	-3.174897980949E-06	7.524167185714E-08	-6.141534284471E-10	1.463896995503E-12
i = 2	-1.310632653461E-08	7.702474418324E-10	-1.830098887313E-11	1.530419648245E-13	-3.852361658746E-16
i = 3	1.335772487425E-12	-8.113168443709E-14	1.921794651400E-15	-1.632868926659E-17	4.257160059035E-20
i = 4	-5.047795395464E-17	3.115707980951E-18	-7.370406590957E-20	6.333570782917E-22	-1.691344581198E-24

The end